COMPREHENSIVE COPPER ION HYDRATION: EXPERIMENTAL AND THEORETICAL INVESTIGATION OF $Cu^{2+}(H_2O)_n$, $Cu^{+}(H_2O)_n$, $CuOH^{+}(H_2O)_n$

by

Andrew Sweeney

A dissertation submitted to the faculty of
The University of Utah
in partial fulfillment of the requirements for the degree of

Doctor of Philosophy

Department of Chemistry

The University of Utah

May 2015

The University of Utah Graduate School

STATEMENT OF DISSERTATION APPROVAL

The dissertation of **Andrew Sweeney**

has been approved by the following supervisory committee members:

Peter Armentrout	, Chair	**2/18/15** Date Approved
Michael Morse	, Member	**2/18/15** Date Approved
Scott Anderson	, Member	**2/18/15** Date Approved
Joel Miller	, Member	**2/18/15** Date Approved
Ramesh Goel	, Member	**2/18/15** Date Approved

and by **Cynthia Burrows**, Chair/Dean of

the Department/College/School of **Chemistry**

and by David B. Kieda, Dean of The Graduate School.

ABSTRACT

Guided ion beam tandem mass spectrometry is used to probe the kinetic energy dependence of both $Cu^{2+}(H_2O)_n$, where n = 5 – 10, and $CuOH^+(H_2O)_n$, where n = 0 – 4 colliding with Xe. The resulting cross sections are analyzed using statistical models to yield 0 K bond dissociation energies (BDEs). The primary dissociation pathway for $Cu^{2+}(H_2O)_n$ consists of water loss followed by the sequential loss of additional waters at higher energies until n = 7, at which point charge separation to form $CuOH^+(H_2O)_m$ + $H^+(H_2O)_{n-m-2}$ is energetically favored. The primary dissociation pathway for $CuOH^+(H_2O)_n$ is also water loss and is followed by the sequential loss of additional waters at higher energies until n = 1, at which point OH loss become competitive. The BDEs for loss of water and OH from $CuOH^+(H_2O)$ are combined in a thermodynamic cycle with literature values to derive BDEs for the loss of OH from $CuOH^+(H_2O)_n$, where n = 0, 2 – 4.

Infrared multiple photon dissociation (IRPD) spectroscopy is performed on $CuOH^+(H_2O)_n$, where n = 2 – 9. These spectra are characterized through comparison to theoretical spectra of low energy isomers. It is found that $CuOH^+(H_2O)_n$ prefers a 4-coordinate inner shell, although contributions from 5-coordinate geometries cannot be ruled out in most cases and are clearly present for n = 7. This preference is found in the $Cu^{2+}(H_2O)_n$ system as well and differs from the $Cu^+(H_2O)_n$ system, which prefers a 2-

coordinate inner shell. Electronic structure calculations are further employed to yield BDEs which agree reasonably well with experimental values.

A method for modeling kinetic energy release distributions (KERD) on a guided ion beam tandem mass spectrometer is proposed. This method achieves reasonable agreement with dissociations occurring over loose transition states when reactants have little energy in excess of the dissociation threshold. Current limitations and future possibilities of this method are discussed in detail.

For my mother, who had wished to someday publish her writing.

There is no illusion to truth

Nor is there a lie in faith.

The link is made in the mind

When solitude finds pleasure in

The simplest form … And

Value is discovered outside

The struggle for freedom.

-C.F.Sweeney '93

TABLE OF CONTENTS

ACKNOWLEDGEMENTS

First and foremost, I thank my advisor, Dr. Peter Armentrout, for giving me time and space to learn on my own and direction when I needed it most. Under his guidance, I developed a sense of professional confidence and understanding that any problem can be solved with enough attention to detail.

I thank all past and present members of the Armentrout group, especially Dr. Theresa Hofstetter for selflessly taking time to ensure I was properly trained, and Chris McNary for being my go-to guy for almost everything.

I thank all of the personnel in the electronic and machine shops for their hard work and tutelage, especially Dennis Romney and Dale Heisler.

Finally, I want to express my gratitude for being able to travel the world in the name of science. I have experienced fruitful collaborations, made lasting friendships, and learned that nobody can ride a bicycle like the Dutch.

Funding for this work came from the National Science Foundataion, Grant CHE-1359769.

CHAPTER 1

INTRODUCTION

1.1 Background

The comprehensive investigation of copper ion hydration is part of an ongoing and systematic study in our lab on the interaction of metals with water.[1, 2, 3, 4, 5, 6] These studies are interesting because metal water interactions are ubiquitous. Copper ion water interactions, in particular, can be found in biological,[7, 8, 9] industrial,[10, 11] and environmental processes,[12, 13, 14] so understanding them on a fundamental level is of obvious importance.

Previous studies to understand copper ion water interactions have investigated a range of systems including $Cu^{2+}(H_2O)_n$,[15, 16, 17, 18, 19, 20] $Cu^{+}(H_2O)_n$,[21, 22, 23, 24] and $CuOH^{+}(H_2O)_n$.[15, 25, 26] The focus of each of these studies generally falls into one of two categories: structural characterization or dissociation behavior. Although much attention has been given to each of these systems, the thermodynamics of copper ion hydration are still largely unknown.

In this work, we use guided ion beam tandem mass spectrometry (GIBMS) to measure the kinetic energy dependence of $Cu^{2+}(H_2O)_n$, where n = 8 – 10 colliding with Xe. GIBMS is a powerful technique for measuring thermodynamic properties of small molecules and peptides, as demonstrated previously in our lab.[27, 28, 29, 30, 31, 32, 33] Its advantage over other methods is its precise control over the internal[34] and kinetic

energies[27] of the reactant and neutral. After the collision event, the resulting product intensities are converted to cross sections, which can be profitably thought of as reaction probabilities. The minimum energy at which a given product cross section has intensity is the known as the product threshold. Knowledge of the internal and kinetic energies of the reactants allows us to extract 0 K bond dissociation energies (BDEs) from these thresholds.

As charge separation is a dominant theme in transition metal ion hydration studies, we also measure the thermodynamics for $CuOH^+(H_2O)_n$, where n = 1 – 4. To complement this thermodynamic study, we use infrared multiple photon dissociation (IRPD) spectroscopy, which has established itself as a powerful tool for structural characterization.[35, 36] Specifically, $CuOH^+(H_2O)_n$, where n = 2 – 9, is characterized through comparison of the OH stretching region to theoretical spectra.

Water loss occurs over a loose transition state such that product thresholds from this mechanism are a direct measurement of the BDE.[3] Charge separation, however, occurs over a tight transition state described by a barrier to the reverse reaction.[2, 37] Therefore product thresholds from this mechanism are not a measure of the BDE but rather the bond enthalpy. To obtain the BDE, it is necessary to know the height of the barrier, which can be measured from the kinetic energy release distribution (KERD) of products.[38] We measure KERDs from a variety of systems using the GIBMS and present our efforts towards accurately modeling each distribution.

In this work we present a comprehensive study of copper ion hydration in its most available forms. These studies will help to understand how bond energies and coordination numbers change between charge states of a transition metal and how they

change with and without an OH ligand. Additionally, this work further develops ongoing studies in the Armentrout group to describe metal ion water interactions across the periodic table.

1.2 Overview

A detailed description of the instrumentation used in the present work is given in Chapter 2. The methods through which raw data are converted into cross sections and the statistical methods used to model those cross sections are also presented. A description of the theoretical methods utilized in the present work is also given, which includes level of theory, basis set, and correction factors.

Chapter 3 presents threshold collision-induced dissociation (CID) studies of $Cu^{2+}(H_2O)_n$, where n = 8 – 10 with Xe. These studies provide the first experimentally determined BDE for loss of water from $Cu^{2+}(H_2O)_n$, where n = 6 – 10. Additionally, competition between the water loss and charge separation pathways for n = 7 and 8 is investigated in detail. Ab-initio calculations provide structures for reactants and products at each complex size. Using these structures, theoretical BDEs and potential energy surfaces (PES) are calculated and compared to experiments.

Chapter 4 and 5 present studies on the $CuOH^+(H_2O)_n$ system. Chapter 4 discusses the infrared multiple photon dissociation (IRMPD) spectral analysis of $CuOH^+(H_2O)_n$, where n = 2 – 9. Chapter 5 discusses threshold CID studies of $CuOH^+(H_2O)_n$, where n = 1 – 4 with Xe. In both cases, ab-initio calculations are performed to provide structures for reactant and product isomers. These structures are used to generate theoretical spectra for the IRMPD studies and to generate BDEs and PES for the threshold CID studies.

Finally, Chapter 6 discusses the use of GIBMS for measuring KERDs. Several systems are investigated including the reaction of both $CuOH^+(H_2O)_n$ and H^+Gly with Xe. Statistical models to assess these distributions are implemented and the results are discussed in detail.

1.3 References

[1]Hofstetter, T. E.; Armentrout, P. B., J. Phys. Chem. A **117,** 1110 (2013)

[2]Cooper, T. E.; Armentrout, P. B., J. Chem. Phys. **134,** 114308 (2011)

[3]Cooper, T. E.; Carl, D. R.; Armentrout, P. B., J. Phys. Chem. A **113,** 13727 (2009)

[4]Carl, D. R.; Armentrout, P. B., J. Phys. Chem. A, **116,** 3802 (2012)

[5]Carl, D. R.; Chatterjee, B. K.; Armentrout, P. B., J. Chem. Phys. **132,** 044303 (2010)

[6]Carl, D. R.; Armentrout, P. B., ChemPhysChem **14,** 681 (2013)

[7]Thiele, D. J., Nucleic Acids Res. **20,** 1183 (1992)

[8]Frank, P.; Benfatto, M.; Szilagyi, R. K.; D'Angelo, P.; Longa, S. D.; Hodgson, K. O., Inorg. Chem. **44,** 1922 (2005)

[9]Waggoner, D. J.; Bartnikas, T. B.; Gitlin, J. D., Neurobiol. Dis. **6,** 221 (1999)

[10]Perales-Vela, H. V.; González-Moreno, S.; Montes-Horcasitas, C.; Cañizares-Villanueva, R. O., Chemosphere **67,** 2274 (2007)

[11]Winge, D. R.; Mehra, R. K., Int. Rev. Exp. Path. **31,** 47 (1990)

[12]Andrade, L. R.; Farina, M.; Amado Filho, G. M., Ecotoxicol. Environ. Saf. **58,** 117 (2004)

[13]Ma, M.; Zhu, W.; Wang, Z.; Witkamp, G. J., Aquat. Toxicol. **63,** 221 (2003)

[14]Fernandes, J. C.; Henriques, F. S., Bot. Rev. **57,** 246 (1991)

[15]Stone, J. A.; Vukomanovic, D., Int. J. Mass Spectrom. **185–187,** 227 (1999)

[16]Shvartsburg, A. A.; Siu, K. W. M., J. Am. Chem. Soc. **123,** 10071 (2001)

[17]Rios-Font, R.; Sodupe, M.; Rodriguez-Santiago, L.; Taylor, P. R., J. Phys. Chem. A **114,** 10857 (2010)

[18]Bérces, A.; Nukada, T.; Margl, P.; Ziegler, T., J. Phys. Chem. A **103,** 9693 (1999)

[19]Duncombe, B. J.; Duale, K.; Buchanan-Smith, A.; Stace, A. J., J. Phys. Chem. A **111,** 5158 (2007)

[20]O'Brien, J. T.; Williams, E. R., J. Phys. Chem. A **112,** 5893 (2008)

[21]Holland, P. M.; Castleman, A. W., J. Am. Chem. Soc. **102,** 6174 (1980)

[22]Magnera, T. F.; David, D. E.; Stulik, D.; Orth, R. G.; Jonkman, H. T.; Michl, J., J. Am. Chem. Soc. **111,** 5036 (1989)

[23]Dalleska, N. F.; Honma, K.; Sunderlin, L. S.; Armentrout, P. B., J. Am. Chem. Soc. **116,** 3519 (1994)

[24]Iino, T.; Ohashi, K.; Mune, Y.; Inokuchi, Y.; Judai, K.; Nishi, N.; Sekiya, H., Chem. Phys. Lett. **427,** 24 (2006)

[25]Bryantsev, V. S.; Diallo, M. S.; Goddard, W. A., J. Phys. Chem. A **113,** 1520 (2009)

[26]Marsh, B. M.; Zhou, J.; Garand, E., J. Phys. Chem. A **118,** 2063 (2014)

[27]Ervin, K. M.; Armentrout, P. B., J. Chem. Phys. **83,** 166 (1985)

[28]Fisher, E. R.; Kickel, B. L.; Armentrout, P. B., J. Chem. Phys. **97,** 4859 (1992)

[29]Mookherjee, A.; Armentrout, P. B., Int. J. Mass Spectrom. **370,** 16 (2014)

[30]McNary, C. P.; Armentrout, P. B., Phys. Chem. Chem. Phys. **16,** 26467 (2014)

[31]Hinton, C. S.; Citir, M.; Armentrout, P. B., Int. J. Mass Spectrom. **78,** 1157 (2013)

[32]Sunderlin, L. S.; Armentrout, P. B., J. Chem. Phys. **100,** 5639 (1994)

[33]Fisher, E. R.; Armentrout, P. B., J. Phys. Chem. **94,** 1674 (1990)

[34]Carl, D. R.; Moision, R. M.; Armentrout, P. B., J. Am. Soc. Mass Spectrom. **20,** 2312 (2009)

[35]Bush, M. F.; O'Brien, J. T.; Prell, J. S.; Saykally, R. J.; Williams, E. R., J. Am. Chem. Soc. **129,** 1612 (2007)

[36]Citir, M.; Hinton, C. S.; Oomens, J.; Steill, J. D.; Armentrout, P. B., J. Phys. Chem. A **116,** 1532 (2012)

[37]Cooper, T. E.; Armentrout, P. B., J. Phys. Chem. A **113,** 13742 (2009)

[38]Chesnavich, W. J.; Bowers, M. T., J. Am. Chem. Soc. **98,** 8301 (1976)

CHAPTER 2

EXPERIMENTAL, DATA ANALYSIS, AND THEORETICAL METHODS

2.1 Instrument

The instrument used in the present work is a guided ion beam tandem mass spectrometer, shown in Figure 2.1, and described in detail elsewhere.[1, 2] Briefly, the instrument consists of an ion source, a magnetic momentum analyzer for reactant selection, a collision cell, a quadrupole mass filter for product selection and a detector. In the present work, ions are generated using electrospray ionization (ESI) of 10^{-4} M solutions. The solution is delivered through a 35 gauge stainless steel needle at a rate of ~ 0.05 mL/hr whereupon an applied voltage of ~2 kV transfers the reactants into the gas phase. Shortly beyond the tip of the needle is an inlet capillary to the vacuum system, which is heated to 80 °C to in order to desolvate any large droplets created during ionization process. Ions then enter an 88 plate radio frequency (rf) ion funnel (IF), copied from a design described in detail elsewhere[3]. A super-imposed dc gradient, typically kept below 10 V so as to avoid collisional heating, collects and focuses the ions to increase signal intensity.[4, 5] At the end of the funnel, the ions enter an rf-only hexapole where thermalizing collisions with ambient gas (predominately air and water)[6] ensure a Maxwell-Boltzmann distribution of rovibrational states at room temperature.[6, 7, 8, 9] A set of dc electrodes placed between the hexapole rods act as an in-source fragmentation

technique to preferentially increase the intensity of smaller complex sizes.[9] These "fin" electrodes are located towards the end of the hexapole to allow the newly-formed fragment ions to rethermalize, as demonstrated elsewhere.[9, 10, 11] Ions generated in the source region then enter the magnetic momentum analyzer for mass/charge selection of the reactant beam. The reactant ions are then decelerated to a well-known kinetic energy and injected into the first of two collinear rf octopole ion guides. Reactant ions then pass through a collsion cell containing low pressures of Xe, which is used because it is large, monatomic, and polarizeable.[12, 13] These factors maintain the high efficiency of energy transfer needed to properly measure thermodynamic properties. After the collision cell, product and unreacted primary ions drift out of the second octopole ion guide and are mass selected by a quadrupole mass filter before detection using a Daly type detector.[14] For KERD studies, the kinetic energy of product and unreacted primary ions is measured in the second octopole region using retarding potential analysis.

2.2 Data Analysis

Ion intensities are converted into cross sections using the Beer-Lambert analogue,

$$I = I_0 \exp(-\rho\sigma\ell) \tag{2.1}$$

where I is the reactant ion intensity after the collision cell, I_0 is the reactant ion intensity before the collision cell, ρ is the number density of the neutral reactant, σ is the total reaction cross section, and ℓ is the length of the collision cell, 8.6 cm. The rf field of the octopole ion guide ensures that very few reactants and products are lost by scattering such that $I_0 - I = \sum I_j$, the sum of all product intensities. Intensities of the reactant and product ions are measured at three different pressures of Xe in the collision cell: ~0.2, 0.1, and 0.05 mTorr so that they may be extrapolated to zero pressure, which rigorously

represents a single collision event. Background collisions and detector noise are removed by subtracting the product ion intensities without gas in the collision cell from those with gas in the cell. Reactant ion intensity is measured at the beginning of each experiment as a function of a retarding potential applied to the octopole.[1] This intensity is differentiated and fit to a Gaussian distribution to obtain the absolute zero of energy as well as the distribution of reactant ion kinetic energies, which is used in later analysis. The relative energy of the reactants is converted from the lab frame voltage, V_{lab}, to the center of mass energy, E_{CM}, using eq. (2.1),

$$E_{CM} = qV_{lab}\, m/(m + M) \tag{2.2}$$

where m is the mass of the reactant neutral Xe, M is the mass of the reactant ion, and q is the charge of the ion.

BDEs for the loss of a single ligand are extracted from the zero pressure kinetic energy dependent cross section using the modified line-of-centers (LOC) model for bimolecular collisions

$$\sigma_j(E) = \sigma_0 \sum_i g_i(E + E_i - E_{0,j})^N/E \tag{2.3}$$

where σ_0 is an energy independent scaling factor, E is the relative collision energy, $E_{0,j}$ is an adjustable parameter representing the reaction threshold for channel j at 0 K, and N is an adjustable parameter that describes energy deposition.[2] The summation is over the rovibrational states of the reactant ion having energies E_i and populations g_i, where $\sum g_i = 1$. Rotational constants and vibrational frequencies are taken from quantum chemical calculations of the reactant and product ground isomers. Rovibrational states are counted using the Beyer-Swinehart-Stein-Rabinovitch[15, 16, 17] algorithm and are assigned populations, g_i, on the basis of a Maxwell-Boltzmann distribution at 300 K. As the size

of the reactants increases, the number of accessible rovibrational states increases such that dissociation may not occur within the experimental time of flight, $\tau \sim 5 \times 10^{-4}$ s.[2] As a result, larger kinetic energies are required to dissociate the reactant in the experimental window and the apparent thresholds increase. To account for this kinetic shift, Rice-Ramsperger-Kassel-Marcus (RRKM) statistical theory[18, 19, 20] for unimolecular dissociation is incorporated into the modified LOC model, as seen below.

$$\sigma_j(E) = \left(\frac{n\sigma_{0,j}}{E}\right) \sum_i g_i \int_{E_{0,j}-E_i}^{E} \left[\frac{k_j(E^*)}{k_{tot}(E^*)}\right] (E-\varepsilon)^{N-1} P_{D1} d(\varepsilon) \qquad (2.4)$$

Here, ε is the energy deposited into internal modes of the reactant ion complex during collision, such that the energized molecule (EM) has an internal energy of $E^* = E_i + \varepsilon$. This value is integrated over all possible deposited energies that can lead to dissociation and is used to calculate the RRKM unimolecular rate constant for dissociation of channel j, $k_j(E^*)$, where $k_{tot}(E^*) = \Sigma\, k_j(E^*)$. The probability for dissociation in the experimental time frame is then given by $P_{D1} = 1 - \exp[-k_{tot}(E^*)\,\tau]$. Should the the EM dissociate within the experimental window, the integration in eq. (2.4) recovers eq. (2.3). The incorporation of $k_j(E^*)/k_{tot}(E^*)$ into the model ensures that competition for energy between multiple reaction channels is accurately represented by using statistical theory.[21, 22] This is accomplished by estimating the rate for each channel, j, as seen in eq. (2.5)

$$k_{tot}(E^*) = \sum_j k_j(E^*) = \sum_j d_j N_j^{\dagger}(E^* - E_{0,j})/h\rho(E^*) \qquad (2.5)$$

Here, d_j is the reaction degeneracy of channel j, $N_j^{\dagger}(E^* - E_{0,j})$ is the sum of rovibrational states of the transition state (TS), and $\rho(E^*)$ is the density of states of the EM at E^*.

Sequential dissociations can also be modeled by combining eq. (2.5) with the probability for further dissociation[23] given by eq. (2.6)

$$P_{D2} = 1 - e^{-k_2(E_2^*)\tau} \qquad (2.6)$$

where $E_2^* = E^* - E_{0,j} - T_1 - E_L$ is the internal energy of the product ion undergoing further dissociation and $T_1$and E_L represent the translational energy of the primary product and the internal energy of the neutral product, respectively. For every neutral ligand lost, uncertainties in the energy distribution of the remaining ion increase, so threshold analysis is typically limited to the one sequential dissociation.

The above equations are then convoluted over the kinetic energy distributions of the neutral and reactant ion. Experimental cross sections are fit by optimizing the adjustable parameters $\sigma_{0,j}$, N, and $E_{0,j}$ using a nonlinear least-squares optimization criterion. Once optimized, eq. (2.4) represents the threshold energy, $E_{0,j}$, which is equivalent to the 0 K dissociation energy for bond cleavages over a loose transition state. The uncertainties in these dissociation energies are determined from the range of parameters obtained from modeling multiple data sets, scaling the quantum chemical vibrational energies by $\pm 10\%$, varying the best fit N value by ± 0.1, changing the experimental time-of-flight up and down by a factor of 2, and including the uncertainty in the energy scale, ± 0.05 eV (lab).

2.3 Theoretical Methods

All low energy isomers are optimized at the B3LYP/6-311+G(d,p) level.[24, 25] In a previous study of similar hydrated complexes,[26] we showed that geometry optimizations, vibrational frequencies, and energetics calculated at this level yielded no appreciable differences from those calculated at alternate levels of theory, including B3LYP/6-311++G(d,p), BHandHLYP/6-311+G(d,p), BHandHLYP/6-311++G(d,p), and MP2(full)/6-311+G(d,p). Diffuse functions on heavy atoms were used at every step because of their importance in describing the hydrogen bonding characteristics of

hydration and solvation.[27, 28] To avoid SCF convergence failure and local minima, each structure is optimized four times with increasingly tighter SCF criteria and increasingly complex basis sets, beginning with 6-31G(d) and opt=loose. For all studies, relative energetics are obtained using single point energy (SPE) calculations at the B3LYP, B3P86,[29] M06,[30] and MP2(full)[31] levels of theory with a 3-311+G(2d,2p) basis set and zero-point energy (ZPE) corrections scaled by 0.989[32]. In some studies, additional levels of theory are implemented including Coulomb attenuating method (cam) B3LYP[33] and CCSD(T).[34] Our use of MP2 with full electron correlation is predicated on previous results that show that frozen core calculations can lead to anomalous metal cation binding affinities.[35, 36, 37] Relative energies of reactant and product isomers are also calculated at the relevant experimental temperatures using thermal corrections scaled by 0.989. Theoretical 0 K BDEs are calculated from the difference in energies of the ground reactant and product isomers and compared to experiment. Basis set superposition error (BSSE) corrections determined to the full counterpoise level[38, 39] are also made. In cases where theoretical spectra are generated, these frequencies have been scaled by 0.956 – 0.959 to provide the best match with our experiment. This range is similar to the value of 0.956,[40, 41] which is typically used for these types of studies. All quantum chemical calculations were performed using the Gaussian 09 suite of programs.[42]

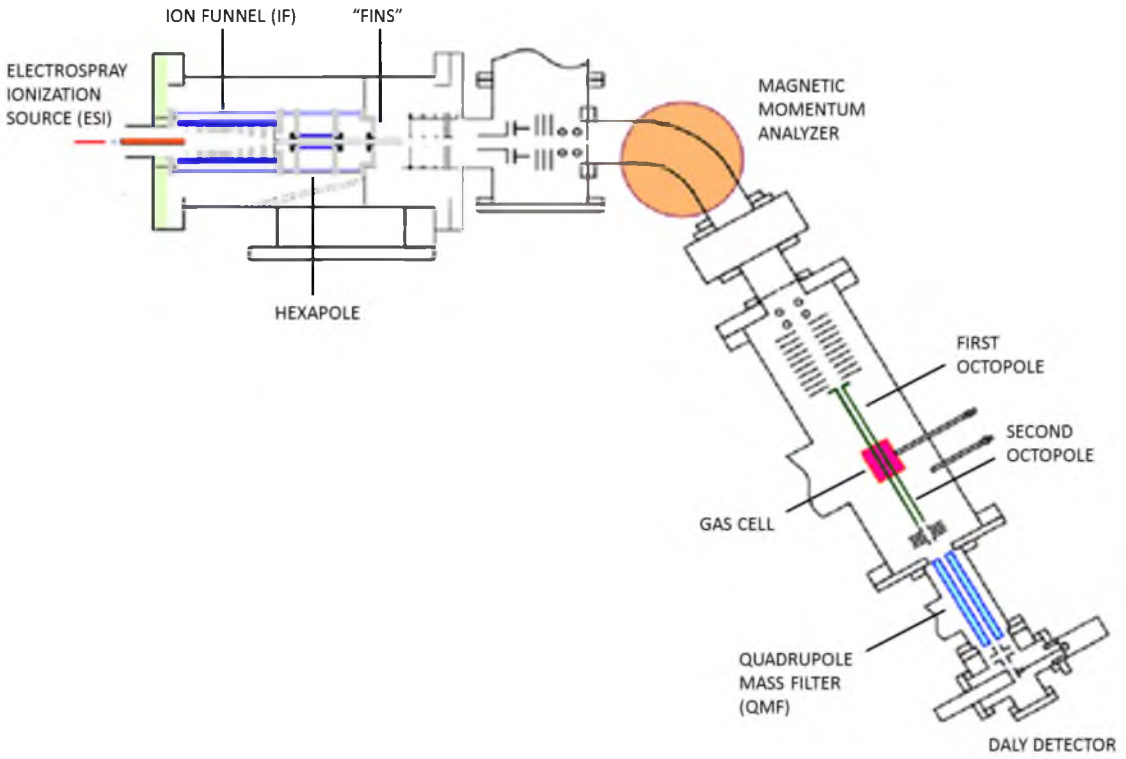

Figure 2.1 Schematic of the guided ion beam tandem mass spectrometer.

2.4 References

[1]Ervin, K. M.; Armentrout, P. B., J. Chem. Phys. **83,** 166 (1985)

[2]Muntean, F.; Armentrout, P. B., J. Chem. Phys. **115,** 1213 (2001)

[3]Kim, T.; Tolmachev, A. V.; Harkewicz, R.; Prior, D. C.; Anderson, G.; Udseth, H. R.; Smith, R. D., Anal. Chem **72,** 2247 (2000)

[4]Shaffer, S. A.; Prior, D. C.; Anderson, G. A.; Udseth, H. R.; Smith, R. D., Anal. Chem. **70,** 4111 (1998)

[5]Shaffer, S. A.; Tolmachev, A.; Prior, D. C.; Anderson, G. A.; Udseth, H. R.; Smith, R. D., Anal. Chem. **71,** 2957 (1999)

[6]Moision, R. M.; Armentrout, P. B., J. Am. Soc. Mass Spectrom. **18,** 1124 (2007)

[7]Heaton, A. L.; Moision, R. M.; Armentrout, P. B., J. Phys. Chem. A **112,** 3319 (2008)

[8]Heaton, A. L.; Ye, S. J.; Armentrout, P. B., J. Phys. Chem. A **112,** 3328 (2008)

[9]Carl, D. R.; Moision, R. M.; Armentrout, P. B., J. Am. Soc. Mass Spectrom. **20,** 2312 (2009)

[10]Carl, D. R.; Moision, R. M.; Armentrout, P. B., Int. J. Mass Spectrom. **265,** 308 (2007)

[11]Cooper, T. E.; Armentrout, P. B., Chem. Phys. Lett. **486,** 1 (2010)

[12]Dalleska, N. F.; Honma, K.; Sunderlin, L. S.; Armentrout, P. B., J. Am. Chem. Soc. **116,** 3519 (1994)

[13]Aristov, N.; Armentrout, P. B., J. Phys. Chem. **90,** 5135 (1986)

[14]Daly, N. R., Rev. Sci. Instrum. **31,** 264 (1960)

[15]Beyer, T. S.; Swinehart, D. F., Commun. ACM **16,** 379 (1973)

[16]Stein, S. E.; Rabinovich, B. S., Chem. Phys. Lett. **49,** 183 (1977)

[17]Stein, S. E.; Rabinovitch, B. S., J. Chem. Phys. **58,** 2438 (1973)

[18]Gilbert, R. G.; Smith, S. C., *Theory of Unimolecular and Recombination Reactions.* Blackwell Scientific: London, 1990.

[19]Holbrook, K. A.; Pilling, M. J.; Robertson, S. H., *Unimolecular Reactions*. 2nd ed.; Wiley: New York, 1996.

[20]Truhlar, D. G.; Garrett, B. C.; Klippenstein, S. J., J. Phys. Chem. **100,** 12771 (1996)

[21]Rodgers, M. T.; Ervin, K. M.; Armentrout, P. B., J. Chem. Phys. **106,** 4499 (1997)

[22]Rodgers, M. T.; Armentrout, P. B., J. Chem. Phys. **109,** 1787 (1998)

[23]Armentrout, P. B., J. Chem. Phys. **126,** 234302 (2007)

[24]Becke, A. D., J. Chem. Phys. **98,** 5648 (1993)

[25]Lee, C.; Yang, W.; Parr, R. G., Phys. Rev. B **37,** 785 (1988)

[26]Cooper, T. E.; Carl, D. R.; Armentrout, P. B., J. Phys. Chem. A **113,** 13727 (2009)

[27]Peschke, M.; Blades, A. T.; Kebarle, P., J. Am. Chem. Soc. **122,** 10440 (2000)

[28]Pavlov, M.; Siegbahn, P. E. M.; Sandstrom, M., J. Phys. Chem. A **102,** 219 (1998)

[29]Perdew, J. P., Phys. Rev. B **33,** 8822 (1986)

[30]Zhao, Y.; Truhlar, D. G., Theor. Chem. Acc. **120,** 215 (2008)

[31]Möller, C.; Plesset, M. S., Phys. Rev. **46,** 618 (1934)

[32]Bauschlicher, C. W., Jr.; Maitre, P. J., J. Phys. Chem. **99,** 3444 (1995)

[33]Yanai, T.; Tew, D. P.; Handy, N. C., Chem. Phys. Lett. **393,** 51 (2004)

[34]Bartlett, R. J., Ann. Rev. Phys. Chem. **32,** 359 (1981)

[35]Petrie, S., Chem. Phys. Lett. **283,** 131 (1998)

[36]Hoyau, S.; Norrman, K.; McMahon, T. B.; Ohanessian, G., J. Am. Chem. Soc. **121,** 8864 (1999)

[37]Sannigrahi, A. B.; Nandi, P. K.; Schleyer, P. v. R., J. Am. Chem. Soc. **116,** 7225 (1994)

[38]Boys, S. F.; Bernardi, R., Mol. Phys. **19,** 553 (1970)

[39]van Duijneveldt, F. B.; van Duijneveldt-van de Rijdt, J. G. C. M.; van Lenthe, J. H., Chem. Rev. **94,** 1873 (1994)

[40]O'Brien, J. T.; Williams, E. R., J. Phys. Chem. A **112,** 5893 (2008)

[41]Cooper, T. E.; O'Brien, J. T.; Williams, E. R.; Armentrout, P. B., J. Phys. Chem. A **114,** 12646 (2010)

[42]Frisch, M. J.; Trucks, G. W.; Schlegel, H. B.; Scuseria, G. E.; Robb, M. A.; Cheeseman, J. R.; Scalmani, G.; Barone, V.; Mennucci, B.; Petersson, G. A.; Nakatsuji, H.; Caricato, M.; Li, X.; Hratchian, H. P.; Izmaylov, A. F.; Bloino, J.; Zheng, G.; Sonnenberg, J. L.; Hada, M.; Ehara, M.; Toyota, K.; Fukuda, R.; Hasegawa, J.; Ishida, M.; Nakajima, T.;

Honda, Y.; Kitao, O.; Nakai, H.; Vreven, T.; Montgomery, J. A.; Peralta, J. E.; Ogliaro, F.; Bearpark, M.; Heyd, J. J.; Brothers, E.; Kudin, K. N.; Staroverov, V. N.; Kobayashi, R.; Normand, J.; Raghavachari, K.; Rendell, A.; Burant, J. C.; Millam, J. M.; Iyengar, S. S.; Tomasi, J.; Cossi, M.; Rega, N.; Millam, J. M.; Klene, M.; Knox, J. E.; Cross, J. B.; Bakken, V.; Adamo, C.; Jaramillo, J.; Gomperts, R.; Stratmann, R. E.; Yazyev, O.; Austin, A. J.; Cammi, R.; Pomelli, C.; Ochterski, J. W.; Martin, R. L.; Morokuma, K.; Zakrzewski, V. G.; Voth, G. A.; Salvador, P.; Dannenberg, J. J.; Dapprich, S.; Daniels, A. D.; Farkas, O.; Foresman, J. B.; Ortiz, J. V.; Cioslowski, J.; Fox, D. J. *Gaussian 09, Revision A.02*, Gaussian Inc.: Pittsburgh, PA, 2009.

CHAPTER 3

HYDRATED COPPER ION CHEMISTRY: GUIDED ION BEAM AND THEORETICAL INVESTIGATION OF $Cu^{2+}(H_2O)_n$ (n = 7 – 10)

3.1 Introduction

The copper ion is involved in many biological processes,[1, 2, 3, 4, 5] This includes its role in many key enzymes[6, 7, 8, 9, 10, 11] where unique coordination environments favor metal-specific binding.[12] When these binding sites are infiltrated by nonintended metals, it can be toxic to the organism. In this regard, copper is the most common toxic heavy metal used industrially.[5] In both biological and environmental settings, the copper ion is often found in a hydrated form, predominantly as the Cu^{2+} species, although Cu^{+} and $CuOH^{+}$ also exist in substantial concentrations.[13] For these reasons, a fundamental understanding of hydrated copper ion chemistry is of prime importance.

Solvated copper ion chemistry is relatively complex and often departs from periodic trends found among other metals.[14, 15] A good example of this behavior is found in a study by Shvartsburg et al. who examined the collision-induced dissociation (CID) of a range of divalent metals bound to clusters of water.[15] They found that the typical dissociation pathway for these systems is loss of a neutral water molecule followed by the sequential loss of additional water molecules. A competing mechanism for complexes with fewer waters attached is charge separation of the ionic species to form $MOH^{+}(H_2O)_m$

and $H^+(H_2O)_{n-m-1}$. For most metal dications, this channel is not observed until the complex has shrunk to 2 – 4 waters. This behavior has been related to the relatively low second ionization energies (IEs) of those metals compared to the first IE of water. As the second IEs of the metals increase, so too do the maximum sizes, n_{max}, at which the charge separation mechanism can be seen.[15] At the high end of this spectrum is Be, which has a second IE = 18.2 eV and an n_{max} = 8, yet this value decreases to 6 for Cu according to Shvartsburg et al.[15] despite having a larger second IE, 20.29 eV.[16]

Studies to understand this complexity have examined multiple forms of copper ion hydrates including $Cu^{2+}(H_2O)_n$,[15, 17, 18, 19, 20, 21] $Cu^+(H_2O)_n$,[14, 22, 23, 24] and the charge separation product, $CuOH^+(H_2O)_n$.[13, 17, 25, 26, 27] In our laboratory, copper ion hydration studies began over 20 years ago with the threshold CID (TCID) investigation of $Cu^+(H_2O)_n$, n = 1 – 4.[23] Recently, in collaboration with Williams and O'Brien, we investigated $CuOH^+(H_2O)_n$, n = 2 – 9, using a combination of infrared photodissociation (IRPD) in the OH stretching region and theory.[26] It was found that the $CuOH^+(H_2O)_n$ system prefers an inner shell coordination number (CN) of 4 although contributions from CN = 5 were apparent for n = 7 and could not be ruled out for other complexes. The characterization of low-energy isomers in that study prompted a subsequent TCID study of $CuOH^+(H_2O)_n$, n = 1 – 4, which yielded comprehensive thermodynamic information for the dissociation of these complexes losing both OH and H_2O.[27]

Of particular relevance to the present study is work by Kebarle and coworkers who showed that solvated multiply charged metal ions could be transferred to the gas phase using electrospray ionization (ESI) techniques.[28, 29] This inspired subsequent experimental studies of $Cu^{2+}(H_2O)_n$ systems by Stace and coworkers[21, 30, 31] and Stone and

coworkers[17] as well as theoretical studies by Rios-Font et al.[19] and Bérces et al.[20] Common to each experimental study is that $Cu^{2+}(H_2O)_n$ complexes achieve maximum intensity at $n = 8$. Furthermore, theory predicts that isomers with $n \geq 4$ prefer CN = 4 and square planar geometries because of the destabilization of axial sites by Jahn-Teller distortion in this $3d^9$ complex.[32] Additional waters prefer hydrogen bonding in the second solvent shell as axial binding to the metal is 20 – 35 kJ/mol higher in energy, according to theory.[19, 20]

Although hydrated copper ion systems have been well-characterized, the thermodynamics of these systems are still incomplete. Previous efforts to provide this information include TCID studies from this lab of the $Cu^+(H_2O)_n$[23] and $CuOH^+(H_2O)_n$[27] systems. In the present work, we use TCID in a guided ion beam tandem mass spectrometer (GIBMS) to quantitatively investigate the thermochemistry of the $Cu^{2+}(H_2O)_n$ system, where $n = 7 – 10$. The present results represent the first experimentally determined BDEs for the $Cu^{2+}(H_2O)_n$ system. Unfortunately, smaller complexes are not accessible in these experiments because the charge separation decomposition pathway precludes their formation, as demonstrated below; however, speculative analysis of higher order dissociations provide some qualitative thermochemistry for $n = 5$ and 6.

3.2 Experimental and Theoretical Section

3.2.1 Instrumentation

Hydrated copper dications are created from a 10^{-4} M solution of $CuSO_4$ in neat water using electrospray ionization techniques. The solution is pumped through a stainless steel needle at a rate of 0.05 mL/hr and an applied voltage of ~2 kV. Ions then

enter the vacuum system through a 0.01" stainless steel inlet cap and drift through a 4" long capillary that is heated to 80 °C to desolvate large droplets. An 88 plate radio frequency (rf) ion funnel (IF)[33] with a DC gradient typically < 10V collects and focuses the ions emitted from the capillary to increase signal intensity. It is essential to maintain a gentle DC gradient to avoid collisional heating that can arise as a result of the multiple encounters with ambient gas in this region. Larger gradients often result in charge separation, which prohibits the formation of $Cu^{2+}(H_2O)_n$ complexes in the source. After the IF, ions are injected into an rf-only hexapole (250 V peak to peak) where they are cooled by > 10^4 thermalizing collisions with ambient gas.[34] This ensures that the ions subject to CID are well-defined by a Maxwell-Boltzmann distribution of rovibrational states at room-temperature, as shown previously.[27, 34, 35, 36, 37, 38, 39] A set of DC electrodes are located between each hexapole rod and act as an in-source fragmentation technique, as described in detail elsewhere.[37] Increasing the voltage on these electrodes tends to break hydrated ions into smaller complexes. However, increasing the voltage beyond the peak intensity for the $n = 8$ complex resulted primarily in an increase in the charge separation products. This was also previously seen by Cooper et al. for $Zn^{2+}(H_2O)_n$ complexes[40] and is likely a result of the relatively high second IEs for Zn and Cu of 17.96 eV and 20.29 eV, respectively.[16] As a result, we were unable to create $Cu^{2+}(H_2O)_n$ complexes where $n \leq 7$ with appreciable intensity for further study.

Kinetic-energy dependent CID cross sections of the $n = 8 - 10$ complexes were measured using our guided ion beam tandem mass spectrometer.[41, 42] Ions generated as described above are focused into a magnetic momentum analyzer for mass selection of the reactant ion. These ions are then decelerated to a known kinetic energy and injected

into an rf octopole ion guide[43] where they pass through a collision cell containing low pressures of Xe gas. Xe is an ideal choice for inducing dissociation as it is heavy, monatomic, polarizable and chemically unreactive, all of which increase the efficiency of the transfer of collision energy to internal modes.[23, 44, 45] Product and residual reactant ions drift out of the octopole where they are mass analyzed using a quadrupole mass filter before being detected using a Daly detector.[46]

3.2.2 Data Analysis

Intensities of the reactant and product ions are measured at three different pressures of Xe in the collision cell: ~0.2, 0.1, and 0.05 mTorr. These pressure dependent intensities are then converted into absolute cross sections using a Beer-Lambert law analogue, as described in detail elsewhere.[41, 47] Linear extrapolation of the cross sections to zero pressure rigorously removes the effects of multiple collisions, which are nonnegligible in the present system. Product intensities resulting from dissociation outside of the collision cell as well as detector noise are removed by subtracting the product ion intensities without gas in the collision cell from those with gas in the cell. Reactant ion intensity is measured at the beginning of each experiment as a function of a retarding potential applied to the octopole.[41] This intensity is then differentiated and fit to a Gaussian distribution to obtain the absolute zero of energy as well as the distribution of reactant ion kinetic energies, which is used in later analysis. The relative energy of the reactants is converted from the lab frame voltage, V_{lab}, to the center of mass energy, E_{CM}, using eq 3.1,

$$E_{CM} = qV_{lab}\, m/(m + M) \tag{3.1}$$

where m is the mass of the reactant neutral Xe, M is the mass of the reactant ion, and q is

the charge of the ion (here, 2).

Zero-pressure kinetic energy dependent cross sections for loss of a single ligand are analyzed using the empirical model shown in eq 3.2,

$$\sigma_j(E) = \sigma_0 \sum_i g_i (E + E_i - E_{0,j})^N / E \quad (3.2)$$

where σ_0 is an energy independent scaling factor, E is the relative collision energy, $E_{0,j}$ is an adjustable parameter representing the reaction threshold for channel j at 0 K, and N is an adjustable parameter that describes the energy deposition function.[42] The summation is over the rovibrational states of the reactant ion having energies E_i and populations g_i, where $\sum g_i = 1$. Molecular parameters needed for these calculations are taken from quantum chemical calculations of the ground structures, described below. Rovibrational states are directly counted using a Beyer-Swinehart-Stein-Rabinovitch[48, 49, 50] algorithm and are assigned populations, g_i, on the basis of a Maxwell-Boltzmann distribution at 300 K. As the size of reactants increases, so does the number of accessible rovibrational states, which increases the dissociative lifetime of the complexes. Near the threshold energy, these lifetimes can exceed the experimental time window, $\tau \sim 5 \times 10^{-4}$ s,[42] and therefore require energy in excess of the threshold if they are to dissociate before detection. This kinetic shift increases the apparent threshold energy and is accounted for using Rice-Ramsperger-Kassel-Marcus (RRKM) statistical theory[51, 52, 53] for unimolecular dissociation, which is incorporated into the cross section model as seen in eq 3.3.[54, 55]

$$\sigma_j(E) = \left(\frac{n\sigma_{0,j}}{E}\right) \sum_i g_i \int_{E_{0,j}-E_i}^{E} \left(k_j/k_{tot}\right)(E - \varepsilon)^{N-1} P_{D1}\, d(\varepsilon) \quad (3.3)$$

Here, ε is the energy deposited into internal modes of the reactant ion complex during collision, such that the energized molecule (EM) has an internal energy of $E^* = E_i$

+ ε, which is used to calculate the RRKM unimolecular rate constant for dissociation of channel j, $k_j(E^*)$ where $k_{tot}(E^*) = \Sigma\, k_j(E^*)$. The probability for dissociation in the experimental time frame is then given by $P_{D1} = 1 - \exp[-k_{tot}(E^*)\,\tau]$. Should the dissociative lifetime of the EM be shorter than the average experimental timeframe, the integration in eq 3.3 recovers eq 3.2. The incorporation of the ratio of $k_j(E^*)$ and $k_{tot}(E^*)$ into the model ensures that competition between reaction channels is accurately represented.[55]

Cross sections for the loss of a second water ligand are modeled by combining eq 3.3, which reproduces the cross section of the primary dissociation product, with the probability for further dissociation[56] given by eq 3.4,

$$P_{D2} = 1 - e^{-k_2(E_2^*)\tau} \tag{3.4}$$

where k_2 is the rate of the secondary dissociation and $E_2^* = E^* - E_{0,j} - T_1 - E_L$ is the internal energy of the product ion undergoing further dissociation. Statistical assumptions are used to assign the distributions for T_1 and E_L, which represent the translational energy of the primary products and the internal energy of the primary neutral product, respectively.[56]

Water loss for hydrated metal cation species is a heterolytic bond cleavage that can be characterized as proceeding over a loose transition state (TS).[57] In this work, these TSs are treated at the phase space limit (PSL) in which the transitional modes are rotors.[54] For the charge separation channel, a tight TS is involved instead, as discussed further below. All molecular parameters for the TSs and EMs needed to calculate the RRKM rate constants are taken from quantum chemical calculations described below. For both primary and secondary processes, the model cross sections of eqs 3.3 and 3.4 are

convoluted over the kinetic energy distributions of the neutral and ion reactants before comparison to experimental data. The fitting parameters in these equations ($\sigma_{0,j}$, N, and $E_{0,j}$) are then optimized using a nonlinear least squares criterion to reproduce the experimental data throughout the threshold region. The $E_{0,j}$ threshold energies obtained are equivalent to the 0 K binding energy of the ligand to the metal complex,[58] or in the case of the charge separation channel, the barrier along this potential energy surface. The uncertainties in these binding energies are determined from the range of parameters obtained from modeling multiple data sets, scaling the quantum chemical vibrational energies by ±10%, varying the best fit N value by ±0.1, changing the experimental time-of-flight up and down by a factor of 2, and including the uncertainty in the reactant ion voltage scale, ±0.05 eV (lab).

3.2.3 Computational Details

Multiple isomers of the $Cu^{2+}(H_2O)_n$ system, all doublet spin states, were geometry optimized and vibrational frequencies calculated at the B3LYP/6-311+G(d,p) level of theory,[59, 60] including isomers of CN = 4, 5, and 6 at each value of n. Relative energetics of isomers including zero point energy (ZPE) corrections are obtained using single point energy (SPE) calculations at the B3LYP, B3P86,[61] M06,[62] and MP2(full)[63] levels with a 6-311+G(2d,2p) basis set. In a previous study of similar hydrated complexes,[40] we showed that geometry optimizations, vibrational frequencies, and energetics calculated at the B3LYP/6-311+G(d,p) level yielded no appreciable differences from those calculated at alternate levels of theory, including B3LYP/6-311++G(d,p), BHandHLYP/6-311+G(d,p), BHandHLYP/6-311++G(d,p), and MP2(full)/6-311+G(d,p). Diffuse functions on heavy atoms were used at every step because of their importance in

describing the hydrogen bonding characteristics of hydration and solvation.[64, 65] The rate-limiting transition state (TS) for charge separation processes was identified by relaxed potential energy surface scans of the distance between the charge separation products, $CuOH^+(H_2O)_3 + H^+(H_2O)_3$ and $CuOH^+(H_2O)_4 + H^+(H_2O)_3$. Previous studies in the $Zn^{2+}(H_2O)_n$ system show that this step must be rate-limiting even for complicated rearrangements.[66]

Rotational constants and vibrational frequencies of the ground isomers scaled by 0.989[67] were used to calculate the densities and numbers of states for each complex in our statistical modeling analysis, as well as zero point energy (ZPE) conversions to obtain theoretical BDEs at 0 K and thermal corrections to 298 K, which represents the temperature of reactant ions generated in the source region. Basis set superposition errors (BSSE) in the full counterpoise (cp) limit were also calculated for dissociation of the lowest energy structures at each level of theory.[68, 69] All quantum chemical calculations were performed using the Gaussian 09 suite of programs.[70]

3.3 Results and Discussion

3.3.1 Theoretical Structures

Relative energies at 0 and 298 K of $Cu^{2+}(H_2O)_n$ isomers predicted by the different levels of theory are given in Table 3.1 with two low-energy isomers shown in Figure 3.1 for $n = 4 - 10$. For all complex sizes except $n = 5$, all levels of theory predict the same ground isomer at 298 K. We use an (x,y,z) nomenclature to describe each unique structure where x = CN and y and z are the number of waters in the second and third solvent shells, respectively. To further distinguish isomers, hydrogen bonding of second and third shell waters is denoted using an A/D nomenclature where A refers to a water

molecule accepting a single hydrogen bond and D refers to a water molecule donating a single hydrogen. Underscores following the (x,y,z) designation indicate the beginning of a different solvent shell, however, there are instances where waters bind to two separate solvent shells. In these cases, 0.5 is added to each participating shell in the (x,y,z) name and the description of that water following the (x,y,z) designation is included in the highest number solvent shell, as illustrated in Figure 3.2 for the (4,3.5,1.5)_2AD,AAD_2AA complex.

For $n = 4$, all levels of theory predict the ground isomer to be a square-planar (4,0) complex with Cu–O bond lengths of 1.97 Å. The hydrogens are rotated by 44° out of the plane established by the copper and oxygens, such that there are weak hydrogen bonding interactions between each adjacent water molecule. This isomer has a high level of symmetry, D_4. For $n = 5$, the (5,0) MP2(full)/M06 ground isomer at 298 K has a square pyramidal geometry. Cu-O bond lengths for waters at the base are 2.03 Å for waters with hydrogens pointing at the axial ligand (OCuO bond angle = 95°) and 1.99 Å for waters with hydrogens in the plane of the base (OCuO bond angle = 97°). The axially bound water has a Cu-O bond length of 2.20 Å. The (4,1)_AA B3LYP/B3P86 ground isomer remains square planar and populates the second solvent shell with an AA water. Cu-O bond lengths for the inner shell nonhydrogen bonding, inner shell hydrogen bonding, and outer-shell waters are 1.95, 1.99, and 3.72 Å, respectively. The dipole moments of the waters participating in hydrogen bonding point 22° and 30° away from the Cu center, whereas dipole moments of the waters not participating in hydrogen bonding are aligned with Cu.

For $n = 6$, the 298 K ground isomer has CN = 4 and a square planar geometry

with two second shell waters. At 0 K, MP2(full)/B3P86 predict the two second shell ligands are opposite of each other, (4,2)_2AA$_{trans}$, whereas they prefer to be next to each other, (4,2)_2AA$_{cis\text{-}twist}$, in the B3LYP/M06 ground configuration. These isomers are within 4 kJ/mol of one another at all levels of theory. (4,2)_2AA$_{trans}$ has Cu-O bond lengths of 1.96 and 3.73 Å for inner and outer shell waters, respectively. Dipole moments of the water ligands point away from the Cu by 21 - 40°. (4,2)_AA$_{cis\text{-}twist}$ has nonuniform inner shell Cu-O bond lengths because of different hydrogen bonding environments. Cu-O bond lengths of 1.95 and 1.94 Å are seen for first shell waters having one and two hydrogen bonds, respectively, whereas the water ligand not participating in hydrogen bonding has a slightly elongated bond length of 2.01 Å. Dipole moments for the waters with two or zero hydrogen bonds have dipole moments pointed at the Cu, whereas water molecules participating in one hydrogen bond have dipole moments that are skewed by 32 – 38°. Bond lengths for second shell waters are the same as those in the trans isomer. Note that there are two (4,2)_2AA$_{cis}$ configurations, see Table 3.1. The ground isomer, (4,2)_AA$_{cis\text{-}twist}$, predicts that the nonhydrogen bonding water ligand is perpendicular to the plane of the molecule. Moving the hydrogens back into the plane of the molecule to give the (4,2)_AA$_{cis\text{-}flat}$ structure is 5 – 7 kJ/mol higher in energy. Structures with 5–coordinate geometries are 2 – 25 kJ/mol higher at 298 K. In the (5,1)_AA isomer, the second shell water molecule binds to two inner shell waters in the base, whereas in the (5,1)_AA$_{axial}$ isomer, the second shell water molecule binds to inner shell waters in the base and in the axial position. The octahedral (6,0) complex is 8 – 10 (MP2(full)/M06) and ~35 (B3LYP/B3P86) above the (4,2) ground isomer.

For n = 7, the CN and inner shell geometry of the (4,3)_3AA ground isomer is

unchanged from $n = 6$. Cu-O bond lengths are 1.97 and 1.95 Å for inner shell waters with one and two hydrogen bonds and 3.75 Å for outer shell waters. Dipole moments for waters with two hydrogen bonds point at the Cu, whereas dipole moments for waters with just one hydrogen bond point 67° away from copper. Structures with larger CN (5 and 6) lie at least 3 and 22 kJ/mol higher in energy (298 K), respectively, see Table 3.1, with B3LYP/B3P86 results generally being ~11 and ~20 kJ/mol, respectively, higher than MP2(full)/M06 values. At $n = 8$, the (4,4)_4AA ground isomer has identical inner shell waters leading to uniform Cu-O bond lengths of 1.95 and 3.76 Å for first and second shell waters, respectively. Dipole moments for all waters point towards Cu.[18, 20] At this complex size, structures with larger CN (5 and 6) lie at least 19 and 21 kJ/mol higher in energy (298 K), respectively, see Table 3.1.

The 298 K ground isomer for $n = 9$, (4,4,1)_3AA,AAD_A, has a square-planar geometry with CN = 4 and is the smallest complex size with a water in the third solvent shell. Inner shell bond lengths are uniform at 1.95 Å, whereas second shell AA waters and the AAD water have Cu-O bond lengths of 3.77 and 3.67 Å, respectively. The third solvent shell A water has the longest Cu-O bond length investigated at 5.77 Å. At 0 K, MP2(full)/M06 predict the (5,4)_4AA structure to be the ground isomer with a square pyramidal geometry. The Cu center for this isomer is slightly higher than the plane formed by the four inner shell waters forming the base. Cu-O bond lengths of those four waters are 1.99 Å, whereas the axially bound water and the second shell waters (all bound to the base) have bond lengths of 2.26 and 3.81 Å, respectively. Energetic differences between these two CN = 4 and 5 structures are 4 – 5 kJ/mol for MP2(full)/M06, but 9 – 11 kJ/mol for B3LYP/B3P86 at 0 K (3 – 4 and 17 – 20 kJ/mol,

respectively, at 298 K).

For n = 10, the 10th water in the 298 K ground isomer, (4,4,2)_2AA,2AAD_2A, is placed opposite the initial A water in the third shell giving the isomer C_{2v} symmetry. Cu-O bond lengths are only slightly changed from n = 8 and 9 with inner shell lengths of 1.95 Å, second shell AA lengths of 3.77 Å, second shell AAD lengths of 3.69 Å, and third shell A lengths of 5.76 Å. At 0 K, MP2(full)/M06 prefers the 10th water be hydrogen bonded to the first shell axial ligand and a second shell water, hence the (5,4.5,0.5) designation. The Cu-O bond length for this water is 4.53 Å, which falls between those of the second and third solvent shells, which average ~3.8 and 4.8 Å, respectively. Cu-O bond lengths are unchanged from (5,4)_4AA of n = 9 except for the axially bound water and the second shell water participating in hydrogen bonding, which are now 2.28 and 3.61 Å, respectively. Energetic differences between these two isomers of n = 10 are ~5 kJ/mol at 0 K and increase to ~10 kJ/mol at 298 K for MP2(full)/M06, whereas B3LYP/B3P86 put this isomer 13 – 16 kJ/mol above the (4,4,2) ground structure (~ 30 kJ/mol at 298 K).

The transition states (TSs) for the charge separation processes are composed of two species, $CuOH^+(H_2O)_m$ and $H^+(H_2O)_{n-m-1}$. Competing with water loss at n = 7 is formation of $CuOH^+(H_2O)_3$ and $H^+(H_2O)_3$, which passes over TS[3+3]. The distance between the closest oxygens of each species at the TS is 3.85 Å, and the O-H bond distance between the hydroxyl oxygen and the H_3O^+ hydrogen is 2.92 Å. The OH ligand on the $CuOH^+(H_2O)_3$ species forms a HOCu bond angle of 109° and the remaining water ligands are all aligned such that bonding to the Cu center occurs via one of the two lone pairs on each molecule, as found previously.[27] Competing with water loss at n = 8 is

TS[4+3], which has an O-O distance between species of 4.05 Å, and an O-H distance between the hydroxyl oxygen and the H_3O^+ hydrogen of 3.15 Å. The OH ligand on the $CuOH^+(H_2O)_4$ species forms a HOCu bond angle of 111° and one water is bound in a second shell to two inner shell water ligands, as detailed previously.[27] Compared to $CuOH^+(H_2O)_3$, the dipole moments of the water ligands on $CuOH^+(H_2O)_4$ are more directly pointed towards the Cu center as a result of the hydrogen bonding between the two first shell waters and the second shell water.

3.3.2 Infrared Spectra

Infrared photodissociation (IRPD) spectra were previously measured by O'Brien et al. for the $Cu^{2+}(H_2O)_n$ system, where n = 6 – 10, at 215 K.[18] Good agreement was found between the theoretical and experimental spectra although no comparison was given for n = 9. For n = 6 – 8 and 10, the ground isomers found in that study are the same ones identified here at 298 K. To characterize the n = 9 ground isomer at 298 K, the ground isomer found by all four levels of theory in the present work is compared to the experimental spectra of O'Brien et al. in Figure 3.3b. To validate our characterization, we applied the same methods to the n = 8 spectrum and successfully reproduced the results of O'Brien et al., see Figure 3.3a. This comparison was used to determine a scaling factor of 0.959, which when applied to the theoretical frequencies, provided the best match with the experimental spectra. This scaling factor differs only slightly from that used in previous studies, 0.956.[18, 71]

For n = 9, the (4,4,1) ground isomer reasonably agrees with the experimental spectrum, although this isomer has two broad features below 3350 cm^{-1} that are not obvious in the experimental spectrum. Likewise, the (5,4) spectrum is consistent with the

experimental spectrum and no longer predicts intensity below 3300 cm^{-1}. The lack of intensity below 3300 cm^{-1} does not necessarily rule out the presence of (4,4,1) because photodissociation in the bonding-OH region (2800 – 3500 cm^{-1}) is often much less efficient than predicted by the calculated absorption spectra;[72, 73, 74] however, a distinct band in this region is clearly observed for the n = 10 complex, see Figure 3.3c. MP2(full) theory predicts that the (4,4,1) and (5,4) isomers have a relative free energy of only 0.7 kJ/mol at 215 K (1.4 kJ/mol for M06), such that the (5,4) isomer would exist in a 40:60 ratio with the (4,4,1) isomer. This would help explain the very low experimental intensity below 3350 cm^{-1}.

For n = 10, low-energy isomers found by O'Brien et al., (4,4,2) and (5,4,1), as well as two additional low-energy isomers found in the present study are compared to the experimental spectrum in Figure 3.3c. In accord with the analysis of O'Brien et al., the (4,4,2) structure achieves good agreement in the free OH stretching region; however, (5,4,1) provides a comparable match with relative intensities more similar to our experiment. (Notably, the details of the frequencies in the free OH region calculated here for (5,4,1) differ slightly from those shown by O'Brien et al. and do agree with the observed spectrum better.) The MP2(full)/M06 ground isomer at 0 K, (5,4.5,0.5), is clearly not as good a match with experiment nor is the next highest energy isomer predicted by B3LYP/B3P86, (4,5,1), although either could contribute to the observed spectrum. Unlike the n = 9 spectrum, a distinct peak below 3300 cm^{-1} can be seen in the experimental spectrum for n = 10. This is also consistent with the spectra predicted for both the (4,4,2) and (5,4,1) isomers, which MP2(full)/M06 predicts are low-lying at 298 K. At the 215 K temperature where the spectrum was obtained, (4,4,2) is predicted to be

the ground isomer at all levels of theory. The relative free energy of the (5,4,1) isomer is 2.0 – 2.6 kJ/mol higher in energy at the MP2(full)/M06 levels, respectively, such that its equilibrium population would be 19 – 25%. At the B3LYP/B3P86 levels, the relative energy of the (5,4,1) isomer is predicted to be 16 – 19 kJ/mol, which would exclude it from existing with any significant population.

Overall, these IRMPD results appear to provide evidence for both 4- and 5-coordinate structures of the $n = 9$ and 10 complexes but not of $n = 8$. The results are most consistent with relative energetics calculated at the MP2(full) level of theory, in agreement with previous results for analogous $Zn^{2+}(H_2O)_n$ complexes.[71] However, the IRPD spectra for $Cu^{2+}(H_2O)_n$ complexes can be reasonably reproduced using any level of theory utilized in the present work. The spectra of different isomers are not sufficiently distinct in most cases to provide a definitive assessment of the best level of theory.

3.3.3 TCID Results

Experimental cross sections for collision-induced dissociation with Xe were measured for $Cu^{2+}(H_2O)_n$, where $n = 8 – 10$ as shown in Figure 3.4. Starting with the largest complex, Figure 3.4c shows $Cu^{2+}(H_2O)_{10}$ colliding with Xe to form products, yielding sequential loss of water ligands with increasing energy. The low intensity of this reactant ion leads to the noisy results and prevented observation of appreciable intensities of charge separation products seen for smaller complexes. Interestingly, the cross section of the $n = 8$ channel crosses over that of $n = 9$ suggesting an enhanced stability of the former over the latter. This is clearly consistent with the highly symmetric (4,4) structure identified by IRPD spectroscopy[18] and theory at $n = 8$ and the addition of waters into a third solvent shell at $n = 9$.

Figure 3.4b shows $Cu^{2+}(H_2O)_9$ colliding with Xe to form products. The primary dissociation pathway consists of loss of a single water molecule to form $Cu^{2+}(H_2O)_8$, which is then followed by loss of an additional water to form $Cu^{2+}(H_2O)_7$ and charge separation of $n = 8$ to form $CuOH^+(H_2O)_4 + H^+(H_2O)_3$ (hereafter called [4+3]) at similar thresholds. At higher energies, charge separation to form $CuOH^+(H_2O)_3 + H^+(H_2O)_3$ ([3+3]) and water loss to form $Cu^{2+}(H_2O)_6$ also appear with similar apparent thresholds. The cross section of the $H^+(H_2O)_3$ product is slightly smaller than that of the total cross section for charge separation, given in black dots, and parallels its energy dependence. Clearly, the magnitudes of the cross sections for the singly charged metal hydroxide and proton bound water clusters should be identical; however, experimental and dynamical factors can prevent this from being observed. This has been seen in previous work[19, 66, 75] and is caused by poor collection efficiency for the lighter $H^+(H_2O)_3$ product as a result of the large kinetic energies given to both products after passing over the Coulombic barrier during charge separation (see below). Because of momentum conservation, the lighter proton bound water cluster receives a higher velocity and can be scattered backward in the laboratory frame. Careful focusing can retrieve these products, however, at the cost of losing intensity of the parent complex. Because of the competition between water loss and charge separation starting at $n = 8$, we were unable to form reactants smaller than $n = 8$ with appreciable intensity in the source region. It is also interesting to note that the $Cu^{2+}(H_2O)_4$ cross section is larger than that of $Cu^{2+}(H_2O)_5$ at higher collision energies. This indicates that the $n = 4$ complex is entropically favored, which is consistent with it having a highly symmetric (D_4) square planar geometry, as found theoretically here, see Figure 3.1.[19, 20]

Figure 3.4a shows $Cu^{2+}(H_2O)_8$ colliding with Xe to form products. Here, the products are the same as those in Figure 3.4b, with the exception of $CuOH^+(H_2O)_4$, which unfortunately was not collected at the time of the experiment. Its presence can be inferred from the observation that the $H^+(H_2O)_3$ product cross section has a lower threshold energy than $CuOH^+(H_2O)_3$, just as in Figure 3.4b. Multiple attempts to recollect these data including all charge separation products were unsuccessful. We believe this failure can be attributed gradual changes in the pumping efficiency that have led to higher pressure in the source region, which induce the formation of metastable ions that charge separate before reactant ion selection. In some recent studies on similar systems, this issue can be overcome by utilizing the in-source fragmentation technique to shift the reactant population towards more stable ions. However, this procedure usually comes at the cost of signal intensity, which is already low for the $Cu^{2+}(H_2O)_n$ system. As a consequence, this technique could not be used without depleting the reactant beam to the point where signal was no longer adequate for quantitative studies.

3.3.4 Modeling of Experimental Cross Sections

Cross sections for the first and second water loss products resulting from collisions of $Cu^{2+}(H_2O)_n$, $n = 8 - 10$, with Xe after extrapolation to zero pressure are shown in Figure 3.5. We model these cross sections for the $n = 8 - 10$ reactants in several ways: a) the total cross sections are analyzed using eq 3.3, b) cross sections for loss of one and two H_2O ligands are analyzed using eqs 3.3 and 3.4, and c) competition with the charge separation channels is included. Optimized parameters for all three approaches are given in Table 3.2. For a given reactant, the difference between the primary and secondary thresholds can be measured with more precision than the absolute

values for each threshold because many systematic sources of uncertainty cancel. In our modeling, threshold energies correspond to 0 K BDEs for dissociation of the 298 K ground isomer of the reactant and the 0 K ground isomer for the product.[66] When modeling the $n = 8$ and 9 cross sections, theory agrees on which isomers to use, whereas different levels of theory make different predictions for the 0 K isomer of the $n = 9$ product formed from the $n = 10$ complex, see Table 3.1. Therefore, we model the cross section for the dissociation of a water from $n = 10$ considering both possibilities independently, as well as a composite analysis described below.

Modeling of the total cross section and primary and sequential water loss from the $n = 8$ complex, Figure 3.5a, yields a BDE for loss of a water from $n = 8$ of 0.76 ± 0.03 eV and from $n = 7$ of 1.07 ± 0.03 eV. Theory predicts two different (4,2) ground isomers at 0 K for $n = 6$, see Table 3.1; however, differences between the thresholds modeled with each product isomer were much less than the experimental error of the measurement. Consequently, only one set of values is reported here. The ability to measure the BDE for water loss from the $Cu^{2+}(H_2O)_7$ complex underscores the value of sequential modeling. Without it, we would be limited to measuring dissociation energies of complexes created in the source, which excludes $n = 7$.[39, 66, 75] Sequential modeling of the $n = 9$ complex, see Figure 3.5c, gives a threshold difference of 0.81 ± 0.03 eV, which is within the combined experimental uncertainties of the primary threshold value obtained for analysis of $n = 8$, 0.76 ± 0.03 eV. The total cross section and primary modeling of the $n = 9$ complex yield BDEs for loss of water from $n = 9$ that are essentially the same, 0.52 ± 0.06 and 0.50 ± 0.04 eV, respectively, as expected.

For $n = 10$, the threshold obtained assuming a (4,4,1) product is 0.51 ± 0.07 eV,

whereas the (5,4) product yields a threshold of 0.39 ± 0.06 eV. We also consider the possibility that both isomers are formed with relative thresholds corresponding to their calculated relative MP2(full) energies at 0 K, 0.05 eV, see Table 3.1. This composite model is shown in Figure 3.5f, where it can be seen that formation of (4,4,1) dominates the shape of the cross section at high energies because of its larger entropy. Nevertheless, the threshold remains essentially the same as when the (5,4) product alone is assumed, see Table 3.2. Clearly, if the (5,4) complex is actually higher in energy (as suggested by B3LYP/B3P86 results), its production will not be an appreciable contribution to the cross section, such that a threshold interpreted in this fashion should remain the same as found for the (4,4,1) product.

The threshold energy for the n = 10 complex assuming a (5,4) product is much lower than all theoretical BDEs (see detailed discussion in next section), whereas results assuming a (4,4,1) product exhibit good agreement. For this reason, modeling the loss of a sequential water from n = 10 is performed using the (4,4,1) isomer only, see Figure 3.5e. Analysis of the cross sections for the sequential water loss using eqs 3.3 and 3.4 yields a threshold difference of 0.50 ± 0.03 eV, which equals the primary threshold for water loss from n = 9 of 0.52 ± 0.06 eV, as expected.

We now consider the effect that the competing charge separation channels might have on the analysis. For n = 7 and 8, the competing charge separation pathways yield [3+3] and [4+3], respectively, and must pass over rate-limiting transition states TS[3+3] and TS[4+3], respectively. For n = 8, the $CuOH^+(H_2O)_4$ product was not collected at the time of the experiment, so competition from this charge separation channel was modeled using the $H^+(H_2O)_3$ product cross section. Because this lighter product was collected with

poor efficiency, its cross section was scaled to that for $CuOH^+(H_2O)_3$ near its peak magnitude. Now the competitive model yields a threshold for water loss of 0.76 ± 0.11 eV, the same value obtained without accounting for competition, and 0.75 ± 0.13 eV for the charge separation channel to form [4+3]. The best reproduction of the charge separation channel both in shape and absolute magnitude was obtained when the low frequency vibrational modes (< 900 cm^{-1}) were scaled up by 3%. Changes as small as ±2% resulted in noticeably poorer reproduction of the data. Notably, the relative threshold energies for these two processes can be more precisely given as 0.01 ± 0.02 eV, with charge separation being favored. As shown in Figure 3.5b, despite the similar threshold energies, the water loss channel is much larger in magnitude because it involves a loose transition state, whereas passing over the Coulomb barrier that is associated with charge separation (see discussion below) restricts this channel appreciably.

It is also possible to analyze this charge separation pathway starting from the n = 9 complex as a sequential dissociation competitive with water loss to form n = 7, see Figure 3.5d. Here, the thresholds for the two processes are again similar, 1.27 ± 0.11 eV for water loss and 1.23 ± 0.13 eV for charge separation, with a relative threshold difference of 0.04 ± 0.03 eV. This result is consistent with the relative thresholds obtained from the n = 8 reactant, and the absolute values are also in agreement as they are 0.77 and 0.73 eV above the loss of the first water at 0.50 eV.

It is important to realize that the $CuOH^+(H_2O)_3$ product can be formed either by losing water from $CuOH^+(H_2O)_4$ or by charge separation of n = 7 to yield [3+3]. The former process was previously found to have a 0 K threshold of 0.59 ± 0.07 eV.[26] Examination of Figure 3.4b shows that this energy is approximately consistent with the

relative onsets of $CuOH^+(H_2O)_4$ and $CuOH^+(H_2O)_3$. In addition, this sequential dissociation explains why the $CuOH^+(H_2O)_4$ reaches its maximum when the $CuOH^+(H_2O)_3$ product begins to be formed. Nevertheless, we also tried modeling the putative TS[3+3] charge separation process in competition with water loss from n = 7, which could be done starting from either n = 8 or 9, as illustrated in Figure 3.5d. Consistent results were obtained and yielded thresholds that are 0.5 eV higher than the amount of energy required to form $CuOH^+(H_2O)_3$ from dissociation of $CuOH^+(H_2O)_4$. This indicates that the [3+3] product is predominately formed by water loss from [4+3].

Table 3.2 also includes the entropies of activation evaluated at 1000 K for each complex size. These entropies are sensitive to rearrangements in the solvent shell as well as the formation of new solvent shells. This can be seen in the difference between $\Delta S^{\ddagger}_{1000}$ values of the (4,4,1) and (5,4) products from the (4,4,2) reactant isomer, which differ by 22 J/mol K. A particularly small value of 3 J/mol K is found for the n = 9 complex, resulting from the removal of the single third solvent shell water. This small value indicates that the water being eliminated is already relatively loosely bound, such that its dissociation does not appreciably change the entropy.

Because of the limited range of complexes investigated in the present work, we have also investigated whether modeling the tertiary (loss of three H_2O) and quaternary (loss of four H_2O) sequential products might provide useful thermodynamic information. Because our modeling program, CRUNCH, is programmed to examine only primary and secondary ligand loss channels, this necessitates taking thermochemistry from the relative thresholds for loss of two versus three water ligands and three versus four water ligands and ignoring the dominant primary and secondary channels. As these approaches are

therefore more speculative, these results are detailed in the Supporting Information.

3.3.5 Comparison of Primary versus Secondary and Theoretical Bond Energies

As noted above, there is good agreement between the primary and secondary bond energies determined using the models of the total cross sections and individual product cross sections. In general, the models of the total cross sections provide the best experimental information as fewer assumptions associated with the modeling are needed. Therefore, in the following we take the thresholds from the single channel modeling of the total cross section to be our best experimental BDEs for the $Cu^{2+}(H_2O)_n$ complexes where $n = 8 - 10$. For the $n = 7$ complex, we necessarily use the value obtained from our sequential modeling procedure including competition with the charge separation channel.

Theoretical BDEs were calculated using the same isomers employed for statistical modeling, see Table 3.1, and are compared to the experimental values in Table 3.3. All theoretical BDEs include zero point energy corrections calculated at the B3LYP/6-311+G(d,p) level and are given with and without counterpoise corrections for BSSE. Counterpoise corrections were < 5 kJ/mol for B3LYP, B3P86, and M06 levels and as large as 14 kJ/mol for MP2(full). Figure 3.6 shows the comparison of these theoretical BDEs including counterpoise corrections with primary and sequential experimental BDEs for water loss from $Cu^{2+}(H_2O)_n$ where $n = 7 - 10$.

The BDEs at all levels of theory agree well with each other, although MP2(full) values are lower than the DFT results for $n = 9$ and 10 and M06 values tend to be high. Theoretical BDEs generally overestimate the experimental values for $n = 8 - 10$ and are somewhat low for $n = 7$. Modeling the experimental cross section for $n = 10$ using the

(5,4) product yields a BDE of 37.6 ± 5.8 kJ/mol, which is 14 – 36 kJ/mol lower than theory. Modeling the same cross section using the (4,4,1) product yields a BDE that is higher, 49.2 ± 6.6 kJ/mol, and only 0 – 11 kJ/mol lower than theory, see Table 3.3. In general, differences between theoretical and experimental BDEs lead to mean absolute deviations (MADs) of 7 – 12 kJ/mol, which are somewhat larger than the mean experimental uncertainty of ~5 kJ/mol. MP2(full) yields results most consistent with experiment mainly because it reproduces the values for $n = 9$ and 10, whereas M06 and B3P86 reproduce the $n = 7$ BDE better. The MADs increase at all levels of theory when BSSE corrections are not included, appreciably for MP2(full).

Experimental BDEs decrease by ~25 kJ/mol for each water going from $n = 7$ to 9 and are nearly the same for $n = 9$ and 10. This is suggestive of the formation of a third solvent shell at $n = 9$, in which hydrogen bonded waters are significantly shielded from the metal center. A comparable result is found by all levels of theory, which show a relatively large drop in binding energies between the $n = 8$ and 9 complexes and comparable BDEs for $n = 9$ and 10.

3.3.6 Charge Separation

For $n = 8$, the threshold for charge separation to form [4+3] is found to be slightly lower in energy than the threshold for water loss to form $n = 7$. This finding is consistent with the results of Shvartsburg et al.[15] who found a *lower* limit to the critical complex size, n_{crit}, for Cu^{2+} to be 6. In a previous study, the discrepancy between n_{crit} values obtained in our laboratory and those obtained using other methods prompted a redefinition of n_{crit} as the largest value of n at which charge separation is energetically favored over water loss.[66] As the present results demonstrate that charge separation is the

favored pathway for n = 8, n_{crit} for the $Cu^{2+}(H_2O)_n$ system is therefore 8. As noted in the Introduction, given that the second IE of Cu, 20.29 eV,[16] is larger than that of Be, 18.2 eV, the present assignment of n_{crit} now seems consistent with the observation that n_{max} = 8 for Be.

Figure 3.7 shows calculated potential energy surfaces for dissociation of the n = 8 complex, including the products and rate-limiting transition states for the charge separation and water loss channels. Dissociation to lose water is calculated to be lower in energy than charge separation to form TS[4+3] by 3 – 29 kJ/mol, see Table 3.3, except at the B3P86 level where charge separation is favored by 4 kJ/mol. The variance in the reverse Coulomb barrier among theory is relatively small with values between 147 and 157 kJ/mol. Both B3P86 and B3LYP agree with experiments that these two channels have similar threshold energies, although all levels of theory exceed the absolute experimental values. Similar results for charge separation from n = 7 to form [3+3] are included in Table 3.3, with the potential energy surface (PES) provided in the Supporting Information. Comparison of the relative energies of the rate-limiting transition states of water loss and charge separation shows that charge separation is favored by 6 – 24 kJ/mol except at the MP2(full) level, which favors water loss by ~ 6 kJ/mol. This charge separation channel is not directly observed experimentally because it is masked by the sequential dissociation of water from the [4+3] product.

3.3.7 Comparison to Literature Theoretical Results

Bérces et al. studied the $Cu^{2+}(H_2O)_n$ system where n = 3 – 8 using a combination of static density functional theory (DFT) and ab initio molecular dynamics simulations.[20] Ground isomers found in that study tend to have inner shell waters with dipole moments

that do not point directly toward Cu, such that bonding occurs to one of two equivalent lone pair electrons. This differs from ground isomers found in the present study, which tend to have water dipole moments that are nearly collinear with Cu. The incremental binding energies for the n = 8 and 7 ground isomers found in the study of Bérces et al. are 99 and 116 kJ/mol, respectively, see Table 3.3. These values are 6 – 18 kJ/mol higher than the nearest theoretical values (M06) in the present work and are well outside the uncertainty of the experimental values. Our attempts to reproduce the unique orientation of the first shell waters in that study collapsed upon optimization to the same n = 8 isomer given in Figure 3.1. Calculations by Bérces et al. were also performed on the n = 8 isomer where all first shell hydrogens lie in the plane of the molecule, our (4,4)_4AA ground structure. The loss of a single water from this structure was calculated to be 86 kJ/mol, which agrees better with the present theoretical work.

Rios-Font et al. performed a theoretical study of $Cu^{2+}(H_2O)_n$, where n = 1 – 6, at the BLYP, B3LYP, MPWB1K, and BHLYP levels of theory with both 6-311++G(d,p) and cc-pVTZ basis sets. CCSD(T) calculations were also performed for n = 1 – 5. For n = 4 – 6, a four-coordinate inner shell with square planar geometry was found as the ground isomer at all levels of theory. For n = 2 and 3, the water ligands point directly at the copper center, whereas for n = 4, the water ligands are oriented such that the dipole moment of each is tilted, similar to the findings of Bérces et al.[19] Upon addition of a second shell water to form n = 5, hydrogen bonding appears to dominate the electrostatic interactions and dipole moments of all waters again point more closely towards the copper center, which agrees well with the present work. At n = 6, both the (4,2)_$2AA_{trans}$ and (4,2)_$2AA_{cis\text{-}twist}$ isomers are identified and differ by ~2 kJ/mol (B3LYP), the same

difference found in the present study. For B3LYP, relative energies between the most stable 4- and 5-coordinate isomers are 43, 17, and 22 kJ/mol (n = 4 – 6, respectively), which are on the same order as the differences of 37, 10 and 31 kJ/mol found here. Cu-O bond lengths for inner shell waters are identical to those found in the present study for n = 4 – 6.

3.3.8 Comparison to Other Metals: Mg^{2+}, Ca^{2+}, Sr^{2+}, Ba^{2+}, Fe^{2+}, Zn^{2+}, Cd^{2+}

The alkaline earth dications, Mg^{2+}, Ca^{2+} and Sr^{2+}, have rare gas electron configurations and are hydrated with well-defined inner shell geometries that prefer CN = 6.[38, 76, 77, 78] Ba^{2+} is large enough that evidence for both CN = 6 and 7 and possibly 8 exists.[79] In contrast, Zn^{2+} and Fe^{2+} have somewhat ambiguous inner shell CNs in which both CN = 5 and 6 are competitive.[40, 66, 71, 75] The ambiguity of the inner shell CN for Zn^{2+} is likely a result of having a d^{10} configuration and small ionic radius. Cd^{2+} also has a d^{10} configuration yet has a well-defined inner shell geometry (CN = 6),[39] presumably because its larger ionic radius can more easily accommodate a sixth ligand and adopt a stable octahedral geometry.

These results are in contrast to Cu^{2+}, which has a d^9 configuration. As discussed in our previous papers,[26, 27] this d^9 configuration has interesting implications. For instance, of the first row transition metals, Cu^{2+} has the highest crystal field stabilization energy (CFSE), as determined in the Irving-Williams series.[80] Typically, metal ions with large CFSEs tend to coordinate ligands in octahedral geometries; however, the partially filled e_g orbitals in a d^9 configuration undergo further splitting, which stabilizes the equatorial ligands at the cost of destabilizing the axial ligands. In the limit of this axial elongation,

these complexes resemble square-planar coordination. Indeed, Cotton and Wilkinson find that for many discrete complexes of Cu^{2+}, cases of tetragonally distorted octahedral complexes and square coordination cannot be sharply differentiated.[32] In the present work, square-planar geometries are preferred over octahedral geometries, although the five-coordinate square pyramidal geometry is competitive at MP2 and M06 levels of theory for $n = 9$ and $n = 5$, see Table 3.1.

3.3.9 Conversion to 298 K Thermodynamics

Using the calculated frequencies and rotational constants of the various complexes, a rigid rotor/harmonic oscillator approximation was employed to convert the 0 K binding energies into hydration enthalpies and free energies at 298 K, see Table 3.4. The uncertainties in these conversions are found by scaling the vibrational frequencies up and down by 10%. 0 K binding energies used here are the same as those used for comparison to theory in Table 3.3. It is important to note that there are many low frequency vibrations that correspond to hindered rotations and translations of the water ligands in these noncovalently bound systems. Therefore, treating these vibrations as harmonic oscillators may lead to inaccuracies, however, more exact treatments are beyond the scope of the present study.

Hydration enthalpies and the free energies of hydration increase with decreasing n despite the fact that the entropies of dissociation decrease going from $n = 10$ to 9 and increase from there to $n = 8$. This is indicative of the formation of a third solvent shell for $n = 9$, which is in accord with observations by O'Brien et al.[18] who found features in the IRPD spectra of $n = 10 - 12$ consistent with isomers having third solvent shells, as discussed above.

3.4 Conclusion

The kinetic energy dependent cross sections for collision-induced dissociation of $Cu^{2+}(H_2O)_n$ where $n = 8 - 10$ with Xe are investigated. The primary dissociation pathways consist of loss of a water followed by the sequential loss of additional waters until $n = 8$, at which point charge separation becomes the favored pathway. The data are interpreted to yield the first experimentally determined BDEs for the hydrated Cu^{2+} system. Primary and sequential BDEs for water loss are obtained from analysis of the cross sections using statistical modeling procedures and are found to be in good agreement with each other. Theoretical BDEs are calculated from the ground isomers at each complex size at the MP2(full), B3LYP, B3P86, and M06 levels of theory with a 6-311+G(2d,2p) basis set. Primary threshold energies for $n = 8 - 10$, the sequential threshold energy for $n = 7$, and the charge separation threshold for $n = 8$ are compared to theoretical 0 K BDEs at each level of theory and are found to be in reasonable agreement. More speculative thermochemistry for $n = 5$ and 6, as well as additional information for TS[3+3] can be found in the Supporting Information. Experimental 0 K BDEs are converted into thermodynamic values at 298 K using a rigid rotor/harmonic oscillator approximation that employs vibrational frequencies and rotational constants of the theoretical ground isomers.

3.5 Supporting Information

Experimental thresholds are typically extracted from modeling of either the primary or sequential products only. However, because of the limited range of complexes studied in the present work, we have investigated whether modeling the tertiary sequential product might provide useful thermodynamic information. In this

approach, we treat the $n - 2$ and $n - 3$ product cross sections as if they were the primary and sequential dissociation products, respectively.

To test the accuracy of this approach in the present system, we first modeled the tertiary processes of the n = 9 and 10 reactants, for which primary and secondary threshold data are available for comparison. For $n = 10$, we obtained a value of 1.10 ± 0.18 eV for dissociation of $n = 8$ to 7, and for $n = 9$, we obtained a value of 1.43 ± 0.07 eV for dissociation of $n = 7$ to 6. Both values are ~0.33 eV higher than the best experimental values discussed above, see Table 3.2, outside of the combined experimental uncertainties. As the zero pressure extrapolated cross sections for these small intensity higher energy products are relatively scattered, especially near threshold, a more accurate approach may be to model the cross sections directly from the high, medium, and low pressure data and linearly extrapolate the resulting thresholds to zero pressure. Using this approach for $n = 10$ results in an upper limit for dissociation of 0.98 ± 0.19 eV, within combined uncertainties of the experimental values of 0.76 ± 0.03 eV and well within the 0.88 – 0.96 eV range predicted by theory. For $n = 9$, this approach results in a value of 1.28 ± 0.10 eV for dissociation of $n = 7$ to 6, which is slightly larger than the value of 1.07 ± 0.03 eV obtained from secondary modeling, as well as the range of values given by theory of 0.94 – 1.01 eV. In both cases, the tertiary value is ~0.20 eV higher than our best value.

Modeling the zero pressure extrapolated cross sections for the $n = 8$ reactant yielding the $n = 6$ and 5 products resulted in a relative threshold of 1.86 ± 0.10 eV, see Figure 3.8a. Because theory predicts two different ground isomers for $n = 5$, (5,0) and (4,1), we modeled the cross section considering both possibilities. When the high,

medium, and low pressure cross sections are modeled directly the extrapolated zero-pressure threshold lowers to 1.52 ± 0.17 eV for the (5,0) product and 1.49 ± 0.16 eV for the (4,1) product. Because modeling these tertiary processes gives thresholds that are higher than those from the primary and sequential model, the value for $n = 6$ of 1.49 ± 0.16 represents an upper limit to the true threshold. As noted above, a more realistic value in this system is probably about 0.20 eV lower, 1.3 ± 0.2 eV.

Finally, we model the $n = 5$ and 4 cross sections from the $n = 8$ reactant to obtain a BDE energy for $n = 5$ in the same way that we modeled the $n = 6$ and 5 cross sections above, Tables 3.5 and 3.6. That is, we treat the $n - 3$ and $n - 4$ product cross sections as if they were the primary and sequential dissociation products, respectively. Because our pressure dependent studies of the $n = 8$ system only extended down to the $n = 5$ product, the high pressure data shown in Figure 3.4a is necessarily modeled. This quaternary sequential fit yields a BDE for $n = 5$ of 1.22 ± 0.16 eV assuming a (5,0) reactant and 1.28 ± 0.17 eV assuming a (4,1) reactant, see Figure 3.8b. Again, a more realistic value in this system is probably about 0.2 eV lower. We must also consider that as the pressure increases, the relative threshold energy decreases. This is because increased pressure more severely affects the higher energy product channels such that their thresholds are more shifted relative to the lower energy product channels. For $n = 8$ dissociating to form $n = 6$ and 5, relative threshold energies obtained at high pressure were ~0.4 eV lower than the zero pressure relative thresholds. Including these two correction factors (-0.2 eV, +0.4 eV) increases the thresholds from the (5,0) and (4,1) products by 0.2 eV to 1.4 ± 0.2 eV and 1.5 ± 0.2 eV, respectively.

As the complex size decreases, the BDEs increase because the charge of the metal is shared over fewer ligands. This trend is visible in Figure 3.9 as the energy between apparent thresholds for water loss increases, going from $n = 9$ to 5. At n = 9 and 10, the difference in BDE is quite small. This is indicative of the formation of a third solvent shell, where the dominant electrostatic force is hydrogen bonding rather than bonding from the Cu center. Experimental values for both $n = 5$ and 6 are larger than the range of theoretical values. That the experimental values from $n = 10$ to 5 gradually increase relative to the theoretical values suggests that the charge separation mechanism is becoming increasingly competitive.

Charge separation from $n = 8$ and 7 reactants results in the formation of [4+3] and [3+3] products, respectively. As discussed in the main text, formation of the $CuOH^+(H_2O)_3$ species from sequential decomposition of $CuOH^+(H_2O)_4$ is lower in energy than formation from charge separation of $n = 7$. This can be seen in Figure 3.4b as the onset of $CuOH^+(H_2O)_3$ is concomitant with the rapid decline in the $CuOH^+(H_2O)_4$ cross section. Indeed, the $CuOH^+(H_2O)_3$ threshold is ~ 0.6 eV higher in energy than the threshold for $CuOH^+(H_2O)_4$, which agrees well with the previously measured value for loss of H_2O from $CuOH^+(H_2O)_4$ of 0.59 ±0.07 eV.[27] This agreement suggests that the energy of the Coulomb barrier released to charge separation products after passing over the tight transition state (~1.6 eV) goes mainly into translation and is largely unavailable to internal modes, such that an additional 0.6 eV above the barrier is needed for $CuOH^+(H_2O)_4$ to sequentially dissociate to form $CuOH^+(H_2O)_3$. For completeness, the theoretical PES for dissociation of the $n = 7$ complex by water loss and charge separation is shown in Figure 3.10.

Table 3.1: Relative Calculated Enthalpy (ΔH_0) and Free Energies (ΔG_{298}) in kJ/mol of $Cu^{2+}(H_2O)_n$ Isomers[a]

n	name	literature[b]	MP2(full)	M06	B3LYP	B3P86
4	(4,0)		**0.0 (0.0)**	**0.0 (0.0)**	**0.0 (0.0)**	**0.0 (0.0)**
	(3,1)		59.2 (65.8)	58.2 (64.9)	48.6 (55.2)	49.4 (56.0)
5	(5,0)		**0.0 (0.0)**	**0.0 (0.0)**	10.2 (6.8)	12.1 (8.7)
	(4,1)_AA		3.0 (6.4)	**0.0** (3.4)	**0.0 (0.0)**	**0.0 (0.0)**
6	(4,2)_$2AA_{cis\text{-}twist}$	6AI (**0**)	0.8 **(0.0)**	**0.0 (0.0)**	**0.0 (0.0)**	1.2 **(0.0)**
	(4,2)_$2AA_{trans}$	6AII (3)	**0.0** (2.1)	0.6 (3.5)	1.2 (4.1)	**0.0** (1.7)
	(5,1)_AA	6B (9)	4.4 (2.3)	5.9 (4.6)	16.1 (14.8)	16.7 (14.2)
	(4,2)_$2AA_{cis\text{-}flat}$		5.7 (5.5)	5.7 (6.3)	6.7 (7.3)	6.1 (5.5)
	(6,0)	6C (22)	11.7 (7.8)	13.4 (10.3)	37.7 (34.6)	40.6 (36.3)
	(5,1)_AA_{axial}		15.8 (13.0)	17.3 (15.3)	26.7 (24.7)	27.4 (24.2)
7	(4,3)_3AA	7A (**0**)	**0.0 (0.0)**	**0.0 (0.0)**	**0.0 (0.0)**	**0.0 (0.0)**
	(5,2)_$2AA_{cis}$	7B (11)	5.5 (2.8)	7.6 (4.9)	16.9 (14.2)	18.3 (15.6)
	(5,2)_$2AA_{trans}$		10.3 (8.5)	9.7 (7.9)	18.1 (16.3)	18.5 (16.7)
	(4,2.5,0.5)_AA,AD_AA		23.5 (19.6)	28.0 (24.1)	20.1 (16.2)	20.4 (16.5)
	(6,1)_AA	7C (38)	26.7 (22.3)	27.8 (23.4)	45.7 (41.3)	48.2 (43.8)

Table 3.1 Continued

n	name	literature[b]	MP2(full)	M06	B3LYP	B3P86
8	(4,4)_4AA	8A (**0**)	**0.0 (0.0)**	**0.0 (0.0)**	**0.0 (0.0)**	**0.0 (0.0)**
	(5,3)_3AA	8B (21)	15.9 (19.0)	15.2 (18.7)	22.4 (25.9)	22.2 (25.7)
	(5,3)_2AA,AA_{ax}		18.5 (19.0)	21.3 (21.8)	27.1 (27.6)	27.9 (28.4)
	(6,2)_2AA	8C (40)	29.0 (21.1)	31.9 (24.0)	49.3 (41.4)	51.8 (43.9)
	(4,3.5,0.5)_2AA_{cis},AD_AA		26.1 (27.2)	30.8 (31.9)	21.5 (22.6)	21.3 (22.4)
	(4,3.5,0.5)_2AA_{trans},AD_AA		29.4 (30.6)	34.8 (36.0)	25.7 (26.9)	25.5 (26.7)
	(5,2.5,0.5)_AAD,AA_AA		30.1 (35.1)	33.4 (38.4)	29.4 (34.4)	40.2 (45.2)
	(5,2.5,0.5)_AD,AA_AA		37.2 (38.6)	40.7 (42.1)	39.9 (41.3)	40.2 (41.6)
n	name	literature[b]	MP2(full)	M06	B3LYP	B3P86
9	(4,4,1)_3AA,AAD_A		5.0 **(0.0)**	4.3 **(0.0)**	**0.0 (0.0)**	**0.0 (0.0)**
	(5,4)_4AA		**0.0** (2.8)	**0.0** (3.5)	9.1 (16.9)	11.2 (19.0)
	(4,4.5,0.5)_3AA,AD_AA		9.1 (9.7)	12.2 (13.5)	5.8 (11.4)	7.1 (12.7)
	(5,4)_3AA,AAax		8.7 (11.9)	8.3 (12.2)	16.4 (24.6)	18.0 (26.2)
	(5,4)_3AA,A		22.4 (22.9)	23.4 (24.6)	27.4 (32.9)	28.7 (34.2)
	(5,4)_2AA,AAD,AA		17.8 (24.4)	18.0 (25.3)	26.1 (37.7)	27.5 (39.1)

Table 3.1 Continued

n	name	literature[b]	MP2(full)	M06	B3LYP	B3P86
	(6,3)_3AA		23.0 (27.7)	24.1 (29.5)	40.6 (50.3)	43.4 (53.1)
	(4,4,1)_2AD,2AA_AA		30.3 (32.3)	36.0 (38.7)	23.6 (30.6)	24.3 (31.3)
	(4,4,1)_2AD,AA_2AA		33.0 (33.3)	39.8 (40.8)	25.3 (30.6)	26.4 (31.7)
	(4,3.5,1.5)_2AD,AAD_2AA		42.0 (41.1)	41.5 (41.3)	36.0 (40.1)	37.6 (41.7)
10	(4,4,2)_2AA,2AAD_2A	10A (**0**)	5.2 **(0.0)**	4.6 **(0.0)**	**0.0 (0.0)**	**0.0 (0.0)**
	(5,4,1)_4AA_A	10B (10)	2.2 (3.7)	2.2 (4.3)	10.8 (17.5)	13.5 (20.2)
	(4,5,1)_3AA,2AD_AA		7.0 (8.5)	11.0 (13.1)	5.4 (12.1)	6.9 (13.6)
	(5,4.5,0.5)_3AA,AD_AA		**0.0** (9.8)	**0.0** (10.4)	12.9 (27.9)	15.6 (30.6)
	(6,4)_4AA	10C (32)	10.7 (12.9)	10.3 (13.1)	35.1 (42.5)	43.7 (51.1)
	(5,5)_3AA,AD2,AA2		10.3 (15.4)	13.3 (19.0)	22.2 (32.5)	25.3 (35.6)
	(4,5,1)_2AD,2AA_2AA		14.4 (16.3)	20 (22.8)	13.6 (21.0)	15.5 (22.9)
	(5,5)_4AA,A		6.6 (20.7)	9.6 (24.3)	18.6 (37.9)	22.1 (41.4)

[a] ΔG_{298} values given in parentheses. Single point energies calculated at the level shown using a 6-311+G(2d,2p) basis set with geometries, zero point energy corrections (scaled by 0.989), and thermal corrections calculated at the B3LYP/6-311+G(d,p) level of theory. Ground isomers indicated by bold. [b] Results from ref. 18 calculated at the B3LYP/LACV3P**++ level.

Table 3.2: Optimized Parameters of Eqs 3.3 and 3.4 from Analysis of CID Cross Sections[a]

n	reactant	product	σ_0[b]	N[b]	E_0[c] (eV)	E_0[b] PSL (eV)	$\Delta S^{\dagger}_{1000}$ (J/mol K)
8	(4,4)	(4,3)	71 (4)	0.9 (0.1)	0.99 (0.08)	0.76 (0.03)	50 (5)
	(4,4)	(4,3)[d]	69 (4)	0.9 (0.1)		0.76 (0.03)	47 (5)
		(4,2)[d]	43 (8)			1.83 (0.05)	
	(4,4)	(4,3)	73 (8)	1.0 (0.1)		0.76 (0.11)	50 (5)
		TS[4+3]	39 (22)			0.75 (0.13)	
	(4,4)	(4,3)[e]	71 (6)	0.8 (0.1)		0.73 (0.04)	50 (3)
		(4,2)[e]	74 (13)			1.78 (0.04)	
		TS[3+3][e]	15 (14)			1.68 (0.03)	
9	(4,4,1)	(4,4)	122 (3)	0.8 (0.2)	1.06 (0.08)	0.52 (0.06)	3 (5)
	(4,4,1)	(4,4)[d]	127 (5)	0.8 (0.2)		0.50 (0.04)	3 (5)
		(4,3)[d]	62 (6)			1.31 (0.06)	
	(4,4,1)	(4,4)[e]	127 (5)	0.8 (0.2)		0.50 (0.07)	
		(4,3)[e]	62 (7)			1.27 (0.11)	
		TS[4+3][e]	59 (20)			1.23 (0.13)	

Table 3.2 Continued

n	reactant	product	σ_0 [b]	N [b]	E_0 [c] (eV)	E_0 [b] PSL (eV)	$\Delta S^{\dagger}_{1000}$ (J/mol K)
10	(4,4,2)	(5,4)	107 (8)	1.0 (0.1)	0.89 (0.07)	0.39 (0.06)	18 (4)
	(4,4,2)	(4,4,1)	103 (11)	1.0 (0.1)	0.96 (0.07)	0.51 (0.07)	40 (4)
	(4,4,2)	(5,4)+(4,4,1)[f]	104 (9)	1.0 (0.1)		0.37 (0.05)	40 (4)
	(4,4,2)	(4,4,1)[d]	101 (11)	1.1 (0.1)		0.49 (0.03)	40 (4)
		(4,4)[d]	72 (10)			0.99 (0.04)	

[a] Uncertainties (one standard deviation) in parentheses. Thresholds obtained using single channel modeling of eq. 3 unless otherwise noted. [b] Parameters for modeling where lifetimes effects are taken into account. [c] Threshold values for modeling where lifetime effects are not included. [d] Sequential dissociation modeling using eqs. 3.3 and 3.4. [e] Sequential competitive dissociation modeling using eqs. 3.3 and 3.4. TS[3+3] and TS[4+3] = transition state to charge separation products (number of waters in each fragment). [f] Composite modeling using eq 3.3 and a difference in thresholds for the (5,4) and (4,4,1) isomers given by the MP2(full) theoretical results.

Table 3.3: Comparison of Experimental 0 K Bond Energies (kJ/mol) to Theoretical Values[a]

n=	reactant	product	Experiment[b]	MP2(full)[c]	M06 [c]	B3LYP [c]	B3P86 [c]	Literature[d]
7	(4,3)	(4,2)	101.3 ± 2.9	90.8 (100.1)	97.8 (100.9)	90.3 (93.5)	95.3 (98.6)	116
	(4,3)	TS[3+3]		(106.5)	(95.2)	(74.1)	(74.3)	
	(4,3)	[3+3][e]		(-48.0)	(-70.1)	(-88.4)	(-87.7)	
8	(4,4)	(4,3)	73.3 ± 3.9	86.4 (95.3)	93.0 (96.0)	85.4 (88.5)	87.3 (90.4)	99
		TS[4+3]	72.4 ± 12.5	(124.5)	(110.5)	(92.0)	(86.0)	
	(4,4)	[4+3][e]		(-22.9)	(-44.4)	(-64.5)	(-65.1)	
9	(4,4,1)	(4,4)	50.2 ± 5.8	54.0 (64.7)	62.1 (64.0)	60.4 (63.5)	63.6 (66.9)	
10	(4,4,2)	(4,4,1)	49.2 ± 6.6	48.7 (62.3)	60.2 (62.1)	57.1 (61.2)	60.1 (64.4)	
	(4,4,2)	(5,4)	37.6 ± 5.8	51.4 (57.3)	53.3 (57.8)	68.5 (70.4)	73.7 (75.5)	
MAD[f]			5.3[g]	7.0 (12.7)	11.6 (12.5)	10.3 (12.1)	11.1 (12.9)	

[a] Theoretical values with (and without) BSSE corrections. [b] Values from Table 3.2. [c] Single point energies calculated at the indicated level using a 6-311+G(2d,2p) basis set and B3LYP/6-311+G(d,p) geometries and zero point energies. [d] Bond dissociation energies from Bérces et al.[20] [e] [m + 3] = products of charge separation mechanism (number of waters in each fragment). [f] Mean absolute deviations from experimental BDEs excluding charge separation. [g] Mean experimental uncertainty.

Table 3.4: Conversion of 0 K Thresholds to 298 K Enthalpies and Free Energies (kJ/mol)[a]

n	reactant	product	ΔH_0[b]	$\Delta H_{298} - \Delta H_0$[c]	ΔH_{298}	$T\Delta S_{298}$[c]	ΔG_{298}
7	(4,3)	(4,2)	101.3 (2.9)	4.6 (0.4)	105.9 (2.9)	43.7 (1.0)	62.2 (3.1)
8	(4,4)	(4,3)	73.3 (3.9)	2.3 (0.4)	75.6 (3.9)	40.0 (1.1)	35.6 (4.0)
	(4,3)	TS[4+3]	72.4 (12.5)	5.6 (0.4)	77.9 (12.5)	64.7 (1.5)	-13.8 (12.6)
9	(4,4,2)	(4,4)	50.2 (5.8)	1.5 (0.5)	49.7 (5.8)	27.0 (1.0)	24.6 (5.9)
10	(4,4,2)	(4,4,1)	49.2 (6.6)	1.9 (0.5)	51.1 (6.6)	38.5 (1.1)	12.7 (6.7)
	(4,4,2)	(5,4)	37.6 (5.8)	0.0 (0.5)	37.6 (5.8)	30.6 (1.5)	7.0 (6.0)

[a] Uncertainties in parentheses. [b] Experimental values from this work (Table 3.3). [c] Values are calculated from the vibrational frequencies and rotational constants calculated at the B3LYP/6-311+G(d,p) level using ground isomers indicated by MP2(full) single point energy calculations. Uncertainties are found by scaling the frequencies up and down by 10%.

Table 3.5: Optimized Parameters of Eqs 3 and 4 from Analysis of CID Cross Sections[a]

n	reactant	product	σ_0 [b]	N [b]	E_{rel} [b] PSL (eV)
5[c]	(5,0)	(4,0)	3 (15)	1.7 (0.2)	1.42 (0.2)
	(4,1)	(4,0)	3 (15)	1.7 (0.2	1.48 (0.2)
6	(4,2)	(5,0)	41 (16)	0.4 (0.2)	1.32 (0.2)
	(4,2)	(4,1)	42 (16)	0.4 (0.2)	1.29 (0.2)

[a] Uncertainties (one standard deviation) in parentheses. Thresholds obtained using single channel modeling of eqs 3.3 and 3.4. [b] Parameters for modeling where lifetime effects are taken into account. [c] Relative energy from sequential modeling of the quaternary product. [d] Relative energy from sequential modeling of the tertiary product.

Table 3.6: Comparison of Experimental 0 K Bond Energies (kJ/mol) to Theoretical Values[a]

n=	reactant	product	Experiment[b]	MP2(full)[c]	M06[c]	B3LYP[c]	B3P86[c]
5	(5,0)	(4,0)	137 ± 19[d]	106.6 (117.4)	113.9 (117.8)	99.0 (102.4)	101.6 (105.1)
	(4,1)	(4,0)	143 ± 19[d]	104.5 (114.4)	114.3 (117.8)	109.1 (112.5)	113.7 (117.2)
6	(4,2)	(5,0)	127 ± 19[e]	95.5 (105.1)	106.2 (109.4)	110.8 (114.1)	116.8 (120.2)
	(4,2)	(4,1)	124 ± 19[e]	98.5 (108.0)	106.2 (109.4)	100.6 (103.9)	104.7 (108.1)

[a] Theoretical values with (and without) BSSE corrections. [b] Values from Table 3.1. [c] Single point energies calculated at the indicated level using a 6-311+G(2d,2p) basis set and B3LYP/6-311+G(d,p) geometries and zero point energies. [d] Thresholds obtained from sequential modeling of the quaternary dissociation from $n = 8$. [e] Thresholds obtained from sequential modeling of the tertiary dissociation from $n = 8$.

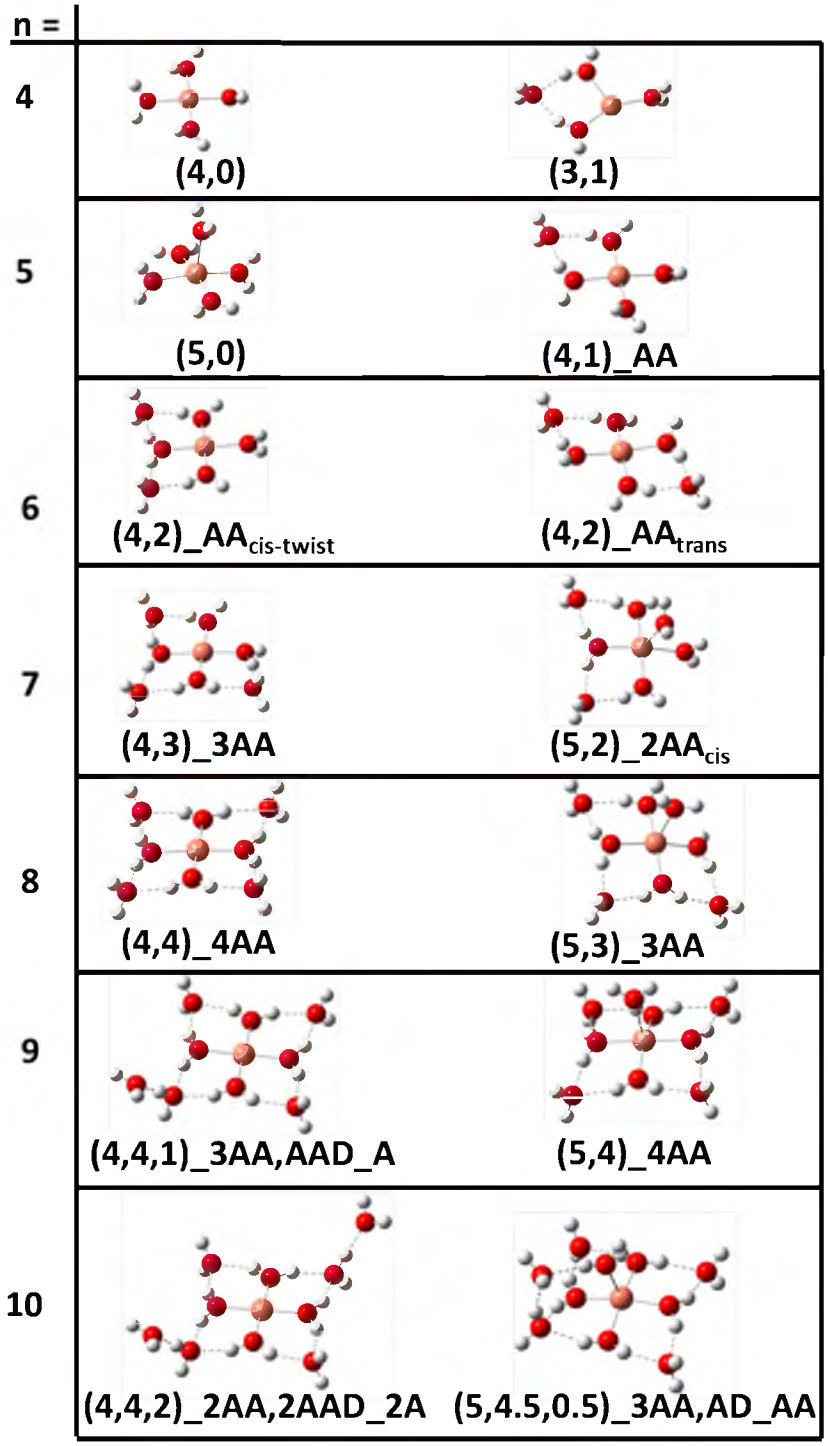

Figure 3.1: Low-lying isomers of $Cu^{2+}(H_2O)_n$ optimized at the B3LYP/6-311+G(d,p) level. 298 K ground states are shown on the left. All but (3,1), (5,2), and (5,3) are 0 K or 298 K ground isomers at some level of theory, Table see 3.1.

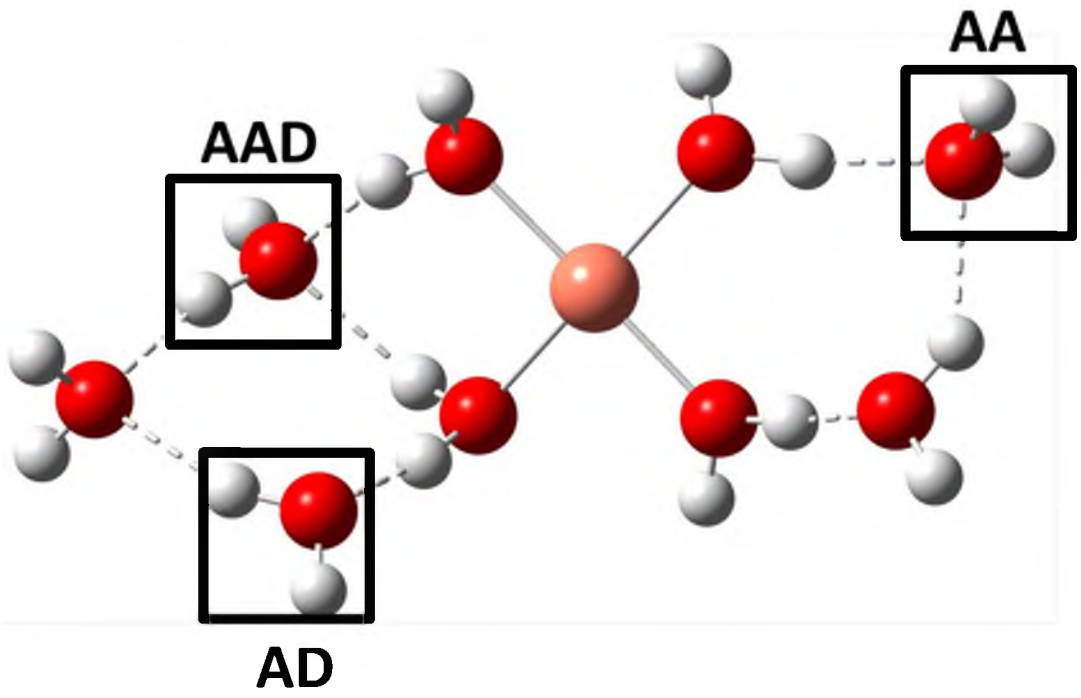

Figure 3.2. Hydrogen bonding motifs exemplified by the (4,3.5,1.5)_2AD,AAD_2AA complex: AA = double acceptor; AAD = double acceptor donating a hydrogen bond; AD = acceptor and donor. Note that the AA water to the right binds both a first and second shell ligand leading to its 0.5 designation. Center atom = copper; red (larger atoms) = oxygen; white (smaller atoms) = hydrogen.

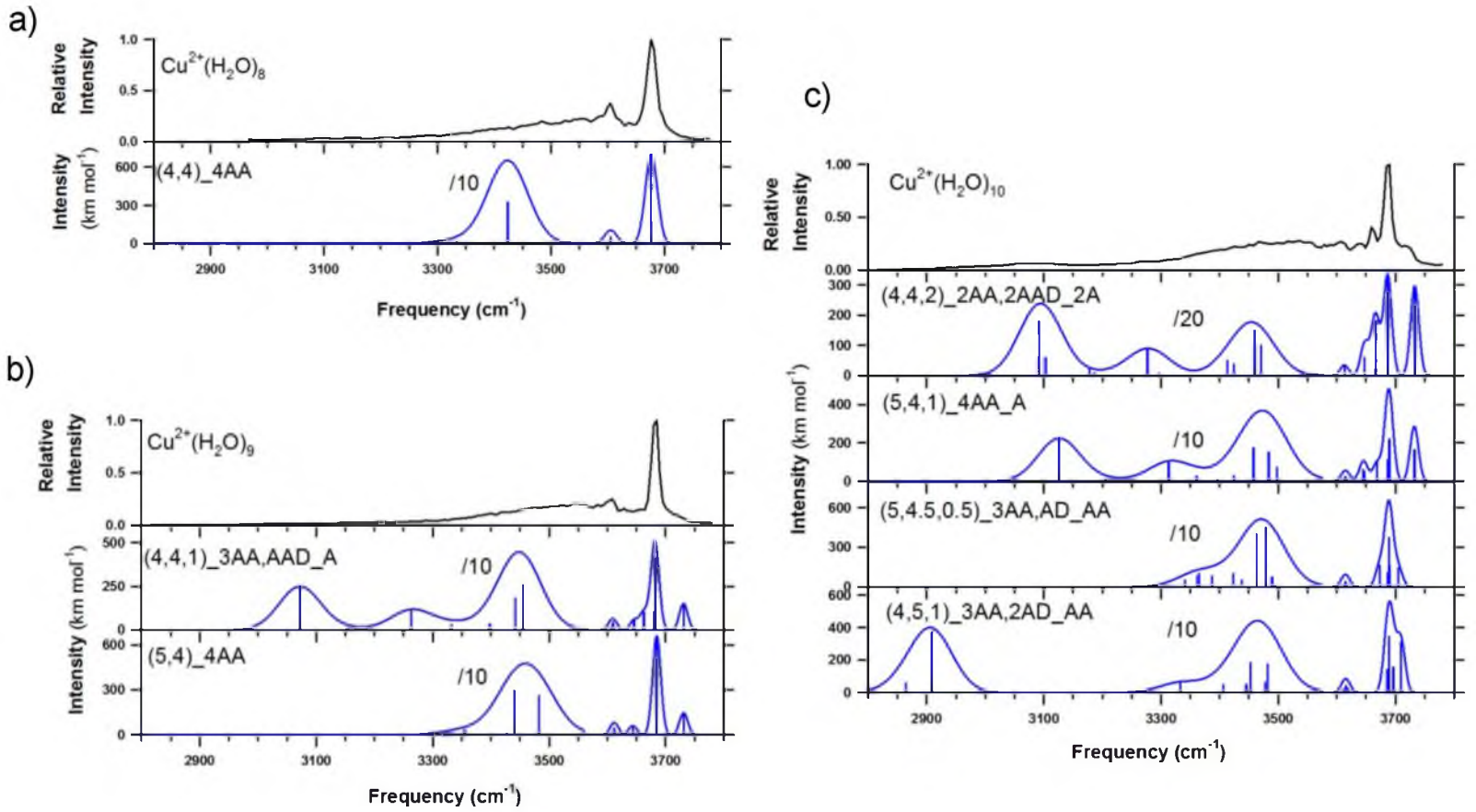

Figure 3.3. IRPD spectra at 215 K of O'Brien et al.[18] compared to theoretical spectra in the present work for $Cu^{2+}(H_2O)_n$, where n = 8 (part a), 9 (part b), and 10 (part c). Theoretical frequencies in the free-OH (above ~3550 cm^{-1}) and bonding-OH (below ~3550 cm^{-1}) regions have been scaled by 0.959 and convoluted over Gaussian linewidths of 10 and 50 cm^{-1}, respectively, to produce the theoretical spectra. Intensities in the bonding-OH regions have been scaled down by the factors shown. The top theoretical panels in all parts show the lowest energy isomers predicted by all levels at 298 K.

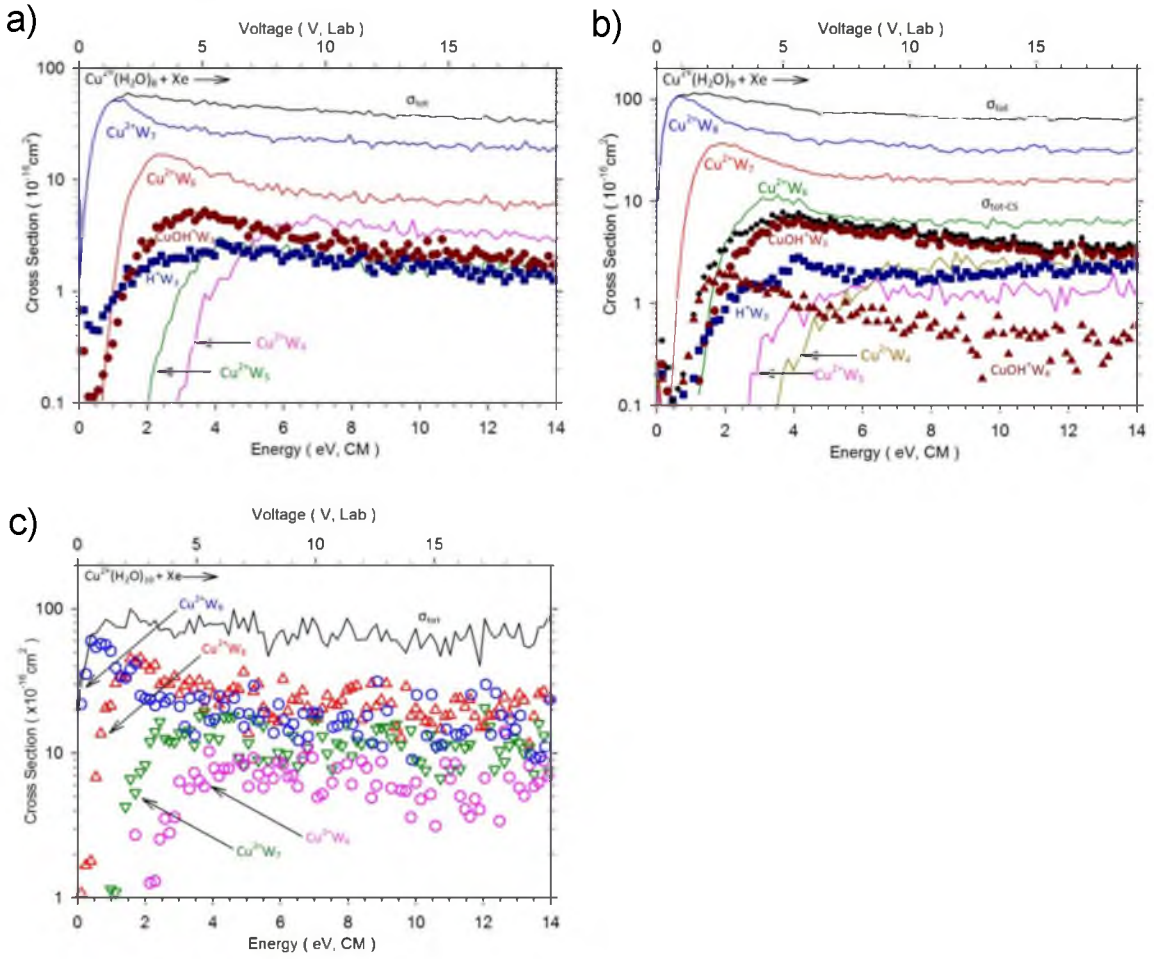

Figure 3.4. CID cross sections for the sequential water loss (lines) and charge separation processes (symbols) for $Cu^{2+}W_8$ (part a) and $Cu^{2+}W_9$ (part b), where W = H_2O, colliding with 0.2 mTorr of Xe as a function of energy in the laboratory (upper x-axis) and center-of-mass (lower x-axis) frames. In part b, black points show the total cross sections for the charge separation channels ($\sigma_{tot\text{-}CS}$). Part c shows the CID cross sections for sequential water loss (symbols) from $Cu^{2+}(H_2O)_{10}$. The uppermost black line in all parts shows the total cross section for all products (σ_{tot}).

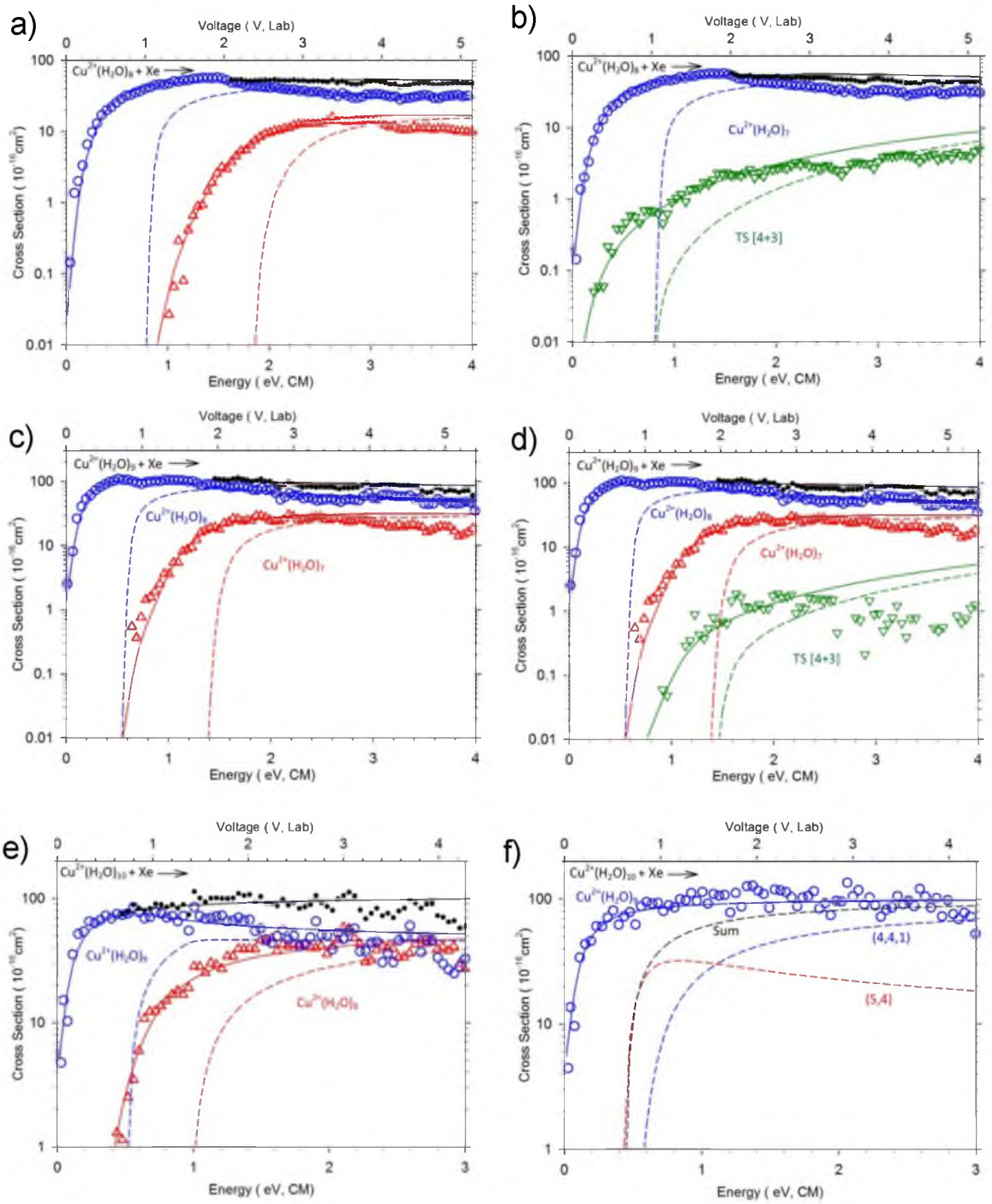

Figure 3.5: Zero pressure extrapolated cross sections for the CID of $Cu^{2+}(H_2O)_n$ with Xe for n = 8 – 10 (parts a – f). Solid lines show the best fits to the primary (circles), secondary (triangles), and total (dots) water loss cross sections and charge separation cross sections (inverted triangles) using eqs 3.3 and 3.4 convoluted over the kinetic and internal energy distributions of the neutral and ion. Dashed lines show the models in the absence of experimental kinetic energy broadening for reactants with an internal energy of 0 K. In part f, the relative energy between the (5,4) and (4,4,1) products is set to 0.05 eV. Optimized parameters for all fits are found in Table 3.2.

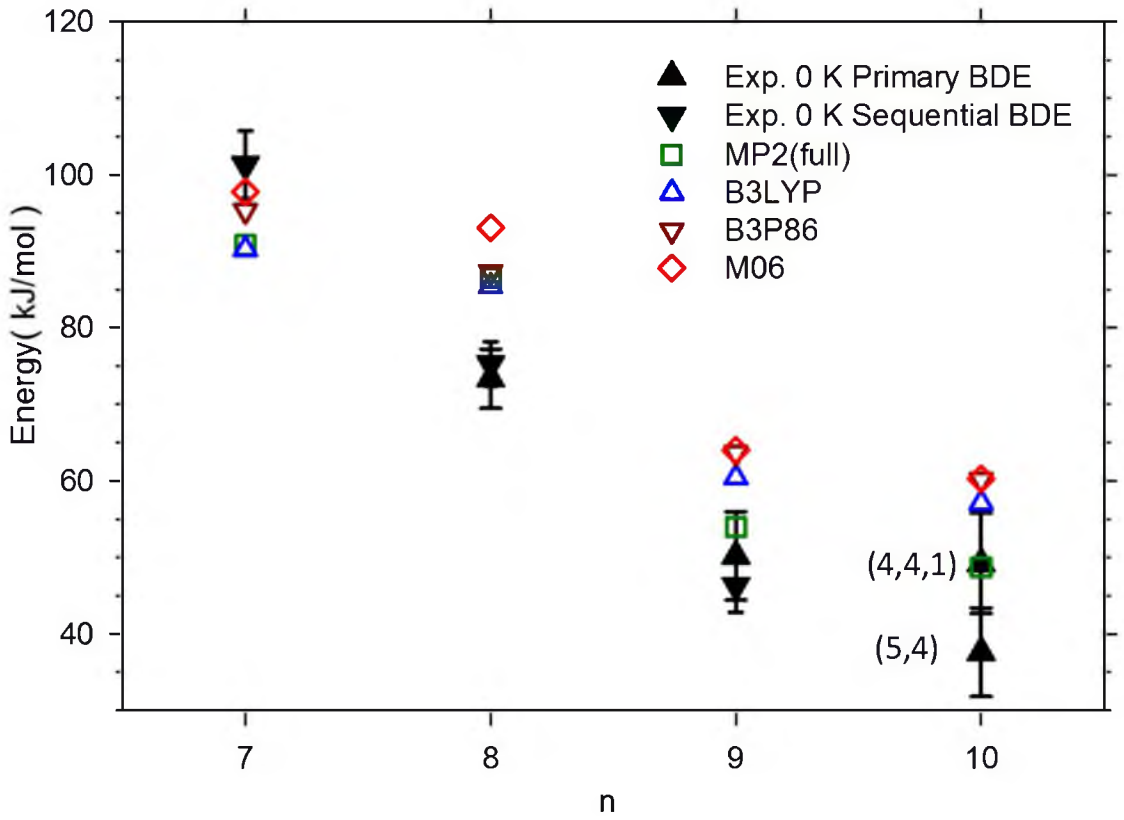

Figure 3.6: Comparison of experimental (solid symbols) and theoretical (open symbols) hydration enthalpies at 0 K for MP2(full), M06, B3LYP, and B3P86 SPEs with counterpoise corrections. Experimental value at n = 10 includes BDEs determined by modeling with the (4,4,1) product and (5,4) product at 0 K.

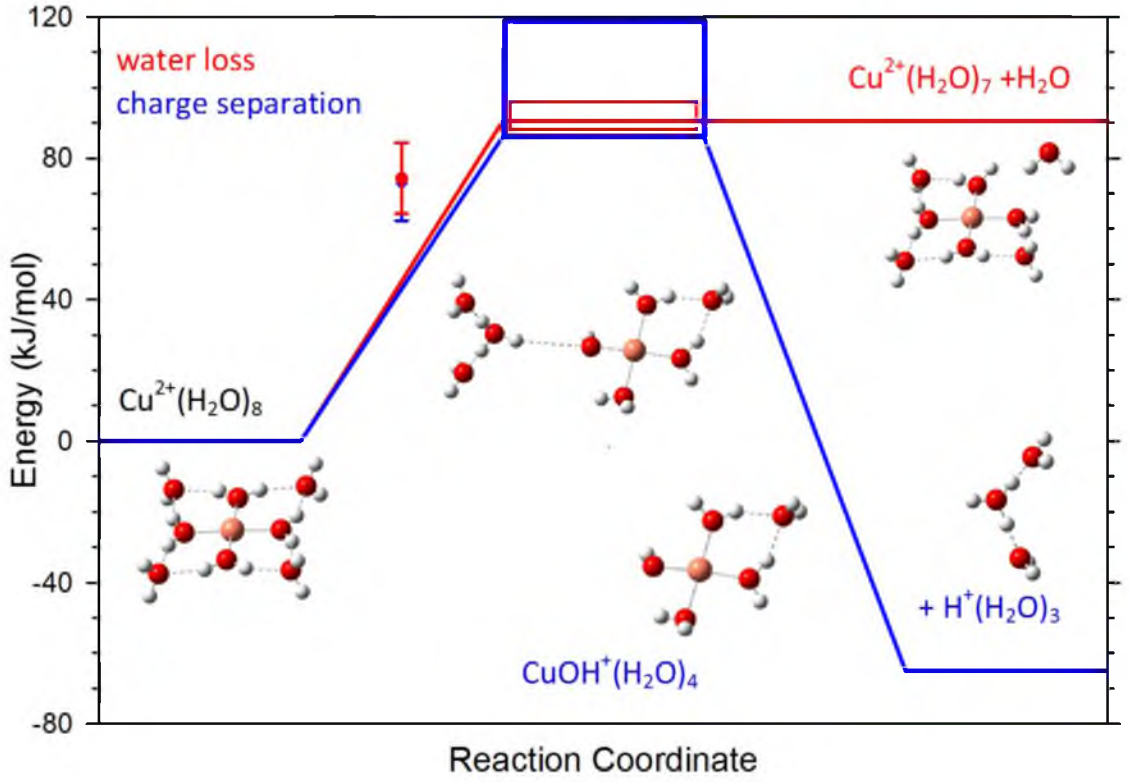

Figure 3.7. Theoretical potential energy surfaces for water loss (red lines) and charge separation (blue lines) from $Cu^{2+}(H_2O)_8$. Boxes indicate the range of theoretical values calculated. Red and blue circles with uncertainties represent experimental values obtained for each reaction channel.

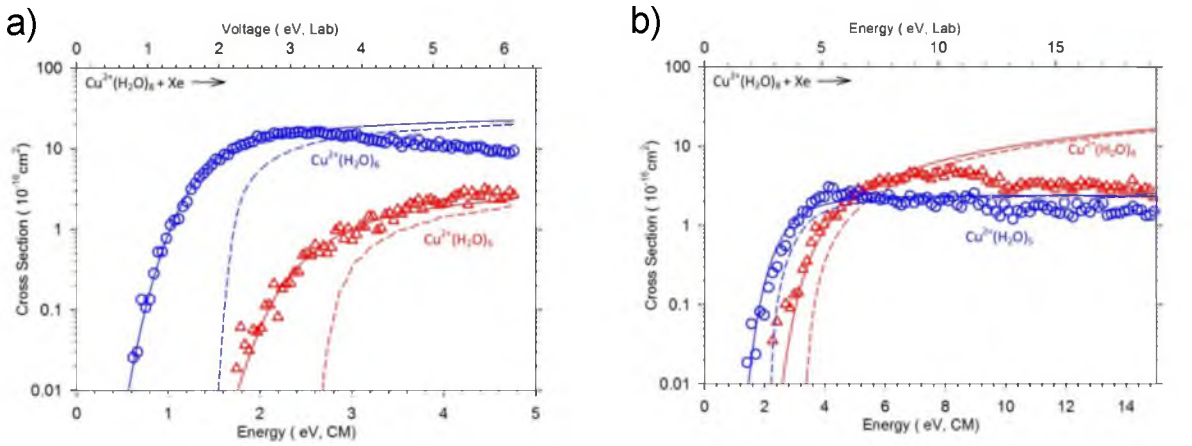

Figure 3.8: Cross sections for the CID of $Cu^{2+}(H_2O)_8$ with Xe to form a) $Cu^{2+}(H_2O)_6$ and $Cu^{2+}(H_2O)_5$ and b) $Cu^{2+}(H_2O)_5$ and $Cu^{2+}(H_2O)_4$. Solid lines show the best fits to the primary (circles) and secondary (triangles) cross sections using eqs 3.3 and 3.4 convoluted over the kinetic and internal energy distributions of the neutral and ion. Dashed lines show the models in the absence of experimental kinetic energy broadening for reactants with an internal energy of 0 K. Optimized parameters for these fits are found in Table 3.5.

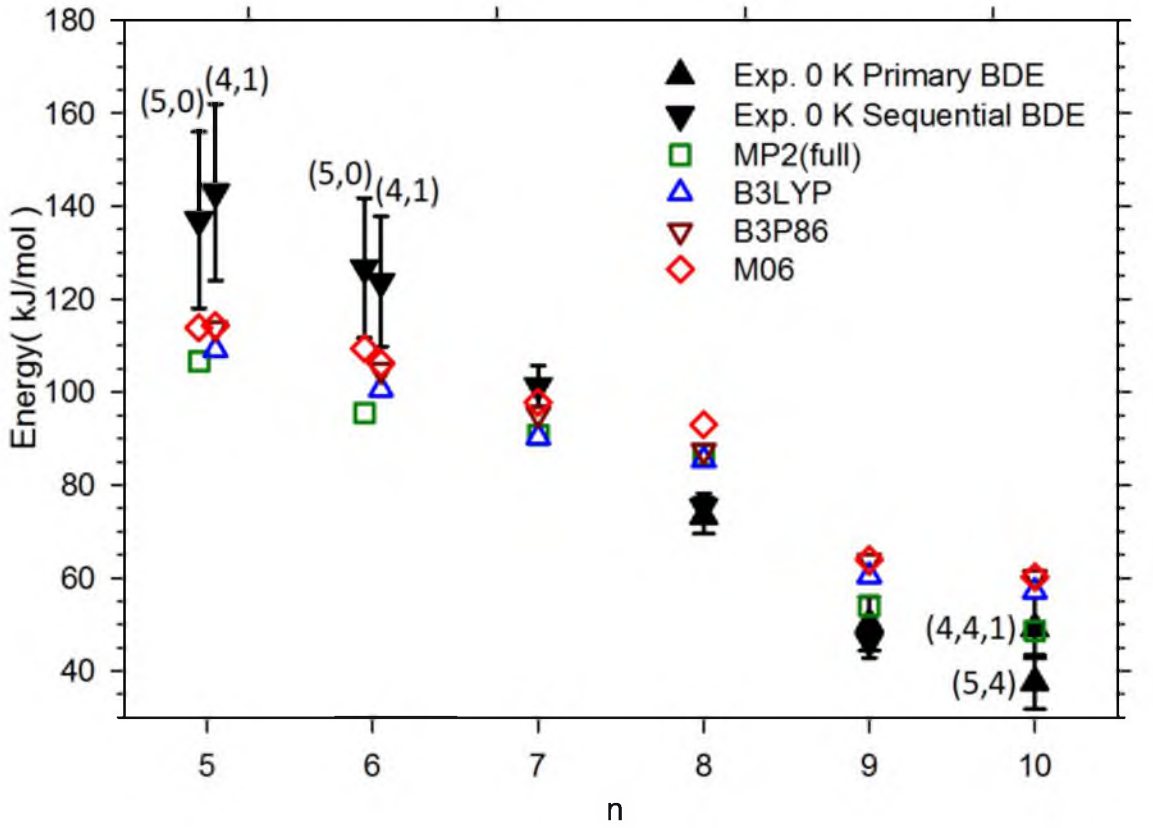

Figure 3.9: Comparison of experimental (solid symbols) and theoretical (open symbols) hydration enthalpies at 0 K for MP2(full), M06, B3LYP, and B3P86 SPEs with counterpoise corrections. Experimental value at n = 10 includes BDEs determined by modeling with the (4,4,1) product and (5,4) product at 0 K. Experimental value at n = 6 comes from modeling the tertiary sequential dissociation using both the (5,0), and (4,1) isomer at 0 K. Experimental value at n = 5 comes from modeling the quaternary sequential dissociation using both the (5,0), and (4,1) isomer at 0 K.

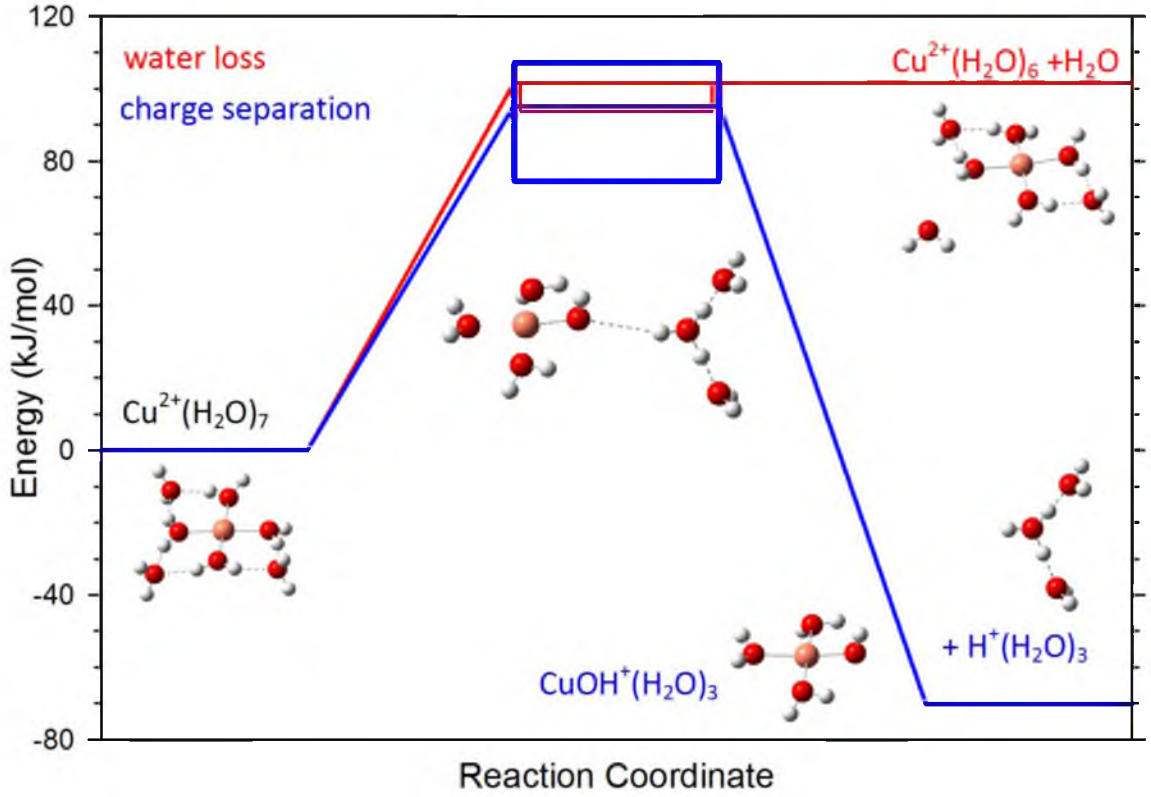

Figure 3.10: Theoretical potential energy surfaces for water loss (red lines) and charge separation (blue lines) from $Cu^{2+}(H_2O)_7$. Boxes indicate the range of theoretical values calculated.

3.6 References

[1]Thiele, D. J., Nucleic Acids Res. **20,** 1183 (1992)

[2]Zhou, P.; Thiele, D. J., Proc. Natl. Acad. Sci. **88,** 6112 (1991)

[3]Fernandes, J. C.; Henriques, F. S., Bot. Rev. **57,** 246 (1991)

[4]Mallick, N.; Mohn, F. H., Ecotoxicol. Environ. Saf. **55,** 64 (2003)

[5]Perales-Vela, H. V.; González-Moreno, S.; Montes-Horcasitas, C.; Cañizares-Villanueva, R. O., Chemosphere **67,** 2274 (2007)

[6]Zeng, L.; Miller, E. W.; Pralle, A.; Isacoff, E. Y.; Chang, C. J., J. Am. Chem. Soc. Comm. **128,** 10 (2006)

[7]Frank, P.; Benfatto, M.; Szilagyi, R. K.; D'Angelo, P.; Longa, S. D.; Hodgson, K. O., Inorg. Chem. **44,** 1922 (2005)

[8]Barnham, K. J.; Masters, C. L.; Bush, A. l., Nat. Rev. Drug Discovery **3,** 205 (2004)

[9]Waggoner, D. J.; Bartnikas, T. B.; Gitlin, J. D., Neurobiol. Dis. **6,** 221 (1999)

[10]Turnlund, J. R., Copper. In *Modern Nutrition in Health and Disease*, Shils, M. E.; Olson, J. A.; Shike, M.; Ross, A. C., Eds. Williams and Wilkins: Baltimore, MD, 1999.

[11]Uauy, R.; Olivares, M.; Gonzalez, M., Am. J. Clin. Nutr. **67,** 952S (1998)

[12]Greenwood, N. N.; Earnshaw, A., Chemistry of the Elements. Pergamon Press Oxford: 1984.

[13]Bryantsev, V. S.; Diallo, M. S.; Goddard, W. A., J. Phys. Chem. A **113,** 1520 (2009)

[14]Magnera, T. F.; David, D. E.; Stulik, D.; Orth, R. G.; Jonkman, H. T.; Michl, J., J. Am. Chem. Soc. **111,** 5036 (1989)

[15]Shvartsburg, A. A.; Siu, K. W. M., J. Am. Chem. Soc. **123,** 10071 (2001)

[16]Moore, C. E., *Atomic Energy Levels, NSRDS-NBS 35*. Washington, D. C., 1971; Vol. III, p 1.

[17]Stone, J. A.; Vukomanovic, D., Int. J. Mass Spectrom. **185–187,** 227 (1999)

[18]O'Brien, J. T.; Williams, E. R., J. Phys. Chem. A **112,** 5893 (2008)

[19]Rios-Font, R.; Sodupe, M.; Rodriguez-Santiago, L.; Taylor, P. R., J. Phys. Chem. A **114,** 10857 (2010)

[20]Bérces, A.; Nukada, T.; Margl, P.; Ziegler, T., J. Phys. Chem. A **103,** 9693 (1999)

[21]Duncombe, B. J.; Duale, K.; Buchanan-Smith, A.; Stace, A. J., J. Phys. Chem. A **111,** 5158 (2007)

[22]Holland, P. M.; Castleman, A. W., J. Am. Chem. Soc. **102,** 6174 (1980)

[23]Dalleska, N. F.; Honma, K.; Sunderlin, L. S.; Armentrout, P. B., J. Am. Chem. Soc. **116,** 3519 (1994)

[24]Iino, T.; Ohashi, K.; Mune, Y.; Inokuchi, Y.; Judai, K.; Nishi, N.; Sekiya, H., Chem. Phys. Lett. **427,** 24 (2006)

[25]Marsh, B. M.; Zhou, J.; Garand, E., J. Phys. Chem. A **118,** 2063 (2014)

[26]Sweeney, A. F.; O'Brien, J. T.; Williams, E. R.; Armentrout, P. B., Int. J. Mass Spectrom. (2014)

[27]Sweeney, A. F.; Armentrout, P. B., J. Phys. Chem. A **118,** (2014)

[28]Blades, A. T.; Jayaweera, P.; Ikonomou, M. G.; Kebarle, P., Int. J. Mass Spectrom. Ion Processes **102,** 251 (1990)

[29]Blades, A. T.; Jayaweera, P.; Ikonomou, M. G.; Kebarle, P., J. Chem. Phys. **92,** 5900 (1990)

[30]Stace, A. J.; Walker, N. R.; Firth, S., J. Am. Chem. Soc. **119,** 10239 (1997)

[31]Walker, N. R.; Firth, S.; Stace, A. J., Chem. Phys. Lett. **292,** 125 (1998)

[32]Cotton, F. A.; Wilkinson, G., *Advanced Inorganic Chemistry*. Wiley: New York, 1988.

[33]Kim, T.; Tolmachev, A. V.; Harkewicz, R.; Prior, D. C.; Anderson, G.; Udseth, H. R.; Smith, R. D., Anal. Chem **72,** 2247 (2000)

[34]Moision, R. M.; Armentrout, P. B., J. Am. Soc. Mass Spectrom. **18,** 1124 (2007)

[35]Heaton, A. L.; Moision, R. M.; Armentrout, P. B., J. Phys. Chem. A **112,** 3319 (2008)

[36]Heaton, A. L.; Ye, S. J.; Armentrout, P. B., J. Phys. Chem. A **112,** 3328 (2008)

[37]Carl, D. R.; Moision, R. M.; Armentrout, P. B., J. Am. Soc. Mass Spectrom. **20,** 2312 (2009)

[38]Carl, D. R.; Moision, R. M.; Armentrout, P. B., Int. J. Mass Spectrom. **265,** 308 (2007)

[39]Cooper, T. E.; Armentrout, P. B., Chem. Phys. Lett. **486,** 1 (2010)

[40]Cooper, T. E.; Carl, D. R.; Armentrout, P. B., J. Phys. Chem. A **113,** 13727 (2009)

[41]Ervin, K. M.; Armentrout, P. B., J. Chem. Phys. **83,** 166 (1985)

[42]Muntean, F.; Armentrout, P. B., J. Chem. Phys. **115,** 1213 (2001)

[43]Teloy, E.; Gerlich, D., Chem. Phys. **4,** 417 (1974)

[44]Aristov, N.; Armentrout, P. B., J. Phys. Chem. **90,** 5135 (1986)

[45]Hales, D. A.; Armentrout, P. B., J. Cluster Science **1,** 127 (1990)

[46]Daly, N. R., Rev. Sci. Instrum. **31,** 264 (1960)

[47]Armentrout, P. B., J. Am. Soc. Mass Spectrom. **13,** 419 (2002)

[48]Beyer, T. S.; Swinehart, D. F., Commun. ACM **16,** 379 (1973)

[49]Stein, S. E.; Rabinovitch, B. S., J. Chem. Phys. **58,** 2438 (1973)

[50]Stein, S. E.; Rabinovich, B. S., Chem. Phys. Lett. **49,** 183 (1977)

[51]Gilbert, R. G.; Smith, S. C., *Theory of Unimolecular and Recombination Reactions*. Blackwell Scientific: London, 1990.

[52]Holbrook, K. A.; Pilling, M. J.; Robertson, S. H., *Unimolecular Reactions*. 2nd ed.; Wiley: New York, 1996.

[53]Truhlar, D. G.; Garrett, B. C.; Klippenstein, S. J., J. Phys. Chem. **100,** 12771 (1996)

[54]Rodgers, M. T.; Ervin, K. M.; Armentrout, P. B., J. Chem. Phys. **106,** 4499 (1997)

[55]Rodgers, M. T.; Armentrout, P. B., J. Chem. Phys. **109,** 1787 (1998)

[56]Armentrout, P. B., J. Chem. Phys. **126,** 1 (2007)

[57]Armentrout, P. B.; Simons, J., J. Am. Chem. Soc. **114,** 8627 (1992)

[58]Dalleska, N. F.; Honma, K.; Armentrout, P. B., J. Am. Chem. Soc. **115,** 12125 (1993)

[59]Becke, A. D., Phys. Rev. A **38,** 3098 (1988)

[60]Lee, C.; Yang, W.; Parr, R. G., Phys. Rev. B **37,** 785 (1988)

[61]Perdew, J. P., Phys. Rev. B **33,** 8822 (1986)

[62]Zhao, Y.; Truhlar, D. G., Theor. Chem. Acc. **120,** 215 (2008)

[63]Möller, C.; Plesset, M. S., Phys. Rev. **46,** 618 (1934)

[64]Peschke, M.; Blades, A. T.; Kebarle, P., J. Am. Chem. Soc. **122,** 10440 (2000)

[65]Pavlov, M.; Siegbahn, P. E. M.; Sandstrom, M., J. Phys. Chem. A **102,** 219 (1998)

[66]Cooper, T. E.; Armentrout, P. B., J. Phys. Chem. A **113,** 13742 (2009)

[67]Bauschlicher, C. W.; Partridge, H., J. Chem. Phys. **103,** 1788 (1995)

[68]Boys, S. F.; Bernardi, R., Mol. Phys. **19,** 553 (1970)

[69]van Duijneveldt, F. B.; van Duijneveldt-van de Rijdt, J. G. C. M.; van Lenthe, J. H., Chem. Rev. **94,** 1873 (1994)

[70]Frisch, M. J.; Trucks, G. W.; Schlegel, H. B.; Scuseria, G. E.; Robb, M. A.; Cheeseman, J. R.; Scalmani, G.; Barone, V.; Mennucci, B.; Petersson, G. A.; Nakatsuji, H.; Caricato, M.; Li, X.; Hratchian, H. P.; Izmaylov, A. F.; Bloino, J.; Zheng, G.; Sonnenberg, J. L.; Hada, M.; Ehara, M.; Toyota, K.; Fukuda, R.; Hasegawa, J.; Ishida, M.; Nakajima, T.; Honda, Y.; Kitao, O.; Nakai, H.; Vreven, T.; Montgomery, J. A.; Peralta, J. E.; Ogliaro, F.; Bearpark, M.; Heyd, J. J.; Brothers, E.; Kudin, K. N.; Staroverov, V. N.; Kobayashi, R.; Normand, J.; Raghavachari, K.; Rendell, A.; Burant, J. C.; Millam, J. M.; Iyengar, S. S.; Tomasi, J.; Cossi, M.; Rega, N.; Millam, J. M.; Klene, M.; Knox, J. E.; Cross, J. B.; Bakken, V.; Adamo, C.; Jaramillo, J.; Gomperts, R.; Stratmann, R. E.; Yazyev, O.; Austin, A. J.; Cammi, R.; Pomelli, C.; Ochterski, J. W.; Martin, R. L.; Morokuma, K.; Zakrzewski, V. G.; Voth, G. A.; Salvador, P.; Dannenberg, J. J.; Dapprich, S.; Daniels, A. D.; Farkas, O.; Foresman, J. B.; Ortiz, J. V.; Cioslowski, J.; Fox, D. J. *Gaussian 09, Revision A.02*, Gaussian Inc.: Pittsburgh, PA, 2009

[71]Cooper, T. E.; O'Brien, J. T.; Williams, E. R.; Armentrout, P. B., J. Phys. Chem. A **114,** 12646 (2010)

[72]Jiang, J. C.; Wang, Y. S.; Chang, H. C.; Lin, S. H.; Lee, Y. T.; Niedner-Schatteburg, G.; Chang, H. C., J. Am. Chem. Soc. **122,** 1398 (2000)

[73]Shin, J. W.; Hammer, N. I.; Diken, E. G.; Johnson, M. A.; Walters, R. S.; Jaeger, T. D.; Duncan, M. A.; Christie, R. A.; Jordan, K. D., Science **304,** 1137 (2004)

[74]Bush, M. F.; Saykally, R. J.; Williams, E. R., ChemPhysChem **8,** 2245 (2007)

[75]Hofstetter, T. E.; Armentrout, P. B., J. Phys. Chem. A **117,** 1110 (2013)

[76]Carl, D. R.; Armentrout, P. B., ChemPhysChem **14,** 681 (2013)

[77]Carl, D. R.; Chatterjee, B. K.; Armentrout, P. B., J. Chem. Phys. **132,** 1 (2010)

[78]Peschke, M.; Blades, A. T.; Kebarle, P., J. Phys. Chem. A **102,** 9978 (1998)

[79]Wheeler, O. W.; Carl, D. R.; Hoffstetter, T. E.; Armentrout, P. B.,

[80]Irving, H. M. N. H.; Williams, R. J. P., J. Chem. Soc. 3192 (1953)

CHAPTER 4

STRUCTURAL ELUCIDATION OF HYDRATED $CUOH^+$ COMPLEXES USING IR ACTION SPECTROSCOPY AND THEORETICAL MODELING

Reprinted with permission of Elsevier from Andrew F. Sweeney, Jeremy T. O'Brien, Evan R. Williams, P. B. Armentrout, Structural elucidation of hydrated $CuOH^+$ complexes using IR action spectroscopy and theoretical modeling, *Int. J. Mass Spectrom*, (2014), http://dx.doi.org/10.1016/j ijms.2014.08.037

Model
15314 No. of Pages 11
ARTICLE IN PRESS

International Journal of Mass Spectrometry xxx (2014) xxx–xxx

Contents lists available at ScienceDirect

International Journal of Mass Spectrometry

journal homepage: www.elsevier.com/locate/ijms

Structural elucidation of hydrated $CuOH^+$ complexes using IR action spectroscopy and theoretical modeling

Andrew F. Sweeney [a], Jeremy T. O'Brien [b], Evan R. Williams [b,*], P.B. Armentrout [a,**]

[a] Department of Chemistry, University of Utah, 315 South 1400 East, Rm 2020, Salt Lake City, UT 84112, United States
[b] Department of Chemistry, University of California, Berkeley, CA 94720-1460, United States

ARTICLE INFO

Article history:
Received 17 July 2014
Received in revised form 21 August 2014
Accepted 25 August 2014
Available online xxx

Keywords:
IRPD
IR spectroscopy
Theory
Hydration
Clusters

ABSTRACT

Complexes of $CuOH^+(H_2O)_n$ where $n = 2–9$ are examined using infrared photodissociation spectroscopy (IRPD) with frequencies between ~2700 and 3900 cm^{-1}. Structural characterization is achieved through comparison between experimental and theoretical spectra. Geometry optimizations and frequency calculations are performed on a myriad of possible low-energy structures at the B3LYP/6-311+G(d,p) level. Subsequent single- point energy calculations are performed at the B3LYP, B3P86, M06, and MP2 (full) levels of theory using a 6-311+G(2d,2p) basis set to obtain relative free energies. The IRPD spectra of all complexes where $n \geq 3$ are consistent with structures having a coordination number (CN) of 4 although broad features in the $CuOH^+(H_2O)_5$ and $CuOH^+(H_2O)_6$ spectra accommodate structures having both CN = 4 and CN = 5. For $CuOH^+(H_2O)_7$, spectral bands in the free-OH region narrow, revealing fine structure that confirms the presence of both CN = 4 and CN = 5 isomers. Conformational assignments are made on the basis of asymmetric stretching frequencies of free-OH water molecules specific to each CN. Relative intensities of these bands are generally in good agreement with relative energies predicted by MP2(full) and not those of the other levels. MP2(full) and M06 single-point energies for the 4 and 5-coordinate isomers are typically within 5 kJ/mol of each other suggesting possible equilibration between the two if isomerization barriers are low.

1. Introduction

Copper is involved in a wealth of biological processes including the activation of many enzymes [1–6] as well as binding to the amino acids histidine, methionine, and cysteine in order to allow absorption through the amino acid transport system [7] . In small concentrations, it is essential for life, yet it is highly toxic at elevated levels [8]. This toxicity has led copper to be routinely monitored in drinking water supplies by the U.S. Environmental Protection Agency (EPA) [7]. Although Cu^{2+} is the predominant species in the aqueous environments typically found in nature, Cu^+ and $CuOH^+$ also exist in substantial concentrations [9].

The chemistry of hydrated copper ions has been previously investigated and includes studies spanning $Cu^{2+}(H_2O)_n$ [10–12], $Cu^+(H_2O)_n$ [13,14], and $CuOH^+(H_2O)_n$ [9,12,15]. Shvartsburg and Siu found that $Cu^{2+}(H_2O)_n$ dissociates via either loss of a water molecule or charge separation to produce $CuOH^+(H_2O)_m + H_3O^+(H_2O)_{n-m-2}$. The maximum size at which charge separation is competitive with simple ligand loss is called the critical size [11,16] and was found to be $Cu^{2+}(H_2O)_6$. Recent work in our lab showed that such observations depend on experimental sensitivity and source conditions, which prompted us to redefine the critical size as the maximum size at which charge separation is energetically more favorable than simple ligand loss [16]. The critical size of six for Cu^{2+} is higher than that for most other transition metals, which is thought to be a result of its exceptionally high 2nd ionization energy. The propensity for $Cu^{2+}(H_2O)_n$ to revert to a hydroxide complex reaffirms the necessity for a full understanding of all hydrated copper species. Bryantsev et al. used density functional theory in conjunction with the COSMO continuum solvent model to characterize the structures and relative energetics of $CuOH^+(H_2O)_n$ where $n = 3, 4, 5, 7$, and 17 [9]. They found that there was a strong preference for a coordination number (CN) of 4 until the second solvent shell was filled, at which point, CN = 5 was favored. Calculated differences between CN = 4 and 5 in most cases were <10 kJ/mol, indicating that the two forms could both be populated.

Recently, Marsh et al. used cryogenic ion spectroscopy to probe the OH stretch region of $CuOH^+(H_2O)_n$ complexes tagged with D_2 where $n = 1–3$ [15]. In that study, it was discovered that

* Corresponding author. Tel.: +1 510 642 7161; fax: +1 510 742 8369.
** Corresponding author.
E-mail addresses: erw@berkeley.edu (E.R. Williams), armentrout@chem.utah.edu (P.B. Armentrout).

http://dx.doi.org/10.1016/j.ijms.2014.08.037
1387-3806/

G Model
MASPEC 15314 No. of Pages 11
ARTICLE IN PRESS

$CuOH^+(H_2O)_n$ systems have a 4- coordinate inner shell that more resembles $Cu^{2+}(H_2O)_n$ [10] systems than the 2 -coordinate inner shells typical of $Cu^+(H_2O)_n$ systems [14]. Their failure to observe clusters larger than $CuOH^+(H_2O)_3$ suggested that the 4th water was weakly bound, whether axially to copper or in a second solvent shell through a hydrogen bonded network. Furthermore, the study acknowledges the possible presence of multiple isomers in complex sizes as small as $CuOH^+(H_2O)_2$ because of the broadness of two characteristic asymmetric OH stretching bands in that spectrum.

Experimental data for $CuOH^+(H_2O)_n$ with $n > 3$ have yet to be reported, which leaves the behavior of $CuOH^+$ in the presence of second and third hydration shells uninvestigated. Such systems provide solvent effects more akin to those found in biological systems. To address this issue, the present work uses infrared photodissociation (IRPD) spectroscopy to probe the structures of these larger systems up to $n = 9$. This technique has been successfully employed by Williams and co-workers to characterize the solvation of $Cu^{2+}(H_2O)_n$ where $n = 6–12$ as well as a variety of other metal complexes including those of Mg^{2+}, Ca^{2+}, Ba^{2+}, Mn^{2+}, Fe^{2+}, Co^{2+}, and Zn^{2+} [10,17–22]. As in the previous studies, structures of the complexes are identified by comparing the IRPD spectra with spectra calculated at the B3LYP/6-311+G(d,p) level. Relative energies determined at the B3LYP, B3P86, M06, and MP2 (full) levels of theory are used to consider which structures are likely to be populated.

2. Experimental section

2.1. Mass spectrometry

Experiments were performed using a home-built 2.7 T Fourier-transform ion cyclotron resonance (FT-ICR) mass spectrometer at UC Berkeley. Distributions of $CuOH^+(H_2O)_n$ were created by nanoelectrospray ionization (ESI) of 4 mM aqueous solutions of $CuSO_4$ (Fisher Scientific, Waltham, MA) using borosilicate capillaries pulled to an inner diameter of ~1 μm. These complexes were introduced into the mass spectrometer where they were trapped in a cylindrical ion cell encompassed by a copper jacket set to a temperature of either 450 ($n = 2$), 290 ($n = 3$), 210 ($n = 4$ and 5), or 130 ($n = 6–9$) K to maximize the abundance. The copper jacket was allowed to equilibrate for at least 8 h prior to the experiments. Ions were accumulated in the cell for 4–6 s, and during that time, dry N_2 gas (~10^{-6} Torr) was pulsed into the vacuum chamber to enhance trapping and thermalization of the ions using a piezoelectric valve. A mechanical shutter was subsequently closed to prevent further ion accumulation, and residual gases were pumped out for 6–10 s, resulting in a base pressure of ~10^{-8} Torr prior to ion isolation. The complex of interest was isolated using a stored waveform inverse Fourier transform (SWIFT) [23].

To obtain IR action spectra, the isolated complexes were irradiated using tunable IR light produced by an optical parametric oscillator/amplifier (OPO/OPA) system (LaserVision, Bellevue, WA) pumped by the fundamental of Nd:YAG laser (Continuum Surelight I-10, Santa Clara, CA) at 10 Hz repetition rate. Laser irradiation times were varied from 1 to 30 s to improve the dynamic range and signal-to-noise of the IR spectrum. Typically, shorter irradiation times (1–3 s) were used for frequencies in the free-OH stretch region (3600–3750 cm^{-1}) of the IR spectrum; otherwise, longer irradiation times (5–30 s) were used. All data were acquired using a MIDAS modular data system.

First order photodissociation rate constants (k_{IR}) are calculated from the precursor and fragmentation ion abundances and the irradiation time. Fragmentation resulting from blackbody infrared radiative dissociation (BIRD) is measured in the absence of laser irradiation and k_{BIRD} is subtracted from k_{IR} to obtain laser-induced photodissociation rate constants, k_{las}, which are plotted versus photon energy to obtain the IR action spectra of the isolated precursor ion. All IR spectra are corrected for frequency-dependent variations in laser power such that k_{las} has units of $W^{-1}\,s^{-1}$. This method has several advantages over plotting photodissociation yields in that intensities can be more directly compared to calculated IR absorption spectra and the intensities are readily corrected for changes in laser power and the irradiation time used [24].

2.2. Computational methods

Electronic structure calculations were performed on complexes with CN = 4, 5, and 6. For the smaller systems, $n = 2–4$, CN = 2 and 3 structures were also investigated. All structures were optimized at the B3LYP/6-311+G(d,p) level [25,26] using the Gaussian 09 suite of programs [27]. In order to avoid SCF convergence issues and to ensure that the lowest energy isomers were found, each structure was optimized four times with increasingly tighter SCF criteria and increasingly complex basis sets. Frequency calculations were performed after the final optimization and were compared to the experimental spectra by broadening each vibrational band using a Gaussian distribution. Gaussian line shapes of 15 or 10 cm^{-1} FWHM were used for the free-OH stretch region of $CuOH^+(H_2O)_{2–9}$, whereas line shapes of 50 cm^{-1} were routinely used for the hydrogen bonded-OH region. These values are similar to those used in previous reports on Cu^{2+} and Zn^{2+} hydration [10,21]. Furthermore, the intensities of vibrations in the hydrogen bonded-OH region are generally reduced as specified in each figure.

All vibrational frequencies are scaled by 0.956, which has been shown to provide good agreement with experimental IR spectra in the free OH region [10,21,28]. In a previous study of $Zn^{2+}(H_2O)_n$, where $n = 6–12$ [29], we have shown that vibrational frequencies obtained from a variety of levels of theory including B3LYP, BHandHLYP, and MP2(full) each using 6-311++G(d) and 6-311+G (2d,2p) basis sets were effectively identical. Relative energies of the different isomers were calculated using single point energies (SPE) at the B3LYP, B3P86 [30], MO6 [31], and MP2(full) [32] levels. These energetics include zero-point energy (ZPE) corrections to yield 0 K values as well as thermal corrections to the source temperature needed to achieve optimum signal intensity for each complex size. These corrections used the calculated frequencies scaled by 0.989, which was determined by Bauschlicher and Partridge to give accurate ZPE corrections at the B3LYP/6-311+G (3df,2p) level [33].

3. Results and discussion

3.1. IR action spectra

3.1.1. overview

Infrared action spectra from ~2700 to 3900 cm^{-1} for $CuOH^+(H_2O)_{2–9}$ are shown in Fig. 1. Common to all spectra is an intense feature in the range of ~3600–3700 cm^{-1}. Comparison to previously reported IR action spectra indicates that this feature corresponds to the symmetric and asymmetric stretching motion of O—H bonds not involved in hydrogen bonding, hereafter referred to as free- OH stretches. The relative intensity of these free-OH features gradually increase with complex size. At smaller complex sizes, the frequencies of these stretching motions are significantly red-shifted from their counterparts in isolated H_2O (3649 cm^{-1} and 3731 cm^{-1}, respectively) because of partial electron transfer to the copper cation, which weakens the O—H bond. As the complex size increases, electron transfer is distributed over more water molecules and the free-OH modes shift to the blue.

Please cite this article in press as: A.F. Sweeney, et al., Structural elucidation of hydrated $CuOH^+$ complexes using IR action spectroscopy and theoretical modeling, Int. J. Mass Spectrom. (2014), http://dx.doi.org/10.1016/j.ijms.2014.08.037

Model
15314 No. of Pages 11
ARTICLE IN PRESS

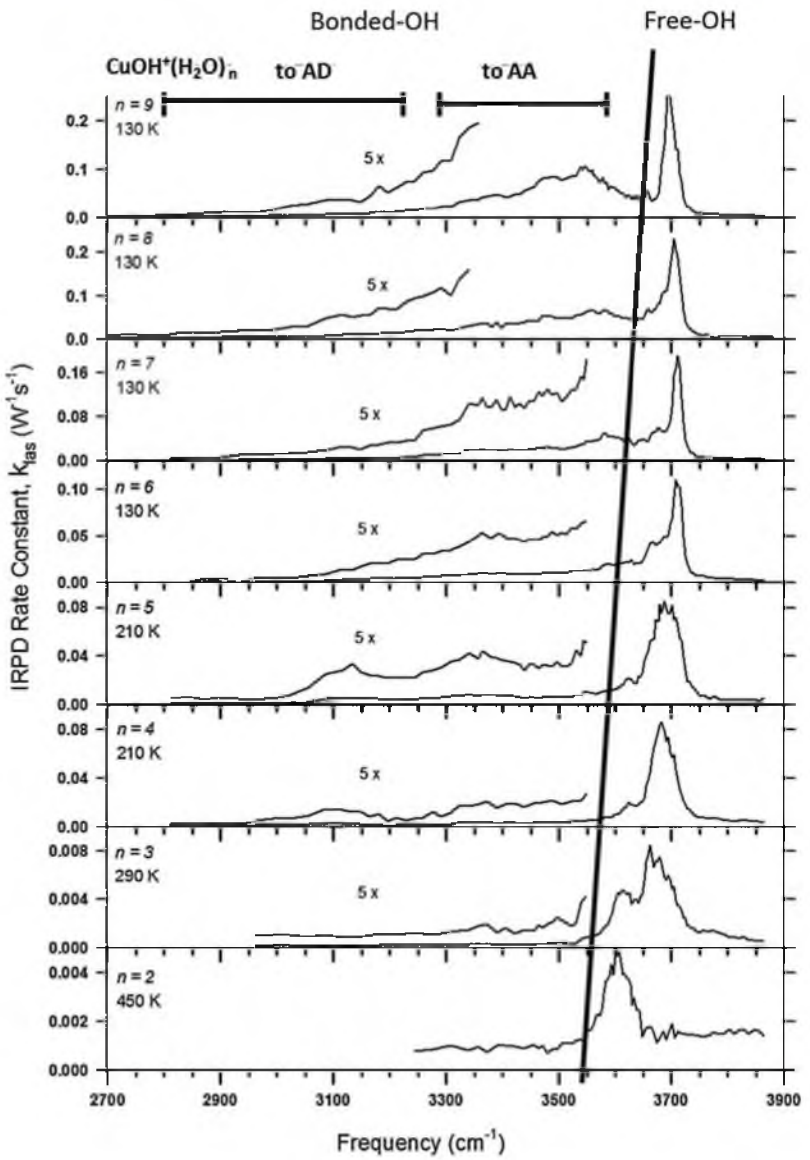

Fig. 1. IR action spectra of $CuOH^+(H_2O)_n$ where $n = 2$–9. Typical peak positions found in the bonded and free-OH regions and temperatures for each species are indicated. The IRPD rate constants are normalized according to the experimental laser intensity and irradiation time scale ($W^{-1}\,s^{-1}$).

Common to the spectra of $n \geq 4$ is a low intensity band to the red of the main free-OH peak, which maintains its intensity relative to the main peak throughout. In addition, these spectra all exhibit broad, low-intensity features between ~3000 and 3600 cm^{-1}. Comparison to previously reported IR action spectra [21] indicates that these features correspond to the stretching motion of hydrogen- bonded water molecules, hereafter referred to as bonded-OH stretches. Both $n = 4$ and 5 exhibit distinct peaks near 3100 and 3350 cm^{-1}, features absent in smaller complexes. For larger complexes, the relative intensity of the higher frequency band increases with complex size, while the lower frequency band maintains a similar relative intensity.

The smallest complex, $n = 2$, exhibits a single broad peak around 3600 cm^{-1} that can only correspond to the free-OH stretching motions of the copper-bound water molecules as well as the stretching motion of the OH ligand. This peak in the next largest complex, $n = 3$, is significantly blue-shifted from $n = 2$ and is broader. As the complexes grow in size, the maximum number of water molecules that can directly bind to copper is reached and water molecules begin to populate the second solvent shell. The binding of these second shell water molecules affects the spectrum in two ways. First, it quenches the free-OH stretching motions of the copper-bound water ligands involved. This interaction red-shifts those free-OH frequencies into the bonded-OH region which

Please cite this article in press as: A.F. Sweeney, et al., Structural elucidation of hydrated $CuOH^+$ complexes using IR action spectroscopy and theoretical modeling, Int. J. Mass Spectrom. (2014), http://dx.doi.org/10.1016/j.ijms.2014.08.037

G Model
MASPEC 15314 No. of Pages 11
ARTICLE IN PRESS

begins to take shape at $n=4$. Second, the free-OH stretching motions of the second-shell water molecules blue shift from their first-shell counterparts because of their greater distance and enhanced shielding from the copper center.

At $n=7$, the second solvent shell for a square–planar complex can be completely full. The resulting structural symmetry introduces degeneracy to the vibrational motions, thereby narrowing the bandwidth in the free-OH region. Indeed, this effect is reflected in the spectrum of $n=6$–9, analyzed more completely below.

We identify the possible origins of all of the aforementioned peaks and discuss their role in characterizing the experimental spectra in the following sections. At each complex size, we investigated the spectra of many low- energy isomers not shown in the figures, including all those listed in Table 1 as well those with relative energies too high to list there. None of these additional spectra showed better agreement with the experimental results. Included in these comparisons were 4, 5, and 6-coordinate species, although most calculations of 6- coordinate species collapsed into one of the 5-coordinate geometries.

3.1.2. Theoretical geometries of $CuOH^+(H_2O)_n$

The free energies calculated at 450 K ($n=2$), 290 K ($n=3$), 210 K ($n=4$ and 5), and 130 K ($n=6$–9) are given in Table 1 for the low energy isomers of $CuOH^+(H_2O)_n$ (values at 0 K are given in Table S1 of the Supporting Information). In most cases, the lowest energy structure is not the same across all four levels of theory. The density functional theories, B3LYP and B3P86, show similar relative energies and assign the same ground structure except for $n=3$ and 4. Compared to these DFT approaches, MP2(full) generally has different relative energies, but with the exception of $n=5$, 6, and 9, predicts the same ground structures. M06 falls somewhere in between, generally agreeing with MP2(full) ($n=$ 2–6 and 9), sometimes agreeing with B3LYP or B3P86 ($n=2$–4), and sometimes providing a unique assignment of the ground structure ($n=7$ and 8).

Included in this comparison are the structures found by Bryantsev et al. at $n=3$, 4, 5, and 7 at the B3LYP/6-311++G(d,p) level of theory with the LACV3P basis used for Cu. These structures were reoptimized at the same level of theory used here. For $n=3$ and 7, the lowest energy structure found by Bryantsev et al. was also the ground isomer located here at most levels of theory. For $n=4$ and 5, we located isomers that were lower in energy than the Bryantsev structures although nearly identical in structure such that their spectra are indistinguishable from the Bryantsev isomers. As a result, only one of the two spectra is shown although energies for both isomers are included in Table 1.

To ease the burden of describing unique structures, an (x, y, z) nomenclature will be used where x, y, and z equal the number of water molecules in the first, second, and third solvent shells, respectively, such that $CN=x+1$. To further distinguish each structure and provide a systematic naming scheme, the hydrogen bonding of second and third solvent shell water molecules are denoted outside of the parentheses using the A = acceptor and D = donor nomenclature established in Fig. 2. Water molecules in the same solvent shell are separated by commas whereas water molecules in different solvent shells are separated by underscores. Hydrogen bonding to the OH is indicated by a subscript. Instances where a single water molecule participates in hydrogen bonding with multiple solvent shells are indicated by a subscript detailing the shell involved when it differs from that for most other water ligands.

3.1.3. Comparison to theory

3.1.3.1. $n=7$. We start with the $n=7$ spectrum because this is one of the easier spectra to interpret definitively and it lays the foundations for appreciating the level of detail that is available in the lower frequency bonded-OH region of the spectra. Theoretical spectra for both 4 and 5-coordinate structures are shown underneath the experimental spectrum of $CuOH^+(H_2O)_7$ in Fig. 3. The main peak for this experimental spectrum is a sharp band at 3710 cm^{-1}, which is reproduced with high fidelity by the (3,4)_$2AD_{OH}$,2AA structure, the smallest complex that can contain a complete second shell of water ligands and the ground structure at all levels of theory, except M06 (Table 1). This peak corresponds to the in/out-of-phase ν_{asym} motions of the AD water molecules as well as those of the AA water molecules 10 cm^{-1} lower in frequency. This theoretical spectrum also reproduces the relative intensity and position of another small feature in the experimental spectrum located at 3650 cm^{-1}, which corresponds to the OH stretch. In the free OH region of the experimental spectrum, this leaves a small feature red-shifted from the main peak by ~30 cm^{-1} that is not reproduced in the theoretical spectrum of the (3,4) complex. However, this feature is consistent with the 5-coordinate complex, (4,3) _AA_2D_{OH},AD_{OH},AD_2, which exhibits a strong peak at this frequency. (Here, the subscript 2 indicates that the donor/acceptor interaction is with a second shell water molecule rather than a first shell water molecule.) This peak comprises seven ν_{asym} motions including those of the AA_2D_{OH} water molecule, the AD_2 water molecule, the OH, and the only free water molecule in the first shell.

The magnitude of this band relative to that of the main feature suggests that this structure is a minor contributor to the experimental spectrum. Given that the bands of the two structures have similar predicted intensities, the experimental relative intensity ratio of ~3/1 is consistent with a relative free energy difference of 1.2 kJ/mol at 130 K. Because overlap of the bands has not been considered and intensities of IRPD experiments need not match those of the calculated single photon spectra, there is significant uncertainty in determining relative isomer populations from spectral intensities. Nevertheless, it is clear that this relative intensity matches the predictions of the relative energies of the two structures found by MP2 theory (which predicts a ratio of 7/1) and not that of the DFT results (B3LYP and B3P86), where the population of the (4,3) structure is negligible, nor that of M06, which predicts an inverted population ratio. The ability of MP2

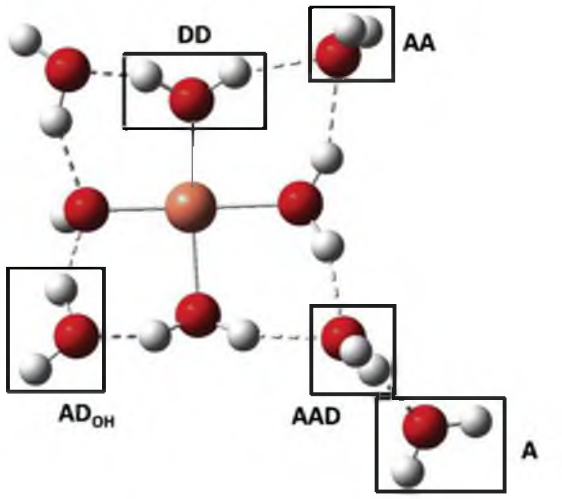

Fig. 2. Hydrogen bonding motifs exemplified by the (3,4,1)_$2AD_{OH}$,AAD,AA_A complex: A = single acceptor, AA = double acceptor, DD = double donor. Orange = copper (central atom), red = oxygen, white = hydrogen.

Please cite this article in press as: A.F. Sweeney, et al., Structural elucidation of hydrated $CuOH^+$ complexes using IR action spectroscopy and theoretical modeling, Int. J. Mass Spectrom. (2014), http://dx.doi.org/10.1016/j.ijms.2014.08.037

IJMS Model
15314 No. of Pages 11
ARTICLE IN PRESS

Table 1
Relative calculated free energies (kJ/mol) at the appropriate experimental temperature of $CuOH^+(H_2O)_n$.[a]

Complex	Structure	MP2(full)	M06	B3LYP	B3P86
$CuOH^+(H_2O)_2$	(2,0)	0.0	0.0	0.0	0.0
	(1,1)_A_t	57.1	28.6	21.9	24.2
	(1,1)_A_{OH}	[b]	45.1	42.3	46.1
	(1,1)_A_c	57.6	29.2	22.4	24.8
$CuOH^+(H_2O)_3$	(3,0)*	0.0	0.0	1.1	0.0
	(3,0)C_s	4.8	2.1	2.5	0.7
	(2,1)_AA	33.5	6.5	0.0	4.0
	(2,1)_A	43.0	19.0	7.2	11.1
$CuOH^+(H_2O)_4$	(3,1)_AA*	0.0 (3.1)	0.0 (3.1)	0.0 (3.2)	4.8 (1.7)
	(4,0)*	3.0	1.5	1.7	0.7
	(3,1)_AD_{OH}*	3.4	1.8	1.4	0.0
	(3,1)_AA_{OH}	13.4	9.7	3.7	10.7
$CuOH^+(H_2O)_5$	(4,1)_AAD_{OH}*	0.0 (2.7)	0.0 (0.0)	10.0 (12.7)	8.3 (11.0)
	(3,2)_AD_{OH},trans-AA*	2.1	2.4	0.0	0.0
	(3,2)_AD_{OH},cis-AA	2.2	4.0	1.2	0.8
	(3,2)_2AD_{OH}	11.0	14.1	9.9	7.9
	(3,2)_2AA	11.2	6.0	5.8	9.8
	(4,1)_AA	11.2	9.8	18.2	19.9
	(3,2)_AA,A	19.9	14.6	10.5	13.8
$CuOH^+(H_2O)_6$	(4,2)_2AAD_{OH}	0.0	0.0	12.0	9.2
	(4,2)_AAD_{OH},AA	2.9	5.5	10.7	12.1
	(4,2)_AAD_{OH},AD_{OH}	4.4	6.9	12.1	10.4
	(3,3)_2AD_{OH},AA	4.9	11.3	0.0	0.0
	(3,3)_2AA,AD_{OH}	6.7	11.0	0.4	3.4
	(4,2)_AAD_{OH},AA[c]	8.7	13.9	19.1	21.0
	(3,3)_AD_{OH},AA_{OH},AA	10.2	17.5	4.4	7.6
	(4,2) _AAD_{OH},AA_{OH}	12.2	11.9	16.3	17.4
	(3,3)_AD_{OH},AAD,AA	13.1	15.2	12.6	15.5
	(3,3)_2AD_{OH},AAD	18.8	23.0	18.7	19.0
$CuOH^+(H_2O)_7$	(3,4)_2AD_{OH},2AA*	0.0	2.5	0.0	0.0
	(4,3)_AA2D_{OH},AD_{OH},AD_2*	2.1	0.0	15.9	13.7
$CuOH^+(H_2O)_8$	(3,4,1)_AA_3D_{OH},AD_{OH},AAD_3,AA_AD	0.0	1.5	0.0	0.0
	(4,4)_AAD_{OH},AD_{OH},AAD,AD	2.0	4.0	14.9	14.8
	(4,4)_AA_2D_{OH},AAD_{OH},AD_2,AD	2.9	4.0	12.3	10.7
	(4,4)_AA_2D_{OH},AAD_{OH},AD_{ax},AD_2	3.2	4.4	13.4	11.8
	(4,4)_2AAD_{OH},2AD_{ax}	4.2	5.3	13.4	12.0
	(5,3)_2AAD_{OH},AA_{OH}	4.4	3.7	20.3	20.7
	(5,3)_2AAD_{OH},AD	5.3	1.9	26.7	25.6
	(4,4)_2AAD_{OH},2AAD	6.3	4.8	24.1	23.9
	(4,4)_2AAD_{OH},AA_{OH}D,AD	8.1	0.0	22.5	21.2
	(4,4)_2AAD_{OH},AA,AD	8.4	5.9	22.8	22.6
	(4,4)_AAD_{OH},AD_{OH},AD,A	9.1	16.4	17.8	19.3
	(4,4)_2AAD_{OH},AD_{OH},AA_{OH}	9.3	4.7	21.0	20.9
	(4,4)_2AAD_{OH},AA_{OH},AD	9.3	4.7	21.0	20.9
	(4,4)_2AADOH,2AD	11.7	9.0	28.7	29.6
	(3,4,1)_2AD_{OH},AAD_3,AA_A	12.5	15.6	5.7	7.5
	(3,4,1)_2AA,AD_3D_{OH},AD_{OH}_A	26.5	29.6	18.5	21.5
$CuOH^+(H_2O)_9$	(3,4,2)_2AAD_3,2AA_3D_{OH}_AA_3D,ADD_3	0.0	0.0	7.7	2.1
	(3,4,2)_2AA_3D_{OH},2AAD_3_2AD	16.6	21.1	7.4	4.4
	(4,4,1)_2AAD_{OH},AAD_3,AAD_A	17.2	34.3	17.9	13.5
	(4,5)_AA_2D_{OH},AD_{OH},AAD,AD_2,AA	17.3	23.5	20.2	18.1
	(4,4,1)_AA_3D_{OH},AD_{OH},AAD_3,AA_AD	20.1	27.8	19.0	16.9
	(3,4,2)_2AD_{OH},2AAD_3_cis-2A	21.9	27.9	0.0	0.0
	(3,4,2)_2AAD_3,AA_3D_{OH},AD_{OH}_AAD,A	25.6	30.4	10.5	8.4
	(3,4,2)_2AAD_{OH},2AAD_3_trans-2A	39.9	46.1	18.3	18.2

[a] Single point energies calculated at the level shown using a 6-311+G(2d,2p) basis set for geometries, zero point energy corrections, and thermal corrections (scaled by 0.989) calculated at the B3LYP/6-311+G(d,p) level of theory. * indicate structures also located by Bryantsev et al. [9]. In some cases, the ground structures identified by Bryantsev et al. were nearly identical to those identified in this study (and hence had identical vibrational spectra) but varied in energy. In those cases, the energy determined here of the ground structure found by Bryantsev et al. is in parentheses.
[b] MP2(full) results for (1,1)_A_{OH} were anomalous for reasons that remain unclear despite repeated computational approaches.
[c] Compared to the lower energy (4,2)_AAD_{OH},AA structure, in this structure, the OH ligand is approximately in the plane of the molecule as opposed to perpendicular to it.

theory to provide better predictions of the relative energies of metal water complexes has also been observed previously in our study of $Zn^{2+}(H_2O)_n$ complexes [21].

In the bonded-OH region, photodissociation is observed down to about 2900 cm^{-1}. A broad, bimodal feature extending from 3250 to 3500 cm^{-1} is reasonably reproduced by the (3,4) structure and corresponds to the in/out-of-phase stretches of waters H-bonded to the OH at the low frequency side and the in/out-of-phase stretches of waters H-bonded to the AA water molecules at the high frequency side. A much less intense peak around 3000 cm^{-1} in

Please cite this article in press as: A.F. Sweeney, et al., Structural elucidation of hydrated $CuOH^+$ complexes using IR action spectroscopy and theoretical modeling, Int. J. Mass Spectrom. (2014), http://dx.doi.org/10.1016/j.ijms.2014.08.037

G Model
MASPEC 15314 No. of Pages 11
ARTICLE IN PRESS

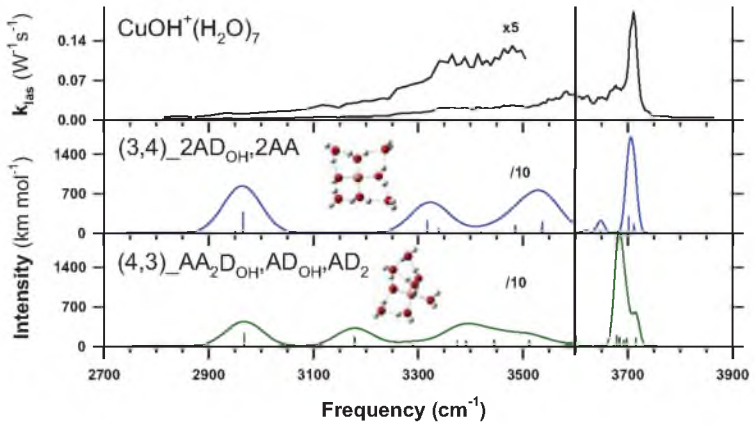

Fig. 3. Comparison of the experimental IRPD spectrum for $CuOH^+(H_2O)_7$ at 130 K with IR spectra for low-energy isomers predicted at the B3LYP/6-311 G(d,p) level. In the theoretical spectra, the bonded-OH region is broadened by 50 cm^{-1}, and the free-OH region is broadened by 10 cm^{-1}. Theoretical spectra in blue (top) and green (bottom) represent 4-coordinate and 5-coordinate spectra, respectively.

the theoretical spectrum signals the location of the in/out-of-phase stretches of waters H-bonded to the AD_{OH} water molecules, although it is not obvious whether this is reproduced in the experimental spectrum. Clearly, minor contributions of the (4,3) isomer are also consistent with the experimental spectrum in this region.

3.1.4. Comparison to theory. Larger complexes

3.1.4.1. n = 8. Four low-energy isomers and their corresponding spectra are shown with the experimental spectrum of $CuOH^+(H_2O)_8$ in Fig. 4. As for $n = 7$, the $n = 8$ complex retains a sharp peak located at ~3710 cm^{-1}, suggesting a similar structure. This is achieved by the (3,4,1) $\_AA_3D_{OH},AD_{OH},AAD_3,AA\_AD$ structure, the ground complex for MP2, B3LYP, and B3P86. Here, a third solvent shell water molecule has been added to the (3,4)_$2AD_{OH}$,2AA structure found for $n = 7$ where it interacts as both a donor and acceptor to two second shell ligands. The highest frequency vibrations for this structure correspond to ν_{asym} stretches of the third shell AD molecule as well as the second shell AD_{OH} molecules. These are nearly matched in frequency by ν_{asym} motions of the AA molecule and the two remaining AAD water molecules. The ν_{asym} motions for $n = 8$ are slightly less degenerate than those for $n = 7$ because the third shell water breaks the symmetry of the complex. This broadens the main peak in the experimental spectrum, as replicated in the theoretical spectrum. The small peak at 3650 cm^{-1} in the (3,4,1) $\_AA_3D_{OH},AD_{OH},AAD_3,AA\_AD$ spectrum is also consistent with the shoulder to the red of the main peak in the experimental spectrum. Likewise, features in the bonded-OH region for this structure are unremarkable but consistent with the observed spectrum, as well as with contributions from other possible isomers.

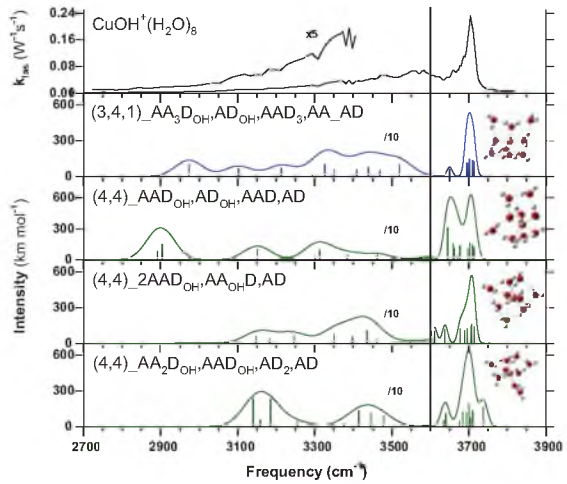

Fig. 4. Comparison of the experimental IRPD spectrum for $CuOH^+(H_2O)_8$ at 130 K with IR spectra for low-energy isomers predicted at the B3LYP/6-311+G(d,p) level. In the theoretical spectra, the bonded-OH region is broadened by 50 cm^{-1}, and the free-OH region is broadened by 10 cm^{-1}. Theoretical spectra in blue (top) and green (bottom three) represent 4-coordinate and 5-coordinate spectra, respectively.

The (4,4) $\_2AAD_{OH},AA_{OH}D,AD$ isomer is the M06 ground structure, although 8–23 kJ/mol above the (3,4,1) isomer at the other levels of theory. The spectrum of this isomer replicates the broadness of the main peak, however, the pair of low-intensity features at 3610 and 3640 cm^{-1} are not apparent in the experimental spectrum. The (4,4) $\_AAD_{OH},AD_{OH},AAD,AD$ and (4,4) $\_AA_2D_{OH},AAD_{OH},AD_2,AD$ isomers exhibit free-OH spectral features (an intense band at ~3650 cm^{-1} and a high frequency shoulder around 3740 cm^{-1}, respectively) that are not replicated in the experimental spectrum. Given relative energies of only 2.0 and 2.9 kJ/mol at the MP2 level, their calculated populations at 130 K are only 13 and 6%, respectively.

3.1.4.2. n = 9. The main feature at 3700 cm^{-1} in the $n = 9$ complex is similar to that for the $n = 7$ spectrum, although slightly red-shifted, as seen in Fig. 1. One can imagine adding two water molecules symmetrically to the (3,4)_$2AD_{OH}$,2AA structure. B3LYP and B3P86 theory suggest this occurs by adding waters in a third shell as single water acceptors, forming (3,4,2)_$2AD_{OH}$,$2AAD_3$_cis-2A, where the third shell waters are in adjacent positions away from the hydroxyl group. The spectrum of this isomer predicts four bands spaced by about 30 cm^{-1}, which is clearly inconsistent with experiment, Fig. 5. If these water molecules interact with two second shell ligands, the (3,4,2) $\_2AA_3D_{OH},2AAD_3\_2AD$ structure results, where the subscript 3 indicates bonds to a third shell water molecule. According to MP2 and M06, the energy of this complex is

Please cite this article in press as: A.F. Sweeney, et al., Structural elucidation of hydrated $CuOH^+$ complexes using IR action spectroscopy and theoretical modeling, Int. J. Mass Spectrom. (2014), http://dx.doi.org/10.1016/j.ijms.2014.08.037

Model
15314 No. of Pages 11
ARTICLE IN PRESS
A.F. Sweeney et al. / International Journal of Mass Spectrometry xxx (2014) xxx–xxx 7

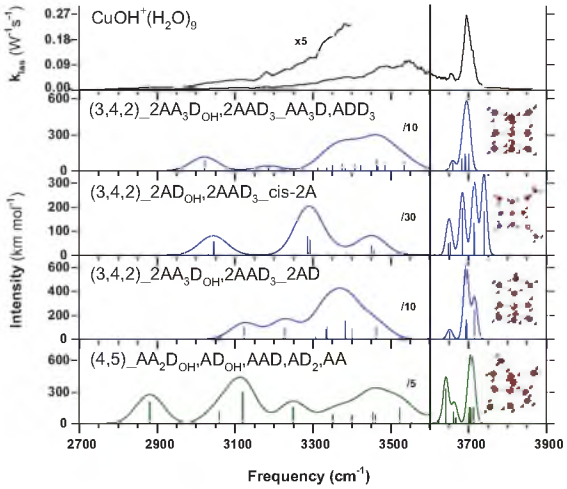

Fig. 5. Comparison of the experimental IRPD spectrum for $CuOH^+(H_2O)_9$ at 130 K with IR spectra for low-energy isomers predicted at the B3LYP/6-311+G(d,p) level. In the theoretical spectra, the bonded-OH region is broadened by 50 cm^{-1}, and the free-OH region is broadened by 10 cm^{-1}. Theoretical spectra in blue (top three) and green (bottom) represent 4-coordinate and 5-coordinate spectra, respectively.

greatly decreased by allowing the two third shell water molecules to H-bond to each other across the middle of the complex, giving the AA_3D,ADD_3 ground complex. The observed spectrum is quite consistent with this latter structure, which also predicts the small band observed at ~3610 cm^{-1} corresponding to the OH-stretching motion. The shoulder on the high frequency side of the main peak, as well as some intensity above 3730 cm^{-1}, could indicate contributions from other isomers similar to (3,4,2) $\_2AA_3D_{OH},2AAD_3\_2AD$, but no other isomers should be appreciably populated at 130 K on the basis of MP2 energies. Fig. 5 also includes the (4,5) complex with CN = 5, but the spectrum predicted for this isomer is clearly not a match for the experimental spectrum.

The bonded-OH region is much more intense for $n = 9$ than any other complex size because it has the most outer shell water ligands. The observed spectrum is consistent with that predicted for the (3,4,2) $\_2AA_3D_{OH},2AAD_3\_AA_3D,ADD3$ structure and not suggestive of the (3,4,2) $\_2AD_{OH},2AAD_3\_cis\text{-}2A$ spectrum. Again contributions from other species cannot be ruled out in this region.

3.1.5. Comparison to theory. Smaller complexes

3.1.5.1. n = 6. This is arguably the most peculiar complex size because of the unique features in the experimental spectrum, which again exhibits the sharp main peak near 3710 cm^{-1} but with a broad shoulder to the red (Fig. 6). Spectra from four low-energy isomers predicted by theory are also shown for $CuOH^+(H_2O)_6$. The location of the main peak is consistent with ν_{asym} of AD water molecules found in all the low-energy structures. Likewise, the broad shoulder to the red matches the range of frequencies for the ν_{asym} AA and ν_{asym} AD modes in these structures. Clearly, there is no one theoretical spectra that reproduces the experimental spectrum well, perhaps suggesting a combination of low-energy isomers. Certainly, the narrow high frequency part of this feature seems most consistent with the (3,3) $\_2AA,AD_{OH}$ structure, which would match the free OH region well if the intensity of the band at 3650 cm^{-1} were lowered. The broad shoulder is consistent with contributions from any of the low-energy structures. The intensity of the observed band at 3710 cm^{-1} can therefore be attributed either to particularly good overlap of these various spectra at this frequency or the real frequencies of some of the other structures are slightly different such that they yield more intensity at this frequency. As MP2 calculations predict that all of these structures are low-lying (within 7 kJ/mol of the ground structure), it is feasible that multiple isomers are formed for this complex.

In the bonded-OH region, intensity near 3600 cm^{-1} is consistent with ν_{sym} of the AA water molecules found in most of the low-energy structures. The broad band at 3200–3550 cm^{-1} agrees best with that predicted for the (3,3) structures, although the (4,2) isomers are also roughly consistent with the observed intensities, especially when shifts associated with the anharmonic

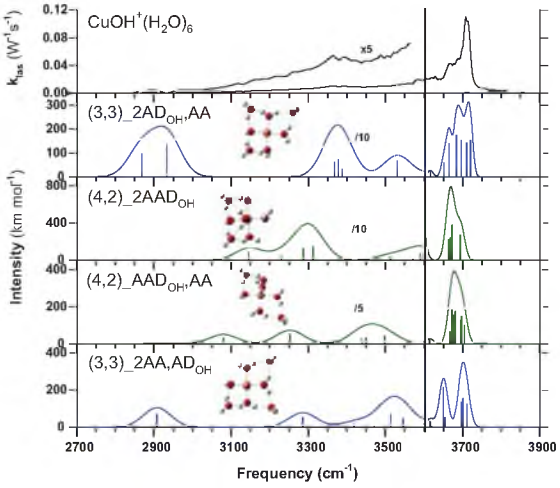

Fig. 6. Comparison of the experimental IRPD spectrum for $CuOH^+(H_2O)_6$ at 130 K with IR spectra for low-energy isomers predicted at the B3LYP/6-311+G(d,p) level. In the theoretical spectra, the bonded-OH region is broadened by 50 cm^{-1}, and the free-OH region is broadened by 15 cm^{-1}. Theoretical spectra in blue (top and bottom) and green (middle two) represent 4-coordinate and 5-coordinate spectra, respectively.

Please cite this article in press as: A.F. Sweeney, et al., Structural elucidation of hydrated $CuOH^+$ complexes using IR action spectroscopy and theoretical modeling, Int. J. Mass Spectrom. (2014), http://dx.doi.org/10.1016/j.ijms.2014.08.037

G Model
MASPEC 15314 No. of Pages 11
ARTICLE IN PRESS

nature of such hydrogen bonds are considered. The lack of intensity near 2900 cm^{-1} belies the assignment of appreciable amounts of the (3,3) isomers. Such a conclusion is not definitive, however, because the laser power and photon energies in this region are low, such that experimental intensities are often lower than predicted.

3.1.5.2. n = 5. Spectra for three low energy isomers of $CuOH^+(H_2O)_5$ and the experimental spectrum are shown in Fig. 7. In contrast to the larger complexes, $CuOH^+(H_2O)_5$ shows a much broader band centered at ~3680 cm^{-1} in the free-OH region. The location of this band is reproduced well by the predicted spectrum of the (4,1)_AAD_{OH} structure, the MP2 and M06 ground structure. The predicted spectrum of the (3,2)_AD_{OH},cis-AA structure also has a similar width, whereas the (3,2)_AD_{OH}, trans-AA structure, the B3LYP and B3P86 ground structure, has a distinctive shape inconsistent with being the dominant isomer present experimentally. A small peak observed at 3620 cm^{-1} is not particularly well reproduced by the (4,1)_AAD_{OH} structure, although this spectrum does show a band at 3600 cm^{-1} corresponding to ν_{sym} of the non-hydrogen bonded water ligand. This small peak agrees better with the ν_{asym} AA motion of the other two low energy structures.

In the bonded-OH region, there are three features including broad peaks centered near 3130 cm^{-1} and 3350 cm^{-1} and a plateau beginning near 3500 cm^{-1}. The band at 3130 cm^{-1} is not particularly well reproduced by any of the theoretical spectra, but lies closest to that for (4,1)_AAD_{OH}. The 3350 cm^{-1} band is consistent with most of the low-energy structures. The absence of intensity below 3000 cm^{-1} suggests that the (3,2)_AD_{OH},trans-AA and (3,2)_AD_{OH},cis-AA structures are not major contributors, although the caveats noted above for this region remain.

3.1.5.3. n = 4. The experimental spectrum for $CuOH^+(H_2O)_4$ is shown in Fig. 8 above those predicted for four low-energy isomers. The main band is centered around ~3675 cm^{-1} and is narrower than that for $n = 5$ but not as narrow as the larger complexes. A low intensity band to the red in the free-OH region is also evident. These features are reproduced reasonably well by the predicted spectrum for the (3,1)_AA structure, which is a 4-coordinate pseudo-square planar complex and the ground structure at all but the B3P86 level of theory. The vibrational frequencies that make up this main peak include the ν_{asym} of the water ligands as well as the

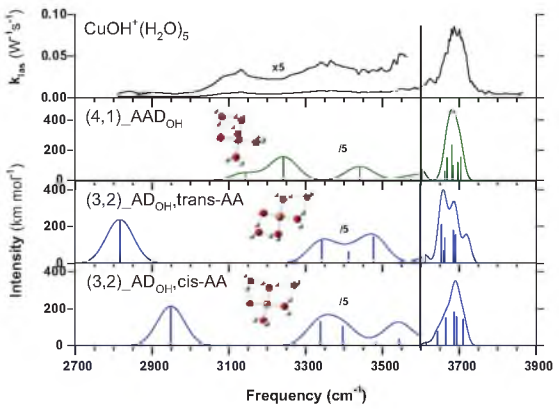

Fig. 7. Comparison of the experimental IRPD spectrum for $CuOH^+(H_2O)_5$ at 210 K with IR spectra for low-energy isomers predicted at the B3LYP/6-311+G(d,p) level. In the theoretical spectra, the bonded-OH region is broadened by 50 cm^{-1}, and the free-OH region is broadened by 15 cm^{-1}. Theoretical spectra in blue (bottom two) and green (top) represent 4-coordinate and 5-coordinate spectra, respectively.

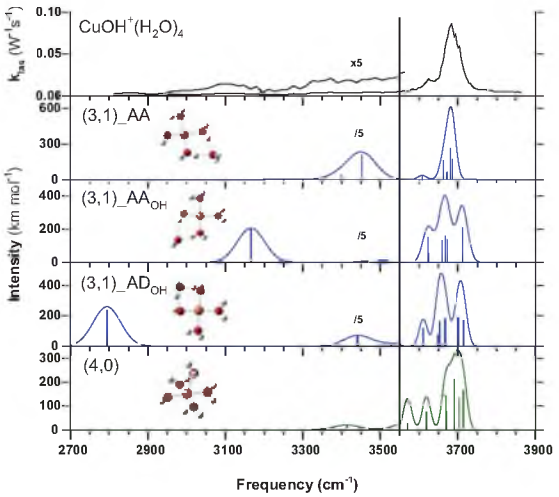

Fig. 8. Comparison of the experimental IRPD spectrum for $CuOH^+(H_2O)_4$ at 210 K with IR spectra for low-energy isomers predicted at the B3LYP/6-311+G(d,p) level. In the theoretical spectra, the bonded-OH region is broadened by 50 cm^{-1}, and the free-OH region is broadened by 15 cm^{-1}. Theoretical spectra in blue (top three) and green (bottom) represent 4-coordinate and 5-coordinate spectra, respectively.

OH stretch. The small band to the red of the main peak consists of ν_{sym} for the AA water, although its predicted frequency is red-shifted from experiment. The width of the free-OH bands in the other three spectra exclude these other isomers from being major contributors to the experimental spectrum. Although none are necessary to reproduce the experimental spectrum, the presence of small amounts of these other isomers cannot be excluded. At 210 K, the relative MP2 energies predict that the (3,1)_AA ground structure should account for >75% of an equilibrated population.

The experimental spectrum also shows two broad, low intensity bands in the bonded-OH region. The first is between 3300 and 3500 cm^{-1} which generally encompasses the ν_{sym} stretches of H-bonded waters and is consistent with the (3,1)_AA spectrum. This complex does not predict any intensity at lower frequencies, hence the small intensity at about 3100 cm^{-1} could indicate the presence of the (3,1)_AA_{OH} structure, where the band corresponds to the ν_{asym} modes of the AA_{OH} molecule. This frequency is significantly red-shifted from the usual location of stretching modes of AA molecules, which generally appear between 3300 and 3500 cm^{-1}. This results from its interaction with the OH ligand, which pulls electron density away from the water and weakens the free-OH stretching mode.

3.1.5.4. n = 3. Spectra for the four lowest energy isomers are shown under the experimental spectrum of $CuOH^+(H_2O)_3$ in Fig. 9. Included in this comparison is the infrared predissociation data of Marsh et al. for the loss of D_2 from $CuOH^+(H_2O)_3D_2$ [15]. Marsh et al. observed six well-resolved peaks in the free-OH region. We convoluted their observed frequencies over the same Gaussian linewidth used for the theoretical spectra to ensure a valid comparison with the present spectrum. Good agreement in these experimental spectra are observed, with two major bands, a broad peak from ~3650 to 3750 cm^{-1} and a smaller peak centered near 3610 cm^{-1}. Differences can be attributed to the very different temperatures in the two experiments and the effects of the D_2 tagging. The overall appearance of these peaks are matched nicely by the (3,0) spectrum, the ground structure at all levels of theory except B3LYP. The high frequency peak corresponds to the ν_{asym} of

Please cite this article in press as: A.F. Sweeney, et al., Structural elucidation of hydrated $CuOH^+$ complexes using IR action spectroscopy and theoretical modeling, Int. J. Mass Spectrom. (2014), http://dx.doi.org/10.1016/j.ijms.2014.08.037

Model
15314 No. of Pages 11
ARTICLE IN PRESS

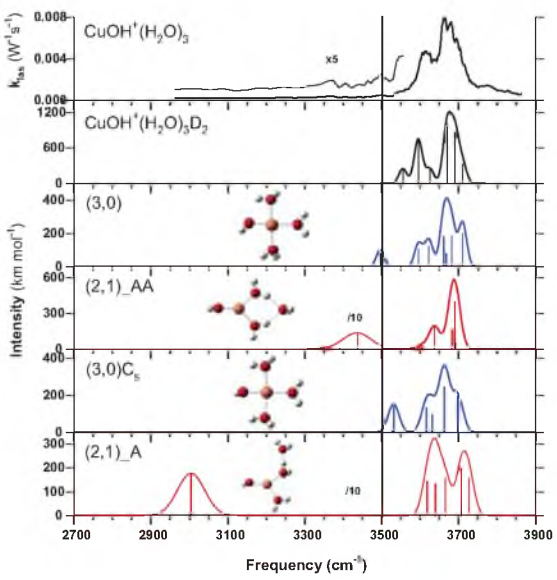

Fig. 9. Comparison of the experimental IRPD spectrum for $CuOH^+(H_2O)_3$ at 290 K and the experimentally determined frequencies and intensities of $CuOH^+(H_2O)_3D_2$ from Marsh et al. [15] convoluted over a Gaussian linewidth of 15 cm^{-1} with IR spectra for the lowest energy isomers predicted at the B3LYP/6-311+G(d,p) level. In the theoretical spectra, the bonded-OH region is broadened by 50 cm^{-1}, and the free-OH region is broadened by 15 cm^{-1}. Theoretical spectra in blue (third and fifth panels) and red (fourth and sixth panels) represent 4-coordinate and 3-coordinate spectra, respectively.

the water molecules as well as the OH stretching motion, whereas the low frequency peak corresponds to ν_{sym} of the same water molecules. Finally, the present spectrum contains a small peak at 3500 cm^{-1} that is also predicted in the (3,0) spectrum and is associated with ν_{sym} motions of the waters closest to the OH.

The H-bonded region is largely featureless but could be interpreted as containing a small peak around 3350 cm^{-1}. Interestingly, Marsh et al. also observed a broad, low intensity peak around 3390 cm^{-1} in their experimental data. Features in this region of the spectrum would indicate bonding to AA waters in the second shell as seen in the (2,1)_AA spectrum, the B3LYP ground structure. However, the relative intensity of this peak compared to the free-OH region suggests that any contribution from this isomer is likely very small, although the presence of this band in the colder temperature conditions (10 K) of Marsh et al. is intriguing, perhaps suggesting some kinetic trapping of the (2,1)_AA isomer or that its relative energy is low, more like the B3P86 result. In this comparison, it should also be realized that the D_2 tag affects the relative energies of the various isomers.

Finally, we note that there are two distinct (3,0) isomers found theoretically. As shown in Fig. 9, these differ primarily in orientation of the OH and one adjacent water molecule. In (3,0) C_s, the free OH bonds on both water molecules adjacent to the OH point up such that there is nearly a plane of symmetry through the Cu—OH bond. In the (3,0) ground structure, one of these bonds points down, which also alters the hydrogen bonding of the opposite water to the OH ligand, which then rotates. This change in the hydrogen bonding leads to the (3,0)C_s structure lying 1–5 kJ/mol above (3,0) according to theory, Table 1. The effect on the (3,0) C_s spectrum is a general broadening of the free-OH band along with a red-shift of one free- OH motion down to 3530 cm^{-1}. In both cases, these features agree with the experimental spectrum less precisely than the (3,0) ground isomer, perhaps suggesting that the (3,0)C_s isomer is not a major contributor.

3.1.5.5. n = 2. The main peak present in this spectrum is a broad band from ~3550 to 3650 cm^{-1}, Fig. 10. This peak is red-shifted from the main peaks of the other complex sizes by ~75 cm^{-1}, Fig. 1. The red-shift in this peak compared to $n = 3$ is a result of the copper ion pulling electron density from fewer ligands leading to higher partial electron transfer per ligand, thereby reducing the vibrational frequency of the free-OH stretching motions. To the blue of the main peak is potentially a small band near 3675 cm^{-1}. None of the predicted spectra reproduce this experimental result as they all exhibit multiple peaks.

When convoluted over a Gaussian linewidth of 15 cm^{-1}, the spectrum for $CuOH^+(H_2O)_2D_2$ of Marsh et al. [15] also exhibits broadness that does not match any of the predicted spectra. The best match comes from the (2,0) isomer, which agrees well with the high frequency portion of the Marsh spectrum but fails to predict the peak around 3560 cm^{-1}. However, calculations of Marsh et al. indicate that this peak is red-shifted by its interaction with D_2 and, in the absence of such an interaction, would have a frequency similar to that of the other water molecule, i.e., near 3610 cm^{-1}. The result would be a spectrum in good agreement with that of the (2,0) isomer, the ground isomer at all levels of theory. In contrast, the spectrum of the untagged ion is missing the higher frequency bands between 3650 and 3700 cm^{-1}. This is likely the result of the significantly higher temperature at which the spectrum of this ion was obtained, required in this case in order to provide efficient photodissociation.

To ensure that the missing intensity was not an artifact of our computational methods, we reoptimized the (2,0) structure at the MP2 (full) geometry. This resulted in a more T-shaped structure than the trigonal planar structure predicted by B3LYP, in

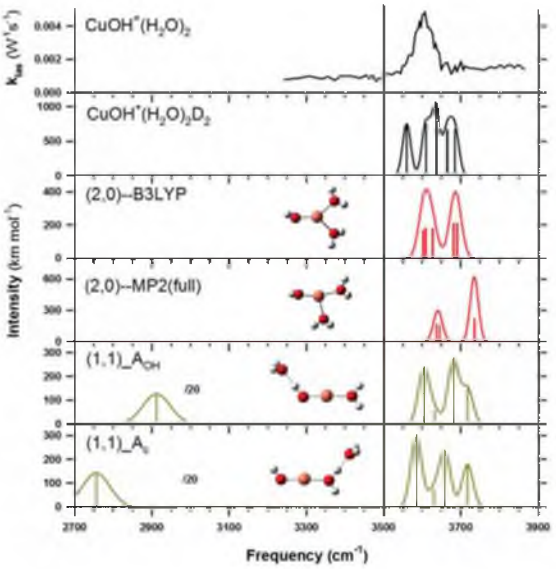

Fig. 10. Comparison of the experimental IRPD spectrum for $CuOH^+(H_2O)_2$ at 450 K and the experimentally determined frequencies and intensities of $CuOH^+(H_2O)_2D_2$ from Marsh et al. [15] convoluted over a Gaussian linewidth of 15 cm^{-1} with IR spectra for low-energy isomers calculated at the B3LYP/6-311+G(d,p) level. In the theoretical spectra, the bonded-OH region is broadened by 50 cm^{-1}, and the free-OH region is broadened by 15 cm^{-1}. Theoretical spectra in red (top two) and yellow (bottom two) represent 3-coordinate and 2-coordinate spectra, respectively.

Please cite this article in press as: A.F. Sweeney, et al., Structural elucidation of hydrated $CuOH^+$ complexes using IR action spectroscopy and theoretical modeling, Int. J. Mass Spectrom. (2014), http://dx.doi.org/10.1016/j.ijms.2014.08.037

G Model
MASPEC 15314 No. of Pages 11
ARTICLE IN PRESS

agreement with similar computational results of Marsh et al.. The resulting spectrum had peak intensity beyond 3750 cm^{-1} and bore little resemblance to either experimental spectra. This result is in accord with observations by Marsh et al. who found cam-B3LYP to agree best with experiment compared to CCSD and MP2 methods. In addition, their results suggested that the (2,0) structure might be even closer to a symmetric trigonal planar structure than predicted by the B3LYP methods.

3.2. Overview of results

For all complex sizes of $n \geq 3$, the experimental data generally suggest a dominant contribution of 4-coordinate pseudo-square planar structures although evidence for contributions from 5-coordinate pseudo-square pyramidal structures is apparent for $n = 5$–7. Distinctive peaks from the 4 and 5-coordinate species at $n = 7$ allow an estimate of the relative abundances of each. These relative abundances are accurately reproduced by the MP2(full) relative energies only. For $n = 5$ and 6, the experimental spectra show broadness resulting from overlapping spectra of multiple isomers, which suggests that the relative free energies between those isomers are small. In accord with this conclusion, MP2(full) and M06 levels of theory typically identify both 4 and 5-coordinate structures as lying close in energy. This is in contrast to the B3LYP and B3P86 relative energies for the same isomers which usually differ by >10 kJ/mol. Part of the reason for this different behavior has been elucidated by Rios-Font et al. in their computational study of $Cu^{2+}(H_2O)_n$ complexes [34]. There, they found that functionals with low amounts of exact exchange (such as B3LYP) overestimate the second ionization energy of Cu, such that the electron hole is too delocalized, especially in low coordinating environments, thereby overstabilizing these geometries.

3.3. Comparison to hydrated Cu^{2+} and Cu^{+}

Solvated Cu^{2+} systems show a preference for a 4-coordinate species [10], whereas studies of solvated Cu^{+} systems show a preference for a 2-coordinate system [14,35,36]. This distinction arises from the electronic character of $Cu^{2+}(^2D, 3d^9)$ versus $Cu^{+}(^1S, 3d^{10})$. For a d^9 complex, ligand field theory prefers a square planar geometry as this allows the d_{x2-y2} orbital, which points at the ligands, to be singly occupied. The out-of-plane d_{z2} orbital, which must be doubly occupied, is repulsive for addition of a fifth ligand. For the spherically symmetric $3d^{10}$ complex, ligation occurs by donation into the empty 4s orbital, which can then hybridize with an empty 4p to enhance the binding and provide the preference for 2-coordination. If more ligands are added, however, tetrahedral and octahedral geometries are possible and hydration of $Zn^{2+}(^1S, 3d^{10})$ shows a preference for 5- coordination [21].

In the present systems, $CuOH^+$ is clearly acting primarily as a d^9 complex, suggesting its electronic character is largely $Cu^{2+}OH^-$, where the OH^- is a two-electron donor like the water ligands. Examination of the molecular orbitals of many of the complexes here verifies that the singly occupied molecular orbital (SOMO) in the 4-coordinate complexes is the d_{x2-y2} on copper, as anticipated. This is demonstrated well by the SOMO of (3,4)_$2AD_{OH}$,2AA, as seen in Fig. 11. However, because of the electronic ambiguity of $Cu^{2+}OH^-$ versus $Cu^{+}OH$, the addition of a fifth ligand to the copper center is a low-lying configuration, and the calculated ground state for $CuOH^+(H_2O)_n$ where $n = 5$ and 6 according to MP2 and M06 theory. In these configurations, the SOMO is again largely d_{x2-y2}, although it appears that some d_{x2} character (where the Cu–OH bond lies along the x axis) is mixed in so that the SOMO now has a doughnut-shaped lobe interacting with three water ligands along with lobes pointing towards the OH and opposite water ligand.

This electronic ambiguity has additional consequences in the presence of second and third solvent shells. For example, MP2(full) predicts that 4-coordinate species are more stable for $n = 3$ and 4, that 5-coordinate species are more stable for $n = 5$ and 6, and that at $n = 7$, the 4-coordinate species is again the preferred geometry. Our experimental results are generally consistent with these predictions. The switch from 4- to 5-coordinate for $n = 5$ and 6 is potentially attributed to the more complicated hydrogen bonding networks that are permitted by the axial water ligand. For $n = 5$ and 6, water molecules in 4-coordinate square planar complexes can only participate in two hydrogen bonds each, whereas water molecules in 5-coordinate square pyramidal complexes can participate in three hydrogen bonds. As the system then moves to the more highly solvated $n = 7$–9 complexes, there is probably enhanced stability from a filled and symmetric second solvent shell. For $n = 8$ and 9, water molecules in the third solvent shell of 4-coordinate complexes are now able to form three hydrogen bonds and the hydrogen-bonding advantage of the 5-coordinate geometry is lost. Interestingly, the 6- coordinate species is never favored, suggesting that the more complicated hydrogen bonding afforded by one axial ligand does not continue to hold for a second axial ligand. Apparently, the energetic cost to the d^9 configuration of having two axial ligands cannot be justified as it adds no more hydrogen bonding opportunities than the single axial ligand. This is clear at $n = 5$ because having a second axial ligand requires removal of the hydrogen-bonded second shell water molecule, which eliminates the hydrogen bonding advantage. At $n = 6$, only one water molecule can participate in the more complex hydrogen bonding, which doesn't offset the energetic penalty of two axial ligands. At $n = 7$ and above, having any axial ligands is less favored than the filled and symmetric second solvent shell.

One can imagine that more extensive solvation than that examined here might eventually lead to more highly coordinated geometries. Indeed, the study of Bryantsev et al. examined this by using the COSMO continuum solvent model [9]. In general, their results show that more complete solvation actually destabilizes the more highly coordinated geometries for $n = 5$ and 7. For $CuOH^+(H_2O)_{17}$, the 5-coordinate geometry is the ground state (both in the gas-phase and solution) with the 4-coordinate geometry lying 7.1 kJ/mol higher in energy (not stable in the gas phase) and a

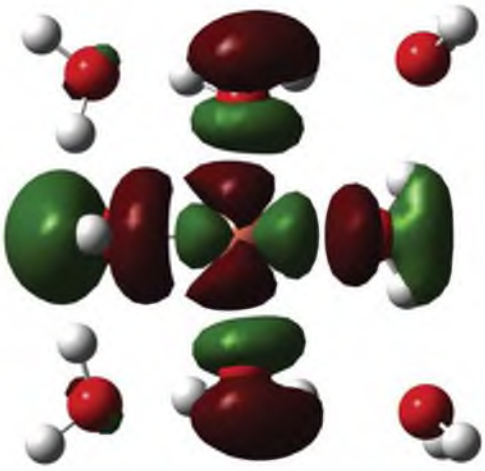

Fig. 11. Singly occupied molecular orbital (SOMO) of (3,4)_$2AD_{OH}$,2AA. The hydroxide ligand is left center.

Please cite this article in press as: A.F. Sweeney, et al., Structural elucidation of hydrated $CuOH^+$ complexes using IR action spectroscopy and theoretical modeling, Int. J. Mass Spectrom. (2014), http://dx.doi.org/10.1016/j.ijms.2014.08.037

Model
15314 No. of Pages 11
ARTICLE IN PRESS

6-coordinate structure lying 1.0 (gas-phase) or 9.3 (solution) kJ/mol above the ground structure. Interestingly, in the 5-coordinate geometry of $CuOH^+(H_2O)_{17}$, the water ligands form a shell surrounding the unoccupied axial site on copper, clearly indicating electron density at this position. Bryantsev et al. conclude by noting that difference in the various solution phase coordinations are sufficiently small "that they may dynamically coexist."

Although the bonding motifs between $CuOH^+$ and Cu^{2+} are similar in coordination number, there are major differences between the placements of the third solvent shell waters. Hydrated Cu^{2+} systems have the third shell waters attached as free rotors through a single hydrogen bond (A) to the second shell waters [10]. $CuOH^+$ systems, however, prefer more hydrogen bonding where the third shell waters are both accepting and donating hydrogen bonds. It is also notable that the ν_{asym} AAD motions are blue-shifted from the corresponding motions in the Cu^{2+} complexes by $\sim 20\,cm^{-1}$. Both of these differences arise because the OH group is more electron withdrawing than the surrounding waters, which weakens the copper–water bonds and allows for stronger vibrations of the water molecules.

Acknowledgements

The authors wish to thank Professor Veronica Bierbaum for many years of wonderful interactions and scientific discussions that have inspired generations of new scientists in the fields of ion structure, energetics and mass spectrometry. This work is supported by the National Science Foundation, Grant No. CHE-1359769 (PBA) and CHE- 1306720 (ERW). In addition, we thank the Center for High Performance Computing at the University of Utah for the generous allocation of computer time.

Appendix A. Supplementary data

Supplementary data associated with this article can be found, in the online version, at http://dx.doi.org/10.1016/j.ijms.2014.08.037.

References

[1] L. Zeng, E.W. Miller, A. Pralle, E.Y. Isacoff, C.J. Chang, J. Am. Chem. Soc. Commun. 128 (2006) 10.
[2] P. Frank, M. Benfatto, R.K. Szilagyi, P. D'Angelo, S.D. Longa, K.O. Hodgson, Inorg. Chem. 44 (2005) 1922.
[3] K.J. Barnham, C.L. Masters, A.L. Bush, Nat. Rev. Drug Discov. 3 (2004) 205.
[4] D.J. Waggoner, T.B. Bartnikas, J.D. Gitlin, Neurobiol. Dis. 6 (1999) 221.
[5] J.R. Turnlund, in: M.E. Shils, J.A. Olson, M. Shike, A.C. Ross (Eds.), Modern Nutrition in Health and Disease, Williams and Wilkins, Baltimore, MD, 1999.
[6] R. Uauy, M. Olivares, M. Gonzalez, Am. J. Clin. Nutr. 67 (1998) 952S.
[7] L. Gaetke, M. Chow, C. Kuang, Toxicology 189 (2003) 147.
[8] D.R. Winge, R.K. Mehra, Int. Rev. Exp. Pathol. 31 (1990) 47.
[9] V.S. Bryantsev, M.S. Diallo, W.A. Goddard III, J. Phys. Chem. A 113 (2009) 9559.
[10] J.T. O'Brien, E.R. Williams, Phys. Chem. A 112 (2008) 5893.
[11] A.A. Shvartsburg, K.W.M. Siu, J. Am. Chem. Soc. 123 (2001) 10071.
[12] J.A. Stone, D. Vukomanovic, Int. J. Mass Spectrom. 185–187 (1999) 227.
[13] N.F. Dalleska, K. Honma, L.S. Sunderlin, P.B. Armentrout, J. Am. Chem. Soc. 116 (1994) 3519.
[14] T. Iino, K. Ohashi, Y. Mune, Y. Inokuchi, K. Judai, N. Nishi, H. Sekiya, Chem. Phys. Lett. 427 (2006) 24.
[15] B.M. Marsh, J. Zhou, E. Garand, J. Phys. Chem. A 118 (2014) 2063.
[16] T.E. Cooper, P.B. Armentrout, J. Phys. Chem. A 113 (2009) 13742.
[17] M.F. Bush, J. Oomens, R.J. Saykally, E.R. Williams, J. Am. Chem. Soc. 130 (2008) 6463.
[18] M.F. Bush, J.T. O'Brien, J.S. Prell, C.-C. Wu, R.J. Saykally, E.R. Williams, J. Am. Chem. Soc. 131 (2009) 13270.
[19] M.F. Bush, R.J. Saykally, E.R. Williams, Chemphyschem: Eur. J. Chem. Phys. Phys. Chem. 8 (2007) 2245.
[20] M.F. Bush, R.J. Saykally, E.R. Williams, J. Am. Chem. Soc. 130 (2008) 15482.
[21] T.E. Cooper, J.T. O'Brien, E.R. Williams, P.B. Armentrout, J. Phys. Chem. A 114 (2010) 12646.
[22] J.T. O'Brien, E.R. Williams, Phys. Chem. A 115 (2011) 14612.
[23] S. Guan, A.G. Marshall, Int. J. Mass Spectrom. Ion Proc. 157–158 (1996) 5.
[24] J.S. Prell, J.T. O'Brien, E.R. Williams, J. Am. Soc. Mass. Spectrom. 21 (2010) 800.
[25] A.D. Becke, J. Chem. Phys. 98 (1993) 5648.
[26] C. Lee, W. Yang, R.G. Parr, Phys. Rev. B 37 (1988) 785.
[27] M.J. Frisch, G.W. Trucks, H.B. Schlegel, G.E. Scuseria, M.A. Robb, J.R. Cheeseman, G. Scalmani, V. Barone, B. Mennucci, G.A. Petersson, H. Nakatsuji, M. Caricato, X. Li, H.P. Hratchian, A.F. Izmaylov, J. Bloino, G. Zheng, J.L. Sonnenberg, M. Hada, M. Ehara, K. Toyota, R. Fukuda, J. Hasegawa, M. Ishida, T. Nakajima, Y. Honda, O. Kitao, H. Nakai, T. Vreven, J.A. Montgomery, J.E. Peralta, F. Ogliaro, M. Bearpark, J.J. Heyd, E. Brothers, K.N. Kudin, V.N. Staroverov, R. Kobayashi, J. Normand, K. Raghavachari, A. Rendell, J.C. Burant, J.M. Millam, S.S. Iyengar, J. Tomasi, M. Cossi, N. Rega, J.M. Millam, M. Klene, J.E. Knox, J.B. Cross, V. Bakken, C. Adamo, J. Jaramillo, R. Gomperts, R.E. Stratmann, O. Yazyev, A.J. Austin, R. Cammi, C. Pomelli, J.W. Ochterski, R.L. Martin, K. Morokuma, V.G. Zakrzewski, G.A. Voth, P. Salvador, J.J. Dannenberg, S. Dapprich, A.D. Daniels, O. Farkas, J.B. Foresman, J.V. Ortiz, J. Cioslowski, D.J. Fox, Gaussian 09, Revision A.02, Gaussian Inc., Pittsburgh, PA, 2009.
[28] A. Kamariotis, O.V. Boyarkin, S.R. Mercier, R.D. Beck, M.F. Bush, E.R. Williams, T. R. Rizzo, J. Am. Chem. Soc. 129 (2006) 11814.
[29] T.E. Cooper, D.R. Carl, P.B. Armentrout, J. Phys. Chem. A 113 (2009) 13727.
[30] J.P. Perdew, Phys. Rev. B 33 (1986) 8822.
[31] Y. Zhao, D.G. Truhlar, Theor. Chem. Acc. 120 (2008) 215.
[32] C. Moller, M.S. Plesset, Phys. Rev. 46 (1934) 618.
[33] C.W. Bauschlicher, H.J. Partridge, J. Chem. Phys. 103 (1995) 1788.
[34] R. Rios- Font, M. Sodupe, L. Rodriguez- Santiago, P.R. Taylor, J. Phys. Chem. A 114 (2010) 10857.
[35] N.S. Rannulu, M.T. Rodgers, Phys. Chem. Chem. Phys. 7 (2005) 1014.
[36] Z. Yang, N.S. Rannulu, Y. Chu, M.T. Rodgers, J. Phys. Chem. A 112 (2008) 388.

Please cite this article in press as: A.F. Sweeney, et al., Structural elucidation of hydrated $CuOH^+$ complexes using IR action spectroscopy and theoretical modeling, Int. J. Mass Spectrom. (2014), http://dx.doi.org/10.1016/j.ijms.2014.08.037

CHAPTER 5

GUIDED ION BEAM STUDIES OF THE COLLISION-INDUCED DISSOCIATION OF $CuOH^+(H_2O)_n$ (n = 1 – 4): COMPREHENSIVE THERMODYNAMIC DATA FOR COPPER ION HYDRATION

THE JOURNAL OF PHYSICAL CHEMISTRY A

Article

pubs.acs.org/JPCA

Guided Ion Beam Studies of the Collision-Induced Dissociation of $CuOH^+(H_2O)_n$ (n = 1–4): Comprehensive Thermodynamic Data for Copper Ion Hydration

Andrew F. Sweeney and P. B. Armentrout*

Department of Chemistry, University of Utah, 315 South 1400 East, Rm 2020, Salt Lake City, Utah 84112, United States

Supporting Information

ABSTRACT: Threshold collision-induced dissociation (TCID) using a guided ion beam tandem mass spectrometer is performed on $CuOH^+(H_2O)_n$ where n = 1–4. The primary dissociation pathway for the n = 2–4 reactants consists of loss of a single water molecule followed by the sequential loss of additional water molecules at higher collision energies. The n = 1 reactant departs from this trend by losing the OH ligand and the H_2O ligand competitively. Loss of the OH ligand is thermodynamically favored, whereas H_2O loss is the kinetically favored process, consistent with heterolytic cleavage of the dative bond. The data are analyzed using a statistical model after accounting for internal and kinetic energy distributions, multiple collisions, and kinetic shifts to obtain 0 K bond dissociation energies (BDEs). These are also converted using a rigid rotor/harmonic oscillator approximation to yield thermodynamic values at room temperature. Experimental BDEs are compared to theoretical BDEs determined at the B3LYP, cam-B3LYP, B3P86, M06, CCSD(T), and MP2(full) levels of theory with a 6-311+G(2d,2p) basis set using geometries and vibrational frequencies determined at the B3LYP/6-311+G(d,p) level. In addition, BDEs for the loss of OH from $CuOH^+(H_2O)_n$ where n = 0, 2–4 are derived using the experimental BDEs for dissociation of $CuOH^+(H_2O)_n$ and literature values for $Cu^+(H_2O)_n$.

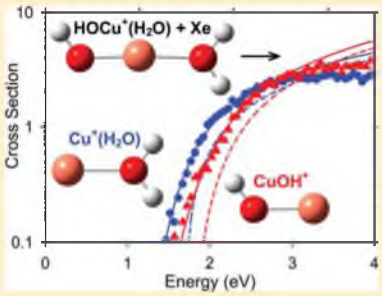

INTRODUCTION

As an abundant trace element, copper is necessary for a wealth of biological processes including gene expression,[1,2] photosynthesis,[3,4] and growth and metabolism.[5] Additionally, copper is a cofactor for a number of key enzymes.[6−11] The ubiquitous nature of copper is not isolated to biological systems. Indeed, copper is the most common toxic heavy metal used in industrial practices,[5] which has contributed to its increased concentrations in aquatic environments[12,13] leading to toxicity[14] and phytotoxicity.[15] For these reasons, its concentration in drinking water supplies is regulated by the EPA.[16] In order to fully understand the role copper plays in any of these systems, it would be useful to better develop our understanding of copper hydration at a fundamental level.

Previous studies toward this goal have investigated a range of hydrated copper systems including $Cu^{2+}(H_2O)_n$,[17−19] $Cu^+(H_2O)_n$,[20−23] and $CuOH^+(H_2O)_n$.[17,24−26] In many of these studies, hydrated copper systems are compared to other hydrated transition metal cations to ascertain periodic trends. In these comparisons, copper systems are often found to represent extremes to the trends or exceptions to them altogether. For instance, fast atom bombardment (FAB) studies by Michl and co-workers[21] revealed that $MOH^+(H_2O)_n$ and $M^+(H_2O)_n$ were present simultaneously for first-row transition metals of groups 4–8. In contrast, competition between these two systems was not seen for Cu as only the $Cu^+(H_2O)_n$ system was present.[21] Siu and co-workers performed a similar study by looking at the collision-induced dissociation (CID) of $M^{2+}(H_2O)_n$ for a variety of transition metal species and found that, at certain sizes, each metal complex undergoes a charge separation process to form $MOH^+(H_2O)_m$ + $H_3O^+(H_2O)_{n-m-2}$.[18] The minimum size at which water loss was favored over this charge separation process was notably higher for copper than for all but one of the dozen other metals investigated, which was presumed to be because of its higher second ionization energy.

The interesting chemistry involved with the charge separation mechanism has elicited a litany of studies focused on the $CuOH^+(H_2O)_n$ system, which is further investigated in the present study. Among these studies is work by Goddard and co-workers who used the Continuum Solvent Model (COSMO)[27] in conjunction with B3LYP to theoretically characterize and provide relative energetics for $CuOH^+(H_2O)_n$ where n = 3, 4, 5, 7, and 17.[24] They found that n = 3–5 complexes preferred a coordination number (CN) of 4, whereas n = 7 and 17 complexes preferred a CN = 5 because of the presence of a second solvent shell. However, the energetic differences between CN = 4 and 5 were less than 10 kJ/mol for all complexes, which suggested that the two species could rapidly interconvert. Experimentally, Garand and co-workers used cryogenic ion spectroscopy to examine the OH stretching region of D_2 tagged $CuOH^+(H_2O)_n$ where

Received: September 4, 2014
Revised: October 10, 2014
Published: October 10, 2014

   dx.doi.org/10.1021/jp508962d | J. Phys. Chem. A 2014, 118, 10210−10222

n = 1−3.[25] Like Goddard and co-workers, they found a preference for CN = 4 for n = 3, although they could not rule out contributions from multiple isomers for complex sizes as small as n = 2. They were unable to obtain spectra for $CuOH^+(H_2O)_n$ complexes larger than n = 4, presumably because the fourth water is weakly bound in a second solvent shell.[21]

Most recently, in collaboration with Williams and O'Brien at UC Berkeley, we used infrared photodissociation (IRPD) in the OH stretching region in conjunction with theoretically predicted spectra to characterize the structures of $CuOH^+(H_2O)_n$, where n = 2−9, trapped in a Fourier transform ion cyclotron resonance (FTICR) mass spectrometer.[26] As in the theoretical study of Goddard and co-workers, we found experimentally that the $CuOH^+(H_2O)_n$ system prefers an inner shell CN = 4, although contributions from CN = 5 isomers were clearly present for n = 7 and could not be ruled out for other complexes. In agreement with the spectra of Garand and co-workers, contributions from multiple isomers could be seen in the n = 2 spectrum, although the low intensity of the corresponding bands indicates that these isomers were likely to be small in abundance.

Although structures of hydrated copper systems have now been well-characterized using both experimental and theoretical measures, the thermodynamics of these systems are still incomplete. Previous thermodynamic studies include only the $Cu^+(H_2O)_n$ system. Bond dissociation energies (BDEs) for $Cu^+(H_2O)_n$ where n = 3−5 were first measured by Castleman and co-workers using equilibrium methods and observed to increase with decreasing n.[20] The n = 1−4 complexes of the same system were later studied by Michl and co-workers using fast atom bombardment (FAB) techniques with a triple quadrupole mass spectrometer.[21] Quantitative discrepancies between those two studies motivated a subsequent guided ion beam study by Dalleska et al.[22] They found that the BDEs for n = 4 and 3 were nearly the same whereas the BDE for n = 2 was much higher and also slightly higher than that for n = 1.[22] These results gave revised BDEs that were in accord with the previous studies[21] and were aligned with observations by Magnera, David, and Michl[28] and Marinelli and Squires[29] who found that the n = 2 water is bound to some first-row transition metals ions more strongly than the first.

In the current study, we use threshold collision-induced dissociation (CID) in a guided ion beam tandem mass spectrometer (GIBMS) to quantitatively investigate the thermochemistry of the $CuOH^+(H_2O)_n$ system for n = 1−4. Analysis of kinetic energy dependent CID cross sections yields 0 K BDEs for these complexes. The present results represent the first experimentally determined BDEs for the $CuOH^+(H_2O)_n$ system. Interestingly, the $CuOH^+(H_2O)$ complex loses both H_2O and OH competitively to form $CuOH^+$ and $Cu^+(H_2O)$ products, respectively. Here, the thermodynamics for both channels are characterized for the first time. This thermochemistry is then combined in a thermodynamic cycle with previous measurements of the $Cu^+(H_2O)_n$ systems to yield the $HO-Cu^+(H_2O)_n$ BDEs for n = 0 and 2−4. The Cu^+−OH bond energy is compared with previous values for related CuX^+ (X = CH_3 and NH_2) and MOH^+ systems to evaluate the periodic trends.

EXPERIMENTAL AND THEORETICAL SECTION

Instrumentation. Hydrated copper hydroxide ions are created from a 10^{-4} M solution of $CuSO_4$ in neat water using electrospray ionization (ESI) techniques. The solution is advanced at a rate of 0.05 mL/h through a 35 gauge stainless steel needle that has an applied voltage of ∼2 kV. Once in the gas phase, ions enter the vacuum system through a stainless steel cap with an inlet diameter that can range in size to help regulate pressure in the front end of the instrument. This affects not only reactant ion throughput but also collisional cooling. Ions then drift through a 4 in. long capillary that is heated to a temperature of 80 °C in order to desolvate large droplets. An 88 plate radio frequency (rf) ion funnel (IF) with superimposed dc gradient field, copied from a design described in detail elsewhere,[30] collects and focuses the ions to increase signal intensity.[31,32] The voltage bias between the first and last plate of the ion funnel is kept below 10 V to minimize heating of the ions. At the end of the funnel, the ions enter an rf-only hexapole with rf amplitudes typically set at 250 V peak to peak. Here, they undergo cooling by $>10^4$ thermalizing collisions with ambient gas (largely air and water).[33] This ensures that ions beyond the hexapole are well-defined by a Maxwell−Boltzmann distribution of rovibrational states at room temperature.[33−38] To preferentially increase the intensity of the n = 2 and 3 complexes, we use a set of dc electrodes located between each hexapole rod. These electrodes act as an in-source fragmentation technique, as described in detail elsewhere.[36] Judicious placement of the electrodes allows rethermalization of the newly formed fragment ion, as demonstrated elsewhere.[36−40]

Ions generated in the ESI/IF/hexapole source[33] then enter the guided ion beam tandem mass spectrometer[41,42] where they are focused into a magnetic momentum analyzer for mass selection. These reactant ions are decelerated to a known kinetic energy and injected into an rf octopole ion guide[43] where they pass through a collision cell containing Xe at low pressures. Xenon is used for reasons described elsewhere.[22,44] Product and remaining reactant ions drift out of the octopole and are mass selected using a quadrupole mass filter before being detected using a Daly detector.[45]

Data Analysis. Producing accurate thermodynamic information requires diligent consideration of many experimental factors that convolute the raw data. These factors include but are not limited to internal and kinetic energy distributions of the ionic and neutral reactants, lifetime effects that arise from a finite experimental time window, the probability of multiple collisions, and competition from other chemical and physical processes.

The measured intensities of the reactant and product ions are converted to absolute cross sections using the Beer−Lambert analogue

$$I = I_0 \exp(-\rho\sigma l) \quad (1)$$

where I is the reactant ion intensity after the collision cell, I_0 is the reactant ion intensity before the collision cell, ρ is the number density of the neutral reactant, σ is the total reaction cross section, and l is the length of the collision cell, 8.6 cm. The advantage of the guided ion beam method is that very few ions are lost such that $I_0 - I = \sum I_p$ the sum of all product ion intensities. The relative energy of the reactants is converted from the lab frame voltage, V_{lab}, to the center of mass energy, E_{CM}, using eq 2

$$E_{CM} = qV_{lab}m/(m + M) \quad (2)$$

where m is the mass of the reactant neutral, M is the mass of the reactant ion, and q is the charge of the ion. E_{CM} represents the amount of energy actually available for reaction, which is a

dx.doi.org/10.1021/jp508962d | J. Phys. Chem. A 2014, 118, 10210−10222

crucial metric when dealing with thermodynamic quantities. The kinetic energy distribution of the ions is determined at the beginning of each experiment using retarding potential analysis.[41] This also allows the absolute zero of energy to be obtained such that it can be subtracted from V_{lab}. Experimental collisions are performed at three different pressures of the Xe neutral gas, typically ~0.2, 0.1, and 0.05 mTorr. The cross sections at each pressure are used to linearly extrapolate to a zero pressure cross section, which rigorously represents a single collision event. The final step toward conversion of the raw data is a background subtraction. This is accomplished by measuring the reactant and product ion intensities with and without gas in the collision cell. In this way, product ion intensities resulting from dissociation outside the collision cell as well as background noise in the detector are removed.

The kinetic energy dependent cross section for the loss of a ligand is modeled using the empirical model shown in eq 3

$$\sigma_j(E) = \sigma_0 \sum_i g_i (E + E_i - E_{0,j})^N / E \tag{3}$$

where σ_0 is an energy independent scaling factor, E is the relative collision energy, $E_{0,j}$ is an adjustable parameter representing the reaction threshold for channel j at 0 K, N describes the energy deposition function,[42] and the summation is over the rovibrational states of the reactant ion having energies E_i and populations g_i, where $\sum g_i = 1$. Rovibrational states taken from quantum chemical calculations of the ground state structures are directly counted using the Beyer–Swinehart–Stein–Rabinovitch[46−48] algorithm and are assigned populations, g_i, on the basis of a Maxwell–Boltzmann distribution at 300 K. As the size of the reactants increases, the number of accessible rovibrational states will also increase such that dissociative lifetimes near the threshold energy can be longer than the experimental time-of-flight, $\tau \sim 5 \times 10^{-4}$ s.[42] For this reason, the apparent dissociation thresholds for larger reaction complexes shift to higher energies. This kinetic shift is accounted for using Rice–Ramsperger–Kassel–Marcus (RRKM) statistical theory[49−51] for unimolecular dissociation and is incorporated into the cross section model, as seen in eq 4.

$$\sigma_j(E) = \left(\frac{n\sigma_{0,j}}{E}\right) \sum_i g_i \int_{E_{0,j}-E_i}^{E} \left[\frac{k_j(E^*)}{k_{tot}(E^*)}\right] (E - \varepsilon)^{N-1} P_{D1} \, d(\varepsilon) \tag{4}$$

Here, ε is the energy that is deposited into internal modes of the reactant ion complex during collision, $P_{D1} = 1 - \exp(-k_{tot}(E^*)\tau)$ is the dissociation probability, and $k_j(E^*)$ is the RRKM unimolecular rate constant for dissociation into channel j where the available energy is $E^* = E_i + \varepsilon$. Should the dissociative lifetime of the energized molecule (EM) be shorter than the average experimental time frame, the integration in eq 4 recovers eq 3. Equation 4 also accounts for the competition between multiple dissociation pathways using the $k_j(E^*)/k_{tot}(E^*)$ ratio, which uses statistical theory[52,53] to estimate the rate for each reaction channel j. The rate coefficients, $k_j(E^*)$, are defined by RRKM theory as in eq 5

$$k_{tot}(E^*) = \sum_j k_j(E^*) = \sum_j d_j N_j^{\ddagger}(E^* - E_{0,j}) / h\rho(E^*) \tag{5}$$

where d_j is the reaction degeneracy of channel j, $N_j^{\ddagger}(E^* - E_{0,j})$ is the sum of rovibrational states of the transition state (TS), and $\rho(E^*)$ is the density of states of the EM at E^*. Water loss for hydrated metal cation species is a heterolytic bond cleavage that can be characterized as proceeding over a loose transition state (TS).[54] In this work, the TS is treated at the phase space limit (PSL) in which the transitional modes are rotors.[52] Loss of an OH ligand also proceeds over a loose TS but only occurs from the $CuOH^+(H_2O)$ reactant where it is competitive with loss of H_2O. Therefore, modeling of its threshold requires competitive modeling of both dissociation pathways, as successfully applied in several previous studies.[53,55−60] All molecular parameters for the TS and EM are taken from quantum chemical calculations described below.

Cross sections for the loss of an additional water ligand are modeled by combining eq 4, which reproduces the cross section of the primary dissociation product, with the probability for further dissociation[61] given by eq 6

$$P_{D2} = 1 - e^{-k_2(E_2^*)\tau} \tag{6}$$

where $E_2^* = E^* - E_{0,j} - T_1 - E_L$ is the internal energy of the product ion undergoing further dissociation. Statistical assumptions are used to assign the distributions for T_1 and E_L, which represent the translational energy of the primary products and the internal energy of the neutral product, respectively.

For both primary and secondary processes, the model cross sections of eqs 4 and 6 are convoluted over the kinetic energy distributions of the neutral and ion reactants before comparison to experimental data. The fitting parameters in these equations ($\sigma_{0,j}$, N, and $E_{0,j}$) are then optimized using a nonlinear least-squares criterion to reproduce the experimental data throughout the threshold region. The $E_{0,j}$ threshold energies obtained are equivalent to the 0 K binding energy of the ligand to the metal complex. The uncertainties in these binding energies are determined from the range of parameters obtained from modeling multiple data sets, scaling the quantum chemical vibrational energies by ±10%, varying the best fit N value by ±0.1, changing the experimental time-of-flight up and down by a factor of 2, and including the uncertainty in the energy scale, ±0.05 eV (lab).

Computational Details. In our previous study,[26] we conducted an exhaustive examination of low energy isomers for $CuOH^+(H_2O)_n$ where n = 2−9 for comparison to IRPD data. Included in that study were relative energies of each isomer calculated at temperatures specific to the FTICR experimental source conditions, which ranged from 130 to 450 K. In the GIBMS, however, source conditions ensure room temperature reactants, so relative free energies for the $CuOH^+(H_2O)_n$ complexes were recalculated here at 298 K in order to ascertain the relative populations of the various isomers. For comparison to our experimentally determined 0 K BDEs, theoretical 0 K BDEs were determined from the difference in energies of the ground state reactant complexes and their products including zero-point vibrational (scaled by 0.989)[62] corrections. Comparison with and without basis set superposition error (BSSE) corrections determined at the full counterpoise level[63,64] are also made. These calculations include the ground state structures for $CuOH^+(H_2O)_n$ where n = 1−4 (all doublet spin states), both possible dissociation products from the n = 1 reactant, $Cu^+(H_2O)$ + OH (singlet + doublet spin states) and $CuOH^+$ + H_2O (doublet + singlet spin

states), as well as $Cu^+(H_2O)_n$ where n = 1−4 (all singlet spin states). All low energy isomers were optimized at the B3LYP/6-311+G(d,p) level of theory.[65,66] Relative energetics are obtained using single point energy (SPE) calculations at the B3LYP, Coulomb attenuating method (cam) B3LYP,[67] B3P86,[68] M06,[69] and MP2(full)[70] levels with a 6-311+G-(2d,2p) basis set. Diffuse functions were used at every step because of their importance in describing the hydrogen bonding characteristics of hydration and solvation.[71,72] In a previous study of similar hydrated complexes,[73] we showed that geometry optimizations, vibrational frequencies, and energetics calculated at this level yielded no discernible differences from those calculated at alternate levels of theory, including B3LYP/6-311++G(d,p), BHandHLYP/6-311+G(d,p), BHandHLYP/6-311++G(d,p), and MP2(full)/6-311+G(d,p). Our use of MP2 with full electron correlation is predicated on previous results that show that frozen core calculations can lead to anomalous metal cation binding affinities.[74−76] Rotational constants and vibrational frequencies of the ground state isomers scaled by 0.989[77] were used to calculate the densities and numbers of states for each complex in our statistical modeling analysis. All quantum chemical calculations were performed using the Gaussian 09 suite of programs.[78]

RESULTS AND DISCUSSION

Theoretical Structures. Relative energies at 298 K of low-lying isomers of $CuOH^+(H_2O)_n$ for n = 2−4 are shown in Table 1. For n = 3 and 4, the predicted ground isomer was not unanimous across all four levels of theory investigated, although in both cases, three of the levels had the same ground isomer. For n = 1 and 2, all levels predict the same ground isomer. Ground isomers of all species considered here are shown in Figure 1a. We use an (x,y) nomenclature to describe each unique structure where x + 1 = CN and y = the number of waters in the second solvent shell. To further distinguish isomers, hydrogen bonding of second shell waters is denoted using an A/D nomenclature where A refers to a water molecule accepting a single hydrogen bond and D refers to a water molecule donating a single hydrogen bond. Binding to the OH ligand rather than a water ligand is specified by an OH subscript.

Table 1. Theoretical Relative Free Energies (kJ/mol) of $CuOH^+(H_2O)_n$ Isomers at 298 K[a]

	complex	MP2(full)	M06	B3LYP	B3P86
$CuOH^+(H_2O)_2$	(2,0)	0.0[b]	0.0	0.0	0.0
	(1,1)_A_t	31.9[b]	29.3	22.5	24.8
	(1,1)_A_c	32.4[b]	29.8	23.1	25.4
	(1,1)_A_{OH}	46.0[b]	45.6	42.7	46.5
$CuOH^+(H_2O)_3$	(3,0)	0.0	0.0	1.1	0.0
	(3,0)C_s	4.8	1.6	2.5	0.7
	(2,1)_AA	33.4	7.6	0.0	3.9
	(2,1)_A	43.0	16.3	7.2	11.1
$CuOH^+(H_2O)_4$	(3,1)_AA	0.0	0.0	0.0	1.2
	(4,0)	3.1	1.3	1.4	0.0
	(3,1)_AD_{OH}	5.8	1.6	0.1	1.3
	(3,1)_AA_{OH}	13.4	10.1	9.1	10.7

[a]Single point energies calculated at the level shown using a 6-311+G(2d,2p) basis set using geometries, zero point energy corrections (scaled by 0.989), and thermal corrections calculated at the B3LYP/6-311+G(d,p) level of theory. [b]CCSD(T) results.

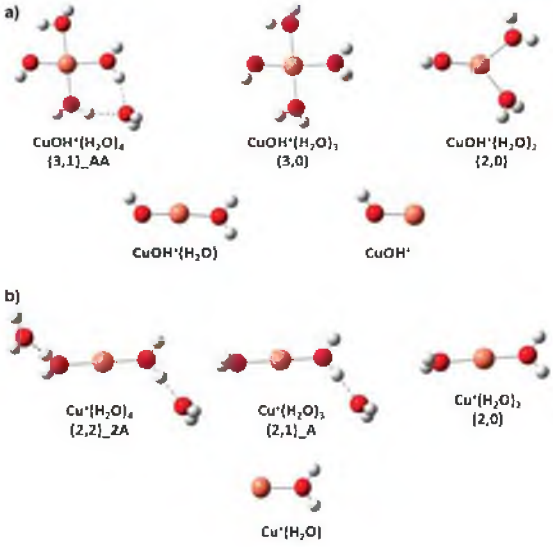

Figure 1. Ground isomers of (a) $CuOH^+(H_2O)_n$ and (b) $Cu^+(H_2O)_n$ calculated at the B3LYP/6-311+G(d,p) level.

At n = 4, the ground isomer is a 4-coordinate structure with a single water molecule in the second shell acting as a double hydrogen bond acceptor, (3,1)_AA, Figure 1a, as also found by Goddard and co-workers.[24] Here, the Cu−OH bond length is 1.83 Å, with Cu−OH_2 bond lengths of 2.01, 2.01, and 2.05 Å. Oxygen atoms for this complex are nearly coplanar with the copper center, as verified by OCuOO dihedral angles of >178°. B3P86 predicts the (4,0) isomer to be 1.2 kJ/mol lower in energy than the (3,1)_AA ground isomer of the other levels. Higher lying isomers have the second shell water binding to the OH ligand either as a donor, (3,1)_AD_{OH}, or acceptor, (3,1)_AA_{OH}. Energetic differences among the four lowest isomers of $CuOH^+(H_2O)_4$ are <14 kJ/mol.

For n = 3, three levels of theory predict the (3,0) square planar ground structure, whereas B3LYP predicts the (2,1)_AA structure to be 1.1 kJ/mol lower in energy. Note that there are two (3,0) isomers in Table 1, (3,0) and (3,0)C_s, which differ primarily in orientation of the OH and adjacent water molecule. The (3,0)C_s isomer contains a plane of symmetry, whereas the (3,0) isomer exhibits no such symmetry as the OH and H_2O ligands participate in hydrogen bonding that slightly reduces the relative energy of the structure. Table 1 shows that at room temperature energetic differences between these two isomers are between 1 and 5 kJ/mol. Energetic differences between all n = 3 isomers are similar among M06, B3LYP, and B3P86 levels of theory with the largest difference being ~16 kJ/mol, whereas MP2(full) gives relative energies that are considerably larger for the (2,1) isomers. The (3,0) structure is the result of losing the second shell water molecule from the (3,1)_AA ground structure of n = 4, and its geometry is comparable to geometries found by Goddard and co-workers[24] and Garand and co-workers.[25] In our calculations of the (3,0) complex, the Cu−OH bond length is 1.84 Å, with Cu−OH_2 bond lengths equaling 2.03, 2.04, and 2.04 Å. Like the n = 4 ground isomer, oxygen atoms for this species are nearly coplanar with the copper center (dihedral angles >177°).

dx.doi.org/10.1021/jp508962d | J. Phys. Chem. A 2014, 118, 10210−10222

Table 2. Optimized Parameters of Equation 4 from Analysis of CID Cross Sections[a]

reactant	product	σ_0[b]	N[b]	E_0[c] (eV)	E_0[b] (PSL, eV)	$\Delta S^{\ddagger}_{1000}$ (J/mol K)
$CuOH^+(H_2O)_4$[d]	$CuOH^+(H_2O)_3$	50 (3)	1.0 (0.2)	0.66 (0.06)	0.59 (0.07)	56 (5)
$CuOH^+(H_2O)_4$[e]	$CuOH^+(H_2O)_3$	45 (2)	1.0 (0.1)		0.59 (0.04)	56 (5)
	$CuOH^+(H_2O)_2$	0.50 (0.03)			1.58 (0.04)	
$CuOH^+(H_2O)_3$[d]	$CuOH^+(H_2O)_2$	45 (2)	0.9 (0.1)	0.95 (0.04)	0.93 (0.03)	53 (5)
$CuOH^+(H_2O)_3$[e]	$CuOH^+(H_2O)_2$	121 (4)	0.9 (0.1)		0.92 (0.03)	53 (5)
	$CuOH^+(H_2O)$	64 (3)			2.22 (0.03)	
$CuOH^+(H_2O)_2$[d]	$CuOH^+(H_2O)$	30 (3)	0.9 (0.1)	1.33 (0.08)	1.31 (0.08)	22 (5)
$CuOH^+(H_2O)$[d]	$Cu^+(H_2O)$	10 (1)	1.1 (0.3)	1.80 (0.13)[f]	1.80 (0.05)	26 (4)
	$CuOH^+$	1.7 (0.7)		1.96 (0.16)[f]	1.86 (0.05)	40 (5)

[a]Uncertainties in parentheses. [b]Parameters for modeling where lifetimes effects are taken into account. [c]Threshold values for modeling where lifetime effects are not included. [d]Single channel modeling using eq 4. [e]Sequential dissociation modeling using eqs 4 and 6. [f]Modeling of individual channels without competition.

At n = 2, all levels of theory predict the ground structure to be (2,0). Loss of a water ligand from the n = 3 complex to form the n = 2 complex reduces the CN of the copper ion from 4 to 3. The resulting geometry is a near trigonal planar complex described by an OCuO angle of 91° between the waters and OCuO angles of 136° and 132° between the waters and the hydroxide. Oxygen atoms of H_2O and OH ligands are nearly coplanar with Cu (dihedral angles >169°). Here, the Cu−OH bond length is 1.77 Å, with Cu−OH_2 bond lengths of 2.00 and 2.02 Å. (Alternative levels of theory provide different structures. MP2(full)[26] and CCSD(T) theory[25] yield a more T-shaped molecule, but the relative energetics are affected only slightly.) The next lowest energy isomer at the M06, B3LYP, and B3P86 levels of theory is (1,1)_A_t, where the t subscript indicates that the water in the second solvent shell and the hydrogen on the OH ligand are trans to one another (whereas the c subscript indicates a cis structure). Energetic differences between this structure and the ground isomer at these levels of theory are 22−32 kJ/mol. MP2(full) also predicts (2,0) as the ground isomer but with much larger differences to (1,1) isomers and fails to yield reasonable results for (1,1)_A_{OH} for reasons that are unclear.[26] Hence, CCSD(T) results are given for this complex in Table 1.

At n = 1, the OCuO angle is 175°, and the molecule exhibits C_s symmetry with all hydrogens in the plane. In this complex, the Cu−OH bond length is 1.76 Å and the Cu−OH_2 bond length is 1.91 Å. The structures of $CuOH^+$ and $Cu^+(H_2O)$ both have HOCu angles of 126° and exhibit C_s and C_{2v} symmetry, respectively. Now the Cu−OH bond length is 1.82 Å, and the Cu−OH_2 bond length is 2.05 Å. Note that the shorter bond lengths in the $CuOH^+(H_2O)$ complex compared with $CuOH^+$ and $Cu^+(H_2O)$ indicate a synergistic interaction between the two ligands. This can be thought of as enhancing the electron transfer from Cu to OH, leading to more $Cu^{2+}OH^-$ character in the n = 1 complex than in $CuOH^+$ alone.

The symmetry of the $CuOH^+(H_2O)$ complex shows that the dipole moment of the water ligand is pointed directly at Cu. As more waters are added to this n = 1 complex, the dipole moments for each water ligand become misaligned with Cu because of hydrogen bonding. For instance, in $CuOH^+(H_2O)_2$, the water dipole moments point 23° and 28° away from Cu. In the $CuOH^+(H_2O)_3$ (3,0) ground isomer, the water molecule that hydrogen bonds to the backside of the OH ligand (top in Figure 1a) has a dipole moment that is 53° away from Cu. This interaction also twists the OH ligand toward the plane of the complex as indicated by a HOCuO dihedral angle of 139°, which contrasts with a HOCuO dihedral angle of 95° for n = 2 where the OH ligand is nearly perpendicular to the plane of the complex. The other water ligand adjacent to the OH ligand in n = 3 has its dipole 35° from being directed at Cu, and the opposite water is nearly aligned at 6°. The slight deviation from alignment is a result of the uneven hydrogen bonding among the various ligands. For the $CuOH^+(H_2O)_4$ (3,1)_AA ground isomer, the addition of a water to the second shell represents the strongest hydrogen bonding environment. Whereas the OH and its hydrogen bonding neighbor are oriented nearly the same as in the (3,0) complex, dipole moments for the two inner shell donor water ligands now reorient such that their dipoles are 23° and 28° away from Cu.

For analysis of the CID cross sections and for calculating BDEs, the (3,1)_AA, (3,0), and (2,0) structures were used for n = 4, 3, and 2 complexes, respectively, Figure 1a. Each of these structures was predicted to be the ground isomer by at least three of the four levels of theory considered. Experimentally, the (2,0) structure was found by Garand and co-workers to reproduce the IR spectrum of cryogenically cooled $CuOH^+(H_2O)_n$ complexes.[25] Additionally, our previous study[26] revealed that the (3,1)_AA and (3,0) isomers were the main contributors to IRPD spectra for n = 4 and n = 3 spectra, respectively, although small contributions from the (4,0) and (2,1)_AA isomers could not be ruled out. Excluding MP2(full) relative energies, for reasons described below, the energetic differences between these isomers and the predicted ground isomers at 298 K are 1−2 and 4−8 kJ/mol, respectively. As a result, the choice of ground isomers will change the theoretical BDEs by very little. For experimental BDEs, previous work done in this lab on the hydration energies of Zn^{2+} complexes has shown that using different isomers in our statistical analysis can change the measured BDE[73] because different isomers have different rovibrational state densities that can yield different kinetic shifts. The small systems investigated here have significantly fewer degrees of freedom than those investigated in that study, 9−45 versus 66−93, and as such have significantly smaller kinetic shifts. Therefore, the changes in the measured BDEs are significantly smaller as well. Indeed, modeling of the experimental cross sections for n = 4 using either of the (4,0), (3,1)_AD_{OH}, or (3,1)_AA reactant isomers with the (2,1)_A or (3,0) product isomers yielded negligible changes in the measured thresholds. Similarly, modeling of the experimental cross sections with (eq 4) and without (eq 3) lifetime effects for each complex size gives experimental thresholds that change little, as shown in Table 2, but the differences do increase with n, from 0.02 eV for n = 2 to 0.07 eV for n = 4. For the n = 1 complex, the comparison of the

threshold for formation of $CuOH^+ + H_2O$ determined with and without explicit consideration of the competition with the lower energy $Cu^+(H_2O) + OH$ channel shows a shift of 0.10 eV.

Experimental Results. Experimental cross sections for collision-induced dissociation with Xe were measured for $CuOH^+(H_2O)_n$ where n = 1–4. Figure 2 shows the largest

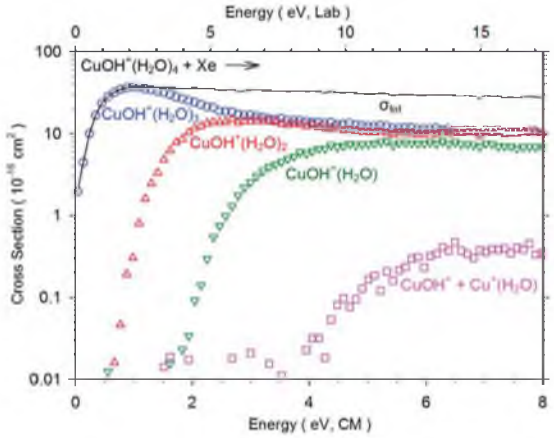

Figure 2. CID cross sections for sequential dissociations of $CuOH^+(H_2O)_4$ colliding with 0.2 mTorr of Xe as a function of energy in the laboratory (upper x-axis) and center-of-mass (lower x-axis) frames. The line shows the total cross section.

reactant $CuOH^+(H_2O)_4$ colliding with Xe to form products. The primary dissociation pathway consists of loss of a single water molecule to form $CuOH^+(H_2O)_3$ and is followed by the sequential loss of two additional water molecules at higher energies to give $CuOH^+(H_2O)$. The least intense cross section occurs at substantially higher collision energies and is the sum of $CuOH^+$ and $Cu^+(H_2O)$, which are unresolved in this experiment. Note that the probability of $CuOH^+(H_2O)_4$ dissociating into $CuOH^+(H_2O)_3$ at room temperature exists even at a collision energy of 0 eV. This indicates that the BDE of the fourth water in $CuOH^+(H_2O)_4$ is comparable to the internal energy content of the complex, a conclusion posited by Garand and co-workers.[25] As an additional water is expected to be even less strongly bound, this explains why we were unable to create $CuOH^+(H_2O)_5$ or larger complexes in appreciable intensity at 298 K.

We model the cross sections for the n = 1–4 reactants colliding with Xe to ascertain dissociation thresholds at each complex size, with optimized parameters given in Table 2. In all cases, the primary dissociation channel is loss of a water ligand with OH loss being competitive for n = 1. Cross sections for the primary and sequential dissociation products were analyzed using eqs 4 and 6 to obtain 0 K BDEs for the n = 2–4 systems. For n = 1, the OH and the H_2O ligands bind with similar energies such that competitive modeling of these cross sections using eq 4 is needed to acquire accurate 0 K thresholds for both pathways.

Cross sections for the products resulting from collisions of $CuOH^+(H_2O)_n$ with Xe are shown in Figure 3 after extrapolation to zero pressure. For the n = 4 complex, Figure 3a, analysis of the total cross section using eq 4 yields a threshold for loss of a single water molecule of 0.59 ± 0.07 eV. When the sequential model, eqs 4 and 6, is included, this threshold remains the same with the sequential loss of an additional water molecule requiring 1.58 ± 0.04 eV. The difference between these two thresholds can be measured with more precision than the absolute values for each threshold because many systematic sources of uncertainty cancel. This difference should equal the $CuOH^+(H_2O)_2$–(H_2O) bond energy, which can also be measured from the primary dissociation channel of $CuOH^+(H_2O)_3$, as shown in Figure 3b. Indeed, this threshold of 0.93 ± 0.03 eV does agree reasonably well with the 0.99 ± 0.02 eV difference between primary and sequential threshold energies for $CuOH^+(H_2O)_4$. Sequential modeling of the n = 3 reactant gives thresholds of 0.92 ± 0.03 and 2.22 ± 0.03 eV for the first and second water losses, respectively. The difference between thresholds, 1.30 ± 0.02 eV, now matches the threshold for single water loss from $CuOH^+(H_2O)_2$, 1.31 ± 0.08 eV, Figure 3c. Individual cross sections for the loss of the OH and the H_2O ligand from the n = 2 complex were too small to analyze independently. The apparent onset of the total cross section for these sequential products can be seen to be ~3 eV, nearly 2 eV higher than the onset of the primary dissociation product, $CuOH^+(H_2O)$. This approximately agrees with the directly measured threshold for dissociation of this species.

Competitive analysis of the $CuOH^+(H_2O)$ dissociation cross sections, Figure 3d, reveals a dissociation threshold for OH loss of 1.80 ± 0.05 eV and a threshold for H_2O loss of 1.86 ± 0.05 eV, with a difference measured more precisely as 0.06 ± 0.02 eV. Although loss of OH is energetically more favorable at n = 1, loss of H_2O is entropically more favorable as is indicated by its higher cross section above 3 eV. Loss of H_2O is entropically favored because it creates products with more rotational degrees of freedom, which then create a higher number of states at the PSL transition state.

Comparison of Experimental and Theoretical Bond Energies: $CuOH^+(H_2O)_{n-1}$–(H_2O). As noted above, there is generally good agreement between the primary and secondary bond energies determined using the models of the total cross sections and individual product cross sections. In general, the models of the total cross sections provide the best experimental information as fewer assumptions associated with the modeling are needed. Therefore, in the following, we take the thresholds from the single channel modeling of the total cross section to be our best experimental BDEs for the $CuOH^+(H_2O)_n$ complexes where n = 2–4, as listed in Table 3. For comparison, theoretical BDEs were calculated at the B3LYP, B3P86, M06, MP2(full), CCSD(T), and cam-B3LYP levels of theory using a 6-311+G(2d,2p) basis set and structures and zero point energy corrections calculated at the B3LYP/6-311+G(d,p) level. As noted above, these structures were verified to be the ground isomer in our previous IRPD study.[26]

The MP2(full) results are described in the Supporting Information. Although MP2(full) BDEs show good agreement for n = 4, 3, and 1 dissociating to lose H_2O, it gives obviously incorrect results for dissociation of n = 2 (off-scale in Supporting Information Figure S1) as well as n = 1 dissociating to lose OH. Despite a variety of computational efforts, repeated several times, these anomalous results could not be resolved. To probe the cause of these errors, SPEs were calculated at the CCSD(T) level with the same basis set. Details of these efforts including BDEs calculated at the MP2(full), MP2, MP3, MP4DQ, CCSD, and CCSD(T) levels of theory are given in the Supporting Information. The CCSD(T) BDEs were in

dx.doi.org/10.1021/jp508962d | J. Phys. Chem. A 2014, 118, 10210–10222

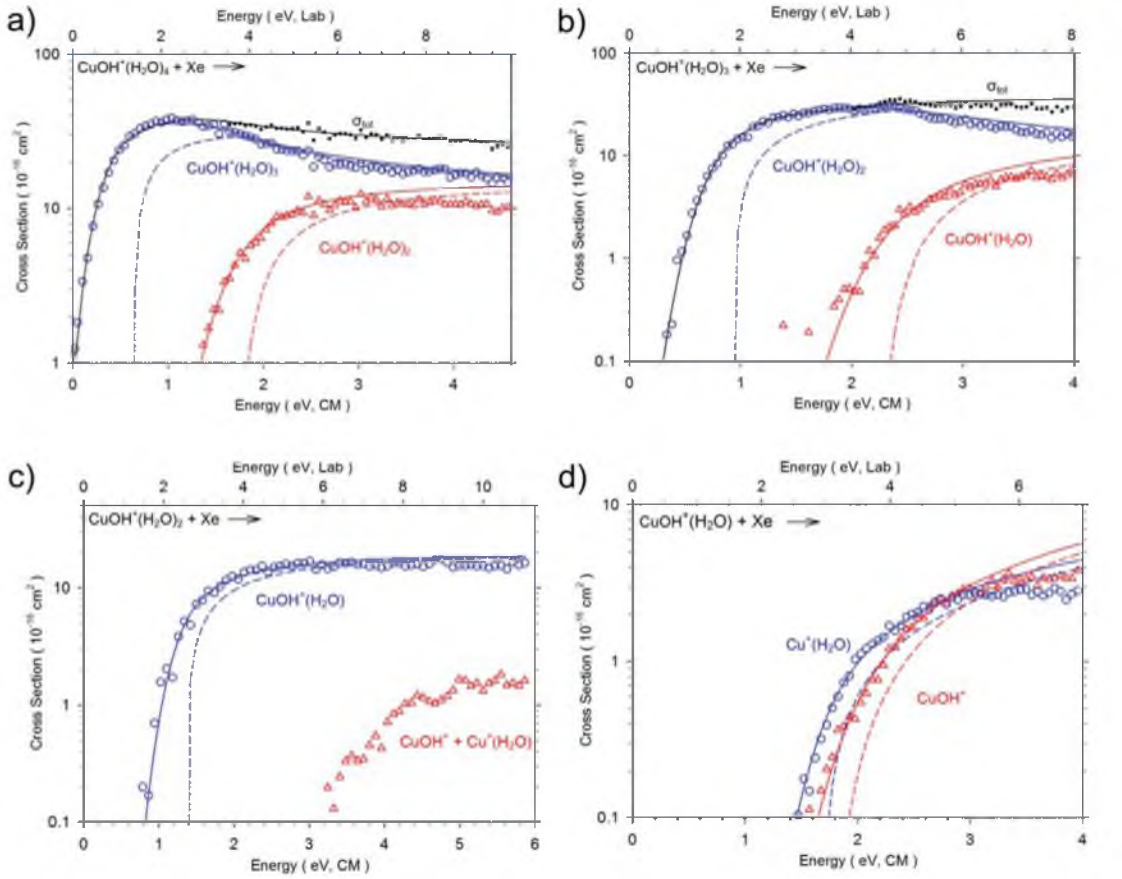

Figure 3. Zero pressure extrapolated cross sections for the CID of $CuOH^+(H_2O)_n$ with Xe for n = 4–1 (parts a–d). Solid lines show the best fits to the primary, secondary, and total water loss cross sections using eqs 4 and 6 convoluted over the kinetic and internal energy distributions of the neutral and ion. Dashed lines show the models in the absence of experimental kinetic energy broadening for reactants with an internal energy of 0 K. Optimized parameters for these fits are found in Table 2. In part c, the total cross section for sequential dissociation of the $CuOH^+(H_2O)$ primary product is shown in red.

Table 3. Comparison of Experimental 0 K Bond Energies (kJ/mol) to Theoretical Values[a]

$CuOH^+(H_2O)_{n-1}$-(H_2O)	expt[b]	B3LYP[c]	B3P86[c]	M06[c]	CCSD(T)[c]	cam-B3LYP[c]	cam-B3LYP/TZVP[d]
n = 4	56.9 ± 6.3	61.6 (64.6)	64.7 (67.8)	67.5 (70.4)	(69.4)	70.1 (73.0)	76.0 (80.5)
3	89.3 ± 3.3	65.9 (69.8)	73.9 (77.9)	78.9 (83.1)	(94.3)	79.5 (83.3)	83.0 (91.5)
2	126.4 ± 7.6	100.1 (103.4)	106.3 (109.7)	105.3 (109.0)	(108.6)	110.3 (113.4)	114.9 (122.0)
1	179.5 ± 4.8	190.0 (193.9)	195.1 (199.2)	185.5 (190.4)	(179.7)	199.1 (202.7)	203.7 (210.9)
MAD[e]	5.5[f]	16.2 (16.2)	14.7 (14.7)	12.0 (12.0)	(8.9)	14.7 (14.6)	15.3 (15.4)

[a]Theoretical values with (and without) BSSE corrections. [b]Values from Table 2. [c]Single point energies calculated at the indicated level using a 6-311+G(2d,2p) basis set and B3LYP/6-311+G(d,p) geometries and zero point energies. [d]Geometries optimized at cam-B3LYP level of theory consistent with calculations of Garand and co-workers.[25] [e]Mean absolute deviations from experimental BDEs. [f]Mean experimental uncertainty.

good agreement with those from both experiment and density functional methods, possibly suggesting an error inherent to the Möller–Plesset correlation energy correction for these systems. In the following discussion, BDEs obtained at the MP2(full) level will not be included.

For each complex size, BDEs calculated in the present study are given with and without BSSE corrections in Table 3, except no counterpoise corrections were calculated for the CCSD(T) approach. BSSE corrections for each complex size were relatively small for B3LYP, B3P86, M06, and cam-B3LYP levels (<5 kJ/mol), whereas corrections for cam-B3LYP/TZVP were larger, generally around 8 kJ/mol. These corrections improve the agreement with experimental BDEs for n = 4 and 1, and worsen the agreement for n = 2 and 3 by further underestimating the experimental values. Overall, BSSE corrections make very little difference in the mean absolute deviation (MAD) from experimental values for all levels of theory. All further comparisons between experimental and theoretical BDEs will be made with the BSSE corrected values, with the CCSD(T) results being a notable exception. Figure 4

dx.doi.org/10.1021/jp508962d | J. Phys. Chem. A 2014, 118, 10210–10222

shows the comparison of these theoretical BDE energies with experiment for $CuOH^+(H_2O)_n$ where n = 1−4.

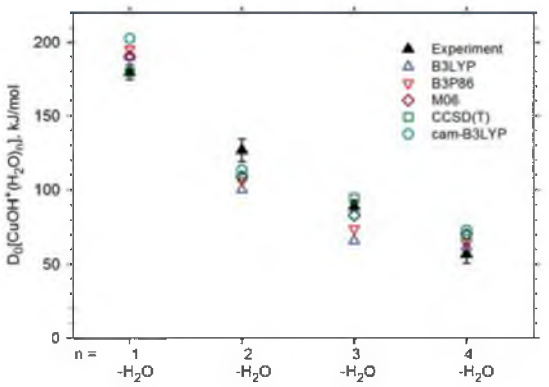

Figure 4. Comparison of experimental (solid symbols) and theoretical (open symbols) hydration enthalpies at 0 K for B3LYP, B3P86, M06, CCSD(T), and cam-B3LYP results (with BSSE corrections except for CCSD(T)) from Table 3.

The BDEs at the B3LYP, B3P86, M06, CCSD(T), and cam-B3LYP levels of theory maintain reasonable agreement among each other, with values agreeing within 9 and 11 kJ/mol for n = 4 and 2, respectively. For n = 3 and 1, variations of 11−25 and 11−23 kJ/mol, respectively, are found for CCSD(T) BDEs from BDEs calculated by a majority of the other levels of theory. In general, agreement with experiment is good, with theory overestimating BDEs for the n = 1 and 4 complexes, and underestimating them for n = 2 and, with the exception of CCSD(T), n = 3. Overall, theory predicts BDEs in reasonable agreement with experiment with mean absolute deviations (MADs) of 16.2 (B3LYP), 14.7 (B3P86), 12.0 (M06), 8.9 (CCSD(T)), and 14.7 (cam-B3LYP) kJ/mol. These differences are somewhat larger than the mean experimental uncertainty of 5.5 kJ/mol.

Calculated values of the HO-$Cu^+(H_2O)$ BDE can be found in Table 4. In accord with experimental results, all five levels of theory predict that the dissociation of $CuOH^+(H_2O)$ to form $CuOH^+$ + H_2O is higher in energy than the dissociation to form $Cu^+(H_2O)$ + OH. Experiment measures this difference as 5.7 ± 1.7 kJ/mol, whereas B3LYP, B3P86, M06, CCSD(T), and cam-B3LYP predict differences of 5.2, 3.0, 14.7, 36.2, and 23.0 kJ/mol, respectively. Clearly, CCSD(T) underestimates the HO-$Cu^+(H_2O)$ BDE badly.

Comparison to Literature Theoretical Values. Garand and co-workers calculated the theoretical bond energies for $CuOH^+(H_2O)_3$ dissociating to $CuOH^+(H_2O)_2$, $CuOH^+(H_2O)$, and $CuOH^+$ using a Coulomb attenuating method (cam) at the cam-B3LYP/TZVP level with no BSSE corrections.[25] These values are in excellent agreement with the experimental values for the $CuOH^+(H_2O)_3$ and $CuOH^+(H_2O)_2$ complexes measured here and slightly outside of the experimental uncertainty for $CuOH^+(H_2O)$, leading to a MAD of 14.0 kJ/mol. For the present study, we independently calculated BDEs for the $CuOH^+(H_2O)_n$ complexes, where n = 1−4, at the same level used by Garand and co-workers in order to obtain a value for the n = 4 complex and for loss of OH from $CuOH^+(H_2O)$. BDEs calculated here for water loss from the n = 1−3 complexes reproduce their values. The BDE at this level for the n = 4 complex with (and without) BSSE corrections is 76.0 (80.5) kJ/mol, which is less accurate than the other five levels of theory, being higher than the experimental value by >19 kJ/mol. The addition of this BDE to those calculated by Garand and co-workers yields a MAD from experiment of 15.3 (15.4) kJ/mol. To further evaluate the cam-B3LYP approach, as noted above, SPEs for cam-B3LYP were also calculated using the 6-311+G(2d,2p) basis set and the B3LYP/6-311+G(d,p) geometries. BDEs from those calculations yield a comparable MAD from experiment of 14.7 (14.6) kJ/mol and improve the agreement with the other levels of theory compared to cam-B3LYP/TZVP, Table 3. The differences are presumably mainly a result of the diffuse functions in the 6-311+G(2d,2p) basis set here.

Trends in the Bond Dissociation Energies. Previous work in this lab measured the dehydration energies for $Cu^+(H_2O)_n$ where n = 1−4.[22] Comparison of those values to the values determined in the present work can be seen in Figure

Table 4. Comparison of Experimental 0 K Bond Energies (kJ/mol) to Theoretical Values[a]

bond	expt	B3LYP[b]	B3P86[b]	M06[b]	CCSD(T)[b]	cam-B3LYP[b]	cam-B3LYP/TZVP[c]
			$Cu^+(H_2O)_{n-1}$-(H_2O)				
n = 4	54.4 ± 4.8[d]	59.7 (57.9)	60.2 (62.2)	58.9 (61.0)	(59.4)	61.8 (64.4)	68.9 (72.1)
3	56.9 ± 7.7[d]	61.8 (63.8)	64.5 (66.5)	62.3 (64.5)	(62.5)	66.6 (68.5)	72.9 (76.2)
2	169.8 ± 6.8[d]	158.8 (161.9)	163.0 (166.2)	156.8 (160.7)	(152.7)	162.4 (165.4)	175.2 (183.5)
1	157.3 ± 7.7[d]	161.7 (163.7)	163.9 (166.0)	156.2 (158.2)	(148.8)	177.3 (179.3)	173.8 (180.0)
MAD[e]	6.8[f]	6.4 (6.2)	6.7 (7.4)	6.0 (6.1)	(9.1)	11.1 (12.0)	13.1 (18.4)
			HO-$Cu^+(H_2O)_n$				
n = 4	165.2 ± 16.2[g]	136.8 (140.6)	152.3 (156.2)	146.7 (151.3)	(141.2)	147.5 (151.3)	139.3 (148.8)
3	162.7 ± 14.1[g]	132.1 (135.8)	146.8 (150.7)	137.4 (142.0)	(131.2)	139.1 (142.5)	131.3 (140.4)
2	130.3 ± 11.3[g]	126.4 (129.8)	135.8 (139.3)	119.6 (123.3)	(99.4)	124.4 (127.6)	118.1 (125.1)
1	173.7 ± 4.8[h]	184.8 (188.3)	192.1 (195.8)	170.8 (175.0)	(143.5)	176.1 (179.5)	180.1 (186.6)
0	151.5 ± 8.0[g]	158.1 (158.1)	162.6 (162.6)	142.8 (142.8)	(112.6)	155.9 (155.9)	155.7 (155.7)
MAD[e]	10.9[f]	16.1 (14.6)	12.8 (12.6)	13.2 (10.3)	(31.1)	10.8 (9.4)	16.0 (12.2)
overall MAD[e,i]	8.0[f,i]	13.2 (12.5)	11.5 (11.7)	10.6 (9.5)	(17.5)	12.1 (14.9)	14.9 (15.0)

[a]Theoretical values with (without) BSSE corrections. [b]Single point energies calculated at the indicated level using a 6-311+G(2d,2p) basis set and B3LYP/6-311+G(d,p) geometries and zero point energies. [c]Geometries optimized at cam-B3LYP/TZVP level of theory. [d]Values from Dalleska et al.[22] [e]Mean absolute deviations from experimental BDEs. [f]Mean experimental uncertainty. [g]Derived values from thermodynamic cycles, Figure 5. [h]Measured here. [i]Includes all values in this table and Table 3.

dx.doi.org/10.1021/jp508962d | J. Phys. Chem. A 2014, 118, 10210−10222

5. The BDEs for the $CuOH^+(H_2O)_n$ system consistently increase by 32−37 kJ/mol as n decreases until n = 1, at which

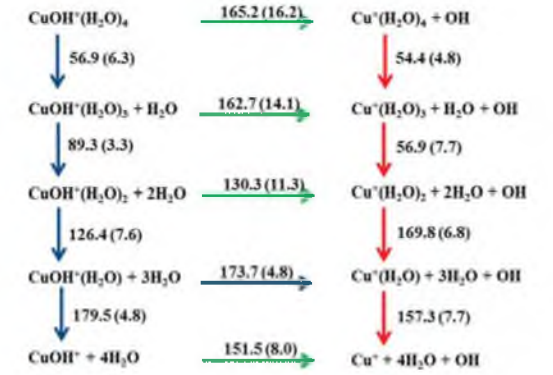

Figure 5. Comparison of present experimental results (blue arrows, left side) with those of Dalleska et al. (red arrows, right side, ref 22). Derived BDEs for the loss of OH lie in between (green arrows).

point formation of either $CuOH^+$ or $Cu^+(H_2O)$ requires ~50 kJ/mol more. By comparison, the energy required to remove sequential waters from $Cu^+(H_2O)_n$ is nearly the same for the n = 4 and 3 complexes and is much smaller than for n = 1 and 2, with n = 2 being larger than n = 1 by 12.5 kJ/mol.[22] The decrease in going from n = 1 to 2 and the jump in BDE between the n = 2 and 3 complexes for that system were determined to arise from the strong electronic effect associated with 4s−3dσ orbital hybridization.[79] Michl and co-workers[21,28] and Squires and co-workers[29] saw similar trends, and the former suggested that the large decrease in BDEs after n = 2 indicated that Cu^+ prefers a CN = 2. Clearly, this pattern of BDEs is not reflected in the $CuOH^+(H_2O)_n$ system. As discussed in our previous work,[26] this can be attributed to a change in the 3d orbital population. Cu^+ has a closed $3d^{10}$ configuration, which means that 4s−3dσ hybridization is used effectively to remove electron density from along the σ axis allowing stronger bonding, but only for the first two ligands. Thus, Cu^+ prefers CN = 2, as shown in Figure 1b. In contrast, the copper in $CuOH^+$ is largely $3d^9$ because the hydroxide acts as a strong electron withdrawer, effectively making the complex $Cu^{2+}OH^-$. This explains the preference for CN = 4 as the $3d^9$ configuration of Cu^{2+} prefers a square planar ligand coordination according to ligand field theory. For both systems, the energy required to remove the fourth water is the same within experimental uncertainty, consistent with a second shell water ligand, Figure 1.

It is interesting to note that the Cu^+−OH_2 BDE is smaller than the $CuOH^+$−OH_2 BDE; however, this is a comparison between CN = 1 and CN = 2 systems. Therefore, a fairer comparison may come from complexes having the same CN, i.e., loss of water from $Cu^+(H_2O)_2$, 169.8 ± 6.8 kJ/mol, and $CuOH^+(H_2O)$, 179.5 ± 4.8 kJ/mol. By either metric, the binding of the last water to the $CuOH^+(H_2O)_n$ system is stronger. This can be attributed to the $Cu^{2+}OH^-$ character of the $CuOH^+$ species, such that interactions of the copper center with electron donors like water are stronger than in the Cu^+ charge state.

Derived Thermochemistry of Copper Ion Hydration. Using the experimentally determined BDEs from both the $CuOH^+(H_2O)_n$ and $Cu^+(H_2O)_n$ systems, values for the loss of the OH ligand from $CuOH^+(H_2O)_n$, where n = 0 and 2−4, are derived, as shown in Figure 5. For the larger complexes, it is now evident that loss of the water ligand is thermodynamically preferred over loss of the OH ligand, explaining why the latter channel is not observed until the n = 1 complex. The derived BDE for dissociation of OH from $CuOH^+$ is 151.5 ± 8.0 kJ/mol, which can be compared with other CuX^+ complexes where X is an isovalent radical ligand, CH_3 and NH_2. Previous work in this lab found that the BDE of $CuCH_3^+$ is 111 ± 7 kJ/mol[80,81] and that for $CuNH_2^+$ it is 192 ± 13 kJ/mol.[81,82] In all three of these molecules, a covalent bond can be made between the radical ligand and the 4s electron of Cu^+. This requires promotion of an electron from the closed $3d^{10}$ ground state configuration to a $4s^13d^9$ configuration where the 4s electron is spin decoupled from the d electrons. For Cu^+, this promotion energy is 292 kJ/mol, the highest among all the first-row transition metal cations. This is consistent with all three CuX^+ BDEs being the lowest values determined across the periodic table for first-row transition metals.[81]

The $CuOH^+$ BDE of 151.5 ± 8.0 kJ/mol falls in between the values for $CuCH_3^+$ and $CuNH_2^+$, which contrasts with results for any other first-row transition metal.[81] In these systems, the BDEs of M^+−OH > M^+−NH_2 > M^+−CH_3 because the lone pairs of electrons on the OH and NH_2 ligands donate into empty or half-empty orbitals on the metal forming dative bonds. For early metals, which have empty 3d orbitals, the MOH^+ BDEs exceed MCH_3^+ BDEs by 253 ± 13 kJ/mol and MNH_2^+ BDEs exceed MCH_3^+ BDEs by 115 ± 16 kJ/mol. Thus, the dative bonds average 126 ± 19 kJ/mol for metal cations having two empty d orbitals (Sc−V). As one moves to the right in the periodic table, the d orbitals become occupied. For Mn−Co, which each have at least two singly occupied d orbitals, MOH^+ BDEs exceed MCH_3^+ BDEs by 120 ± 21 kJ/mol and MNH_2^+ BDEs exceed MCH_3^+ BDEs by 52 ± 19 kJ/mol. In each case, these enhancements are about half those of the early metals, consistent with donation into a singly occupied orbital instead of an empty one. On this basis, Cu^+ with a $4s^13d^9$ configuration (where the 4s electron is needed to form the covalent bond) has only one singly occupied d orbital, such that both $CuNH_2^+$ and $CuOH^+$ might be expected to exceed the $CuCH_3^+$ BDE by 57 ± 17 kJ/mol (the average dative bond strength for late metal cations), as each ligand can form only one-half-dative bond. Experimentally, the enhancements are 81 ± 15 and 40 ± 11 kJ/mol, respectively, both within experimental uncertainty of the predicted result, but on the high and low side, respectively. The OH BDE may be lowered in this case because the doubly occupied 3d orbital interacts repulsively with the second lone-pair orbital on oxygen. In addition, variations can occur as a result of the extent to which the $Cu^{2+}X^-$ configuration contributes to the molecule. Given the electron affinities of NH_2 and OH, 0.771[83] and 1.82767 eV,[84] respectively, the latter ligand will clearly induce more Cu^{2+} character. This potentially contracts the 3d orbitals and expands the heteroatom lone-pair orbitals such that overlap contributing to effective dative bonding is reduced.

Comparison of Literature and Derived Experimental Values with Theory. To provide a more comprehensive evaluation of the experimental and theoretical thermochemistry for copper hydration, BDEs for both $Cu^+(H_2O)_n$, n = 1−4, of Dalleska et al.,[22] and derived values of HO-$Cu^+(H_2O)_n$, n = 0−4, are compared to theoretical BDEs determined at the same levels used above. BDEs at all levels of theory, with

dx.doi.org/10.1021/jp508962d | J. Phys. Chem. A 2014, 118, 10210−10222

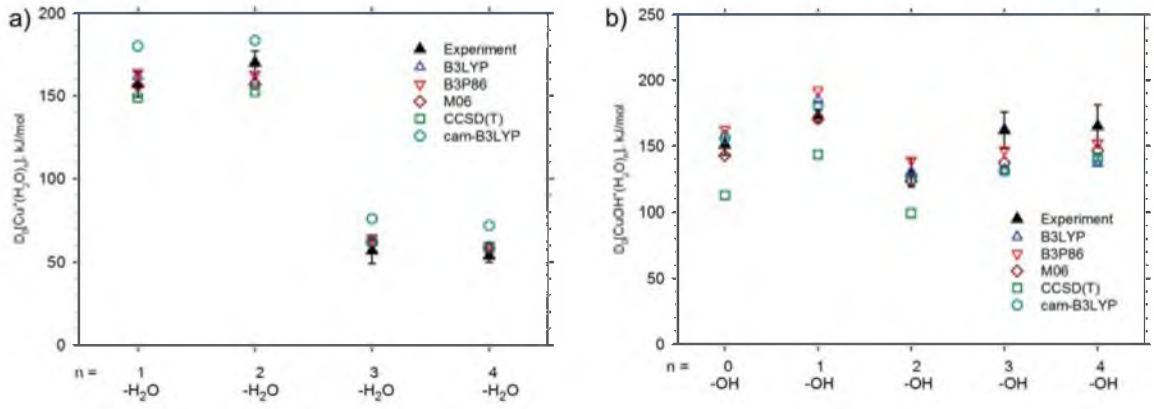

Figure 6. Comparison of experimental (solid symbols) and theoretical (open symbols) hydration enthalpies at 0 K for B3LYP, B3P86, M06, CCSD(T), and cam-B3LYP results (with BSSE corrections except for CCSD(T)) from Table 4 for (a) $Cu^+(H_2O)_n$ dissociating to lose H_2O and (b) $CuOH^+(H_2O)_n$ dissociating to lose OH.

Table 5. Conversion of 0 K Thresholds to 298 K Enthalpies and Free Energies (kJ/mol)[a]

bond	ΔH_0[b]	$\Delta H_{298} - \Delta H_0$[c]	ΔH_{298}	$T\Delta S_{298}$[c]	ΔG_{298}
		$CuOH^+(H_2O)_{n-1}$-(H_2O)			
n = 4	56.9 (6.3)	4.6 (0.5)	61.5 (6.3)	44.0 (1.0)	17.5 (6.4)
3	89.3 (3.3)	3.1 (0.5)	92.4 (3.3)	42.3 (1.2)	50.1 (3.6)
2	126.4 (7.6)	2.5 (0.5)	128.8 (7.6)	35.0 (1.2)	93.7 (7.8)
1	179.5 (4.8)	3.3 (0.5)	182.7 (4.8)	39.0 (1.3)	143.7 (5.0)
		$Cu^+(H_2O)_{n-1}$-(H_2O)			
n = 4	54.4 (4.8)	2.0 (0.3)	56.4 (4.8)	35.3 (1.2)	21.1 (4.9)
3	56.9 (7.7)	2.5 (0.4)	59.4 (7.7)	32.6 (1.1)	26.7 (7.8)
2	169.8 (6.8)	0.7 (0.4)	170.5 (6.8)	33.5 (0.5)	137.0 (6.9)
1	157.3 (7.7)	4.1 (0.3)	161.4 (7.7)	28.9 (0.5)	132.4 (7.7)
		$HO\text{-}Cu^+(H_2O)_n$			
n = 4	165.2 (16.2)	9.3 (0.6)	174.5 (16.2)	61.0 (0.7)	113.5 (16.2)
3	162.7 (14.1)	5.5 (0.6)	168.1 (14.1)	47.1 (0.9)	121.0 (14.1)
2	130.3 (11.3)	4.9 (0.5)	135.1 (11.3)	39.2 (0.8)	96.0 (11.3)
1	173.7 (4.8)	3.1 (0.4)	176.8 (4.8)	35.9 (0.9)	140.8 (4.8)
0	151.5 (8.0)	3.9 (0.2)	155.4 (8.0)	24.1 (0.3)	131.3 (8.0)

[a]Uncertainties in parentheses. [b]Experimental values from this work (Tables 3 and 4). [c]Values are calculated from the vibrational frequencies and rotational constants calculated at the B3LYP/6-311+G(d,p) level. Uncertainties are found by scaling the frequencies up and down by 10%.

(and without) BSSE corrections, for all these systems are given in Table 4 with structures found in Figure 1b.

Geometries for the $Cu^+(H_2O)_n$ systems, calculated at the B3LYP/6-311+G(d,p) level, show Cu−O bond lengths of 2.05 Å for n = 1 and 1.92 Å for n = 2 with an OCuO bond angle of 180°. Addition of the third and fourth water ligands occurs preferentially in the second solvent shell, such that the Cu−O bond distances are now 3.99 and 4.01 Å, respectively. Oxygen atoms in the n = 3 isomer are coplanar with the Cu center, whereas the fourth water for n = 4 is ~120° out of this plane. These results agree with several previous theoretical studies.[23,79,85,86] For the $Cu^+(H_2O)_n$ system, Figure 6a shows that experiment and theory agree very well with MADs of 6.4 (B3LYP), 6.7 (B3P86), 6.0 (M06), 9.1 (CCSD(T)), and 11.1 kJ/mol (cam-B3LYP). These values are similar to the average experimental error of 6.8 kJ/mol. In all cases, BDEs calculated at the cam-B3LYP/TZVP level are much higher than experiment, with a MAD of 13.1 kJ/mol. At n = 3 and 4, all levels of theory are on the high side of the experimental results, whereas at n = 2, all levels of theory are on the low side of the experimental results except for cam-B3LYP/TZVP. For n = 1, the largest variance in theoretical BDEs results in values both slightly higher and slightly lower than the experimental value, yet within experimental uncertainty except for the cam-B3LYP approaches.

Likewise, theoretical values for the dissociation of OH from $CuOH^+(H_2O)_n$ compare well with the derived experimental values, Table 4 and Figure 6b. For n = 3 and 4, all levels of theory are on the low side of the derived values, whereas at n = 1 and 2, the agreement is quite good and is generally within the uncertainty of the derived values except for the CCSD(T) values. MADs for the OH BDEs of 16.1 (B3LYP), 12.8 (B3P86), 13.2 (M06), 31.1 (CCSD(T)), and 10.8 kJ/mol (cam-B3LYP) are generally comparable to the 10.9 kJ/mol average experimental uncertainty for the derived values. For consistency, we report these MADs with BSSE corrections; however, because theory tends to underestimate these derived values, Figure 6b, BDEs without such corrections actually improve agreement slightly.

Overall MADs for the $CuOH^+(H_2O)_{n-1}$-(H_2O), $Cu^+(H_2O)_{n-1}$-(H_2O), and $HO\text{-}Cu^+(H_2O)_n$ BDEs for all levels of theory are included in Table 4. It can be seen that most

dx.doi.org/10.1021/jp508962d | J. Phys. Chem. A 2014, 118, 10210−10222

levels of theory are comparable with MADs from experiment of 10−15 kJ/mol. That for CCSD(T) is larger primarily because of the HO-$Cu^+(H_2O)_n$ discrepancies.

Conversion from 0 to 298 K Thermodynamics. A rigid rotor/harmonic oscillator approximation was applied to convert the 0 K bond energies into 298 K enthalpies. This was achieved using the theoretical vibrational frequencies scaled by 0.989 and rotational constants of the complexes. The uncertainties in these conversions were obtained by scaling the vibrational frequencies up and down by 10%. These conversion factors were used to determine ΔH_{298} and ΔG_{298} values listed in Table 5. Note that this approximation may not be suitable for all cases because of the inaccuracy of low-frequency torsional motions. For the $CuOH^+(H_2O)_{n-1}$-(H_2O) systems, ΔH_0 and ΔG_{298} values increase with decreasing complex size. The decrease in entropy from $n = 4$ to $n = 2$ can be attributed to the hydrogen bonding between adjacent water ligands, which play a smaller role as the complex size decreases and ligand spacing increases. For the $n = 1$ complex, the higher cross section for loss of H_2O from the $n = 1$ reactant above 3 eV indicates that it is entropically favored compared to loss of OH. This result is reproduced quantitatively in Table 5 by the larger $T\Delta S_{298}$ value of the $n = 1 \rightarrow CuOH^+ + H_2O$ dissociation. For the $Cu^+(H_2O)_{n-1}$-(H_2O) systems, ΔG_{298} values track with ΔH_0; i.e., they are similar for $n = 3$ and 4 and much larger for $n = 1$ and 2 with $n = 2$ slightly higher in energy. The $T\Delta S_{298}$ values for this system are relatively unchanged across all complex sizes indicating that simple A-type hydrogen bonding seen in the $n = 3$ and 4 complexes does very little to change the entropy. Finally, for the HO-$Cu^+(H_2O)_n$ systems, the $T\Delta S_{298}$ values have the largest range of all systems investigated and, like $CuOH^+(H_2O)_{n-1}$-(H_2O), decrease with complex size.

As mentioned above, water loss proceeds over a loose TS. A metric for the looseness of a TS is the entropy of activation at 1000 K, as shown in Table 2 for the $CuOH^+(H_2O)_{n-1}$-(H_2O) systems. For all complexes examined, this value is positive and relatively large, which is consistent with a loose TS. Overall, the trends in the entropies of activation track with the dissociation entropies, decreasing with complex size and larger for the $CuOH^+$ product than for the $Cu^+(H_2O)$ product. Across all systems and complex sizes, $T\Delta S_{298}$ values for OH loss are larger than those for H_2O loss except at $n = 1$ where loss of H_2O from $CuOH^+(H_2O)$ is larger. For the larger complexes, this result can probably be attributed to the strong polarizing interaction of the OH ligand in the $CuOH^+(H_2O)_n$ complexes, which constrains the geometry of $CuOH^+(H_2O)_n$ more than $Cu^+(H_2O)_n$.

CONCLUSION

Energy-resolved threshold collision-induced dissociation with Xe is performed on $CuOH^+(H_2O)_n$ where $n = 1$−4. The primary dissociation pathway of the $n = 2$−4 reactants is loss of a single water molecule followed by the sequential loss of additional water molecules at higher collision energies. Interestingly, dissociation of the OH ligand is energetically more favorable than loss of the H_2O at $n = 1$, although loss of the H_2O is entropically favored at higher energies. Statistical analysis of the TCID data is used to obtain 0 K bond energies for all dissociation pathways. These energies are converted to obtain thermodynamic values at 298 K using a rigid rotor/harmonic oscillator approximation. Dissociation energies increase by similar amounts with a decrease in complex size for $n = 2$−4, whereas the $n = 1$ complex requires ~40 kJ/mol more energy for loss of either ligand. In addition, by combining the present results with literature data for $Cu^+(H_2O)_n$ where $n = 1$−4, the hydroxide BDEs in all four $CuOH^+(H_2O)_n$ complexes where $n = 0$, 2−4, are derived. The BDE for $CuOH^+$ is compared to other metal hydroxide cation BDEs and found to align nicely with expected periodic trends. Experimental BDEs for the $CuOH^+(H_2O)_n$ complexes are measured here for the first time and compare favorably to BDEs calculated at the B3LYP, B3P86, M06, and CCSD(T) levels of theory. MP2(full) calculations show anomalous results for these small complexes. Similarly good agreement is also found for HO-$Cu^+(H_2O)_n$ and $Cu^+(H_2O)_n$ complexes although CCSD(T) values for the hydroxide bonds are systematically low.

ASSOCIATED CONTENT

Supporting Information

Efforts to resolve anomalous MP2(full) results including BDEs calculated at the MP2(full), MP2, MP3, MP4DQ, CCSD, and CCSD(T) levels of theory. This material is available free of charge via the Internet at http://pubs.acs.org.

AUTHOR INFORMATION

Corresponding Author

*E-mail: armentrout@chem.utah.edu.

Notes

The authors declare no competing financial interest.

ACKNOWLEDGMENTS

This work is supported by the National Science Foundation, Grant CHE-1359769. In addition, we thank the Center for High Performance Computing (CHPC) at the University of Utah for the generous allocation of computing time.

REFERENCES

(1) Thiele, D. J. Metal-Regulated Transcription in Eukaryotes. *Nucleic Acids Res.* **1992**, *20*, 1183−1191.

(2) Zhou, P.; Thiele, D. J. Isolation of a Metal-Activated Transcription Factor Gene from Candida Glabrata by Complementation in Saccharomyces Cerevisiae. *Proc. Natl. Acad. Sci. U.S.A.* **1991**, *88*, 6112−6116.

(3) Fernandes, J. C.; Henriques, F. S. Biochemical, Physiological, and Structural Effects of Excess Copper in Plants. *Bot. Rev.* **1991**, *57*, 246−273.

(4) Mallick, N.; Mohn, F. H. Use of Chlorophyll Fluorescence in Metal-Stress Research: A Case Study with the Green Microalga Scenedesmus. *Ecotoxicol. Environ. Saf.* **2003**, *55*, 64−69.

(5) Perales-Vela, H. V.; González-Moreno, S.; Montes-Horcasitas, C.; Cañizares-Villanueva, R. O. Growth, Photosynthetic and Respiratory Responses to Sub-Lethal Copper Concentrations in Scenedesmus Incrassatulus (Chlorophyceae). *Chemosphere* **2007**, *67*, 2274−2281.

(6) Zeng, L.; Miller, E. W.; Pralle, A.; Isacoff, E. Y.; Chang, C. J. A Selective Turn-on Fluorescent Sensor for Imaging Copper in Living Cells. *J. Am. Chem. Soc.* **2006**, *128*, 10−11.

(7) Frank, P.; Benfatto, M.; Szilagyi, R. K.; D'Angelo, P.; Longa, S. D.; Hodgson, K. O. The Solution Structure of $[Cu(aq)]^{2+}$ and Its Implications for Rack-Induced Bonding in Blue Copper Protein Active Sites. *Inorg. Chem.* **2005**, *44*, 1922−1933.

(8) Barnham, K. J.; Masters, C. L.; Bush, A. I. Neurodegenerative Diseases and Oxidative Stress. *Nat. Rev. Drug Discovery* **2004**, *3*, 205−214.

(9) Waggoner, D. J.; Bartnikas, T. B.; Gitlin, J. D. The Role of Copper in Neurodegenerative Disease. *Neurobiol. Dis.* **1999**, *6*, 221−230.

(10) Turnlund, J. R. Copper. In *Modern Nutrition in Health and Disease*; Shils, M. E., Olson, J. A., Shike, M., Ross, A. C., Eds.; Williams and Wilkins: Baltimore, MD, 1999.
(11) Uauy, R.; Olivares, M.; Gonzalez, M. Essentiality of Copper in Humans. *Am. J. Clin. Nutr.* **1998**, *67*, 952S−959S.
(12) Andrade, L. R.; Farina, M.; Amado Filho, G. M. Effects of Copper on Enteromorpha Flexuosa (Chlorophyta) in Vitro. *Ecotoxicol. Environ. Saf.* **2004**, *58*, 117−125.
(13) Ma, M.; Zhu, W.; Wang, Z.; Witkamp, G. J. Accumulation, Assimilation and Growth Inhibition of Copper on Freshwater Alga (Scenedesmus Subspicatus 86.81 Sag) in the Presence of Edta and Fulvic Acid. *Aquat. Toxicol.* **2003**, *63*, 221−228.
(14) Winge, D. R.; Mehra, R. K. Host Defenses against Copper Toxicity. *Int. Rev. Exp. Pathol.* **1990**, *31*, 47−83.
(15) Panou-Filotheou, H.; Bosabalidis, A. M.; Karataglis, S. Effects of Copper Toxicity on Leaves of Oregano (Origanum Vulgare Subsp. Hirtum). *Ann. Bot.* **2001**, *88*, 207−214.
(16) Gaetke, L.; Chow, M.; Kuang, C. Copper Toxicity, Oxidative Stress, and Antioxidant Nutrients. *Toxicology* **2003**, *189*, 147−163.
(17) Stone, J. A.; Vukomanovic, D. Collisional Dissociation Studies of $Cu^{2+}(H_2O)_n$ Using Electrospray Ionization Mass Spectrometry. *Int. J. Mass Spectrom.* **1999**, *185*−*187*, 227−229.
(18) Shvartsburg, A. A.; Siu, K. W. M. Is There a Minimum Size for Aqueous Doubly Charged Metal Cations? *J. Am. Chem. Soc.* **2001**, *123*, 10071−10075.
(19) O'Brien, J. T.; Williams, E. R. Hydration of Gaseous Copper Dications Probed by IR Action Spectroscopy. *J. Phys. Chem. A* **2008**, *112*, 5893−5901.
(20) Holland, P. M.; Castleman, A. W. Gas-Phase Complexes of Cu^+ and Ag^+ Via Thermionic Emission Sources. *J. Am. Chem. Soc.* **1980**, *102*, 6174−6175.
(21) Magnera, T. F.; David, D. E.; Stulik, D.; Orth, R. G.; Jonkman, H. T.; Michl, J. Production of Hydrated Metal Ions by Fast Ion or Atom Beam Sputtering. Collision-Induced Dissociation and Successive Hydration Energies of Gaseous Cu^+ with 1−4 Water Molecules. *J. Am. Chem. Soc.* **1989**, *111*, 5036−5043.
(22) Dalleska, N. F.; Honma, K.; Sunderlin, L. S.; Armentrout, P. B. Solvation of Transition Metal Ions by Water. Sequential Binding Energies of $M^+(H_2O)_x$ (x = 1 - 4) for M = Ti-Cu Determined by Collision-Induced Dissociation. *J. Am. Chem. Soc.* **1994**, *116*, 3519−3528.
(23) Iino, T.; Ohashi, K.; Mune, Y.; Inokuchi, Y.; Judai, K.; Nishi, N.; Sekiya, H. Infrared Photodissociation Spectra and Solvation Structures of $Cu^+(H_2O)_n$ (n = 1−4). *Chem. Phys. Lett.* **2006**, *427*, 24−28.
(24) Bryantsev, V. S.; Diallo, M. S.; Goddard, W. A. Computational Study of Copper(II) Complexation and Hydrolysis in Aqueous Solutions Using Mixed Cluster/Continuum Models. *J. Phys. Chem. A* **2009**, *113*, 9559−9567.
(25) Marsh, B. M.; Zhou, J.; Garand, E. Vibrational Spectroscopy of Small Hydrated $CuOH^+$ Clusters. *J. Phys. Chem. A* **2014**, *118*, 2063−2071.
(26) Sweeney, A. F.; O'Brien, J. T.; Williams, E. R.; Armentrout, P. B. Structural Elucidation of Hydrated $CuOH^+$ Complexes Using IR Action Spectroscopy and Theoretical Modeling. *Int. J. Mass Spectrom.* **2014**, DOI: 10.1016/j.ijms.2014.08.037, in press.
(27) Klamt, A.; Schueuermann, G. Cosmo: A New Approach to Dielectric Screening in Solvents with Explicit Expressions for the Screening Energy and Its Gradient. *J. Chem. Soc., Perkin Trans. 2* **1993**, 799−805.
(28) Magnera, T. F.; David, D. E.; Michl, J. Gas-Phase Water and Hydroxyl Binding Energies for Monopositive First-Row Transition Metal Ions. *J. Am. Chem. Soc.* **1989**, *111*, 4100−4101.
(29) Marinelli, P. J.; Squires, R. R. Sequential Solvation of Atomic Transition-Metal Ions. The Second Solvent Molecule Can Bind More Strongly Than the First. *J. Am. Chem. Soc.* **1989**, *111*, 4101−4103.
(30) Kim, T.; Tolmachev, A. V.; Harkewicz, R.; Prior, D. C.; Anderson, G.; Udseth, H. R.; Smith, R. D. Design and Implementation of a New Electrodynamic Ion Funnel. *Anal. Chem.* **2000**, *72*, 2247−2255.
(31) Shaffer, S. A.; Prior, D. C.; Anderson, G. A.; Udseth, H. R.; Smith, R. D. An Ion Funnel Interface for Improved Ion Focusing and Sensitivity Using Electrospray Ionization Mass Spectrometry. *Anal. Chem.* **1998**, *70*, 4111−4119.
(32) Shaffer, S. A.; Tolmachev, A.; Prior, D. C.; Anderson, G. A.; Udseth, H. R.; Smith, R. D. Characterization of an Improved Electrodynamic Ion Funnel Interface for Electrospray Ionization Mass Spectrometry. *Anal. Chem.* **1999**, *71*, 2957−2964.
(33) Moision, R. M.; Armentrout, P. B. An Electrospray Source for Thermochemical Investigation with the Guided Ion Beam Mass Spectrometer. *J. Am. Soc. Mass Spectrom.* **2007**, *18*, 1124−1134.
(34) Heaton, A. L.; Moision, R. M.; Armentrout, P. B. Experimental and Theoretical Studies of Sodium Cation Interactions with the Acidic Amino Acids and Their Amide Derivatives. *J. Phys. Chem. A* **2008**, *112*, 3319−3327.
(35) Heaton, A. L.; Ye, S. J.; Armentrout, P. B. Experimental and Theoretical Studies of Sodium Cation Complexes of the Deamidation and Dehydration Products of Asparagine, Glutamine, Aspartic Acid, and Glutamic Acid. *J. Phys. Chem. A* **2008**, *112*, 3328−3338.
(36) Carl, D. R.; Moision, R. M.; Armentrout, P. B. In-Source Fragmentation Technique for the Production of Thermalized Ions. *J. Am. Soc. Mass Spectrom.* **2009**, *20*, 2312−2317.
(37) Carl, D. R.; Moision, R. M.; Armentrout, P. B. Binding Energies for the Inner Hydration Shells of Ca^{2+}: An Experimental and Theoretical Investigation of $Ca^{2+}(H_2O)_x$ Complexes (x = 5 − 9). *Int. J. Mass Spectrom.* **2007**, *265*, 308−325.
(38) Cooper, T. E.; Armentrout, P. B. Threshold Collision-Induced Dissociation of Hydrated Cadmium (II): Experimental and Theoretical Investigation of the Binding Energies for $Cd^{2+}(H_2O)_n$ Complexes (n = 4 − 11). *Chem. Phys. Lett.* **2010**, *486*, 1−6.
(39) Cooper, T. E.; Armentrout, P. B. Sequential Bond Energies and Barrier Heights for the Water Loss and Charge Separation Dissociation Pathways of $Cd^{2+}(H_2O)_n$, n = 3−11. *J. Chem. Phys.* **2011**, *134*, 114308.
(40) Armentrout, P. B.; Clark, A. A. The Simplest b_2^+ Ion: Determining Its Structure from Its Energetics by a Direct Comparison of the Threshold Collision-Induced Dissociation of Protonated Oxazolone and Diketopiperazine. *Int. J. Mass Spectrom.* **2012**, *316*-*318*, 182−191.
(41) Ervin, K. M.; Armentrout, P. B. Translational Energy Dependence of $Ar^+ + XY \rightarrow ArX^+ + Y$ (XY = H_2, D_2, HD) from Thermal to 30 Ev C.M. *J. Chem. Phys.* **1985**, *83*, 166−189.
(42) Muntean, F.; Armentrout, P. B. Guided Ion Beam Study of Collision-Induced Dissociation Dynamics: Integral and Differental Cross Sections. *J. Chem. Phys.* **2001**, *115*, 1213−1228.
(43) Teloy, E.; Gerlich, D. Integral Cross Sections for Ion−Molecule Reactions. 1. The Guided Beam Technique. *Chem. Phys.* **1974**, *4*, 417−427.
(44) Aristov, N.; Armentrout, P. B. Collision-Induced Dissociation of Vanadium Monoxide Ion. *J. Phys. Chem.* **1986**, *90*, 5135−5140.
(45) Daly, N. R. Scintillation Type Mass Spectrometer Ion Detector. *Rev. Sci. Instrum.* **1960**, *31*, 264−267.
(46) Beyer, T. S.; Swinehart, D. F. Number of Multiply-Restricted Partitions. *Commun. ACM* **1973**, *16*, 379.
(47) Stein, S. E.; Rabinovich, B. S. On the Use of Exact State Counting Methods in RRKM Rate Calculations. *Chem. Phys. Lett.* **1977**, *49*, 183−188.
(48) Stein, S. E.; Rabinovitch, B. S. Accurate Evaluation of Internal Energy Level Sums and Densities Including Anharmonic Oscillators and Hindered Rotors. *J. Chem. Phys.* **1973**, *58*, 2438−2445.
(49) Gilbert, R. G.; Smith, S. C. *Theory of Unimolecular and Recombination Reactions*; Blackwell Scientific: London, 1990.
(50) Holbrook, K. A.; Pilling, M. J.; Robertson, S. H. *Unimolecular Reactions*, 2nd ed.; Wiley: New York, 1996.
(51) Truhlar, D. G.; Garrett, B. C.; Klippenstein, S. J. Current Status of Transition-State Theory. *J. Phys. Chem.* **1996**, *100*, 12771−12800.
(52) Rodgers, M. T.; Ervin, K. M.; Armentrout, P. B. Statistical Modeling of Collision-Induced Dissociation Thresholds. *J. Chem. Phys.* **1997**, *106*, 4499−4508.

(53) Rodgers, M. T.; Armentrout, P. B. Statistical Modeling of Competitive Threshold Collision-Induced Dissociation. *J. Chem. Phys.* **1998**, *109*, 1787−1800.
(54) Armentrout, P. B.; Simons, J. Understanding Heterolytic Bond Cleavage. *J. Am. Chem. Soc.* **1992**, *114*, 8627−8633.
(55) Armentrout, P. B.; Heaton, A. L.; Ye, S. J. Thermodynamics and Mechanisms for Decomposition of Protonated Glycine and Its Protonated Dimer. *J. Phys. Chem. A* **2011**, *115*, 11144−11155.
(56) Muntean, F.; Armentrout, P. B. Modeling Kinetic Shifts for Tight Transition States in Threshold Collision-Induced Dissociation. Case Study: Phenol Cation. *J. Phys. Chem. B* **2002**, *106*, 8117−8124.
(57) Muntean, F.; Heumann, L.; Armentrout, P. B. Modeling Kinetic Shifts in Threshold Collision-Induced Dissociation. Case Study: Dichlorobenzene Cation Dissociation. *J. Chem. Phys.* **2002**, *116*, 5593−5602.
(58) Muntean, F.; Armentrout, P. B. Modeling Kinetic Shifts and Competition in Threshold Collision-Induced Dissociation. Case Study: *N*-Butylbenzene Cation Dissociation. *J. Phys. Chem. A* **2003**, *107*, 7413−7422.
(59) Narancic, S.; Bach, A.; Chen, P. Simple Fitting of Energy-Resolved Reactive Cross Sections in Threshold Collision-Induced Dissociation (T-CID) Experiments. *J. Phys. Chem. A* **2007**, *111*, 7006−7013.
(60) Jia, B.; Angel, L. A.; Ervin, K. M. Threshold Collision-Induced Dissociation of Hydrogen-Bonded Dimers of Carboxylic Acids. *J. Phys. Chem. A* **2008**, *112*, 1773−1782.
(61) Armentrout, P. B. Statistical Modeling of Sequential Collision-Induced Dissociation. *J. Chem. Phys.* **2007**, *126*, 234302.
(62) Bauschlicher, C. W., Jr.; Maitre, P. J. Structure of $Co(H_2)_n^+$ Clusters, for n = 1-6. *J. Phys. Chem.* **1995**, *99*, 3444−3447.
(63) Boys, S. F.; Bernardi, R. The Calculation of Small Molecular Interactions by the Differences of Separate Total Energies. Some Procedures with Reduced Errors. *Mol. Phys.* **1970**, *19*, 553−566.
(64) van Duijneveldt, F. B.; van Duijneveldt-van de Rijdt, J. G. C. M.; van Lenthe, J. H. State of the Art in Counterpoise Theory. *Chem. Rev.* **1994**, *94*, 1873−1885.
(65) Becke, A. D. Density-Functional Exchange Energy Approximation with Correct Asymptotic Behavior. *Phys. Rev. A* **1988**, *38*, 3098−3100.
(66) Lee, C.; Yang, W.; Parr, R. G. Development of the Colle-Salvetti Correlation-Energy Formula into a Functional of the Electron Density. *Phys. Rev. B* **1988**, *37*, 785−789.
(67) Yanai, T.; Tew, D. P.; Handy, N. C. A New Hybrid Exchange−Correlation Functional Using the Coulomb-Attenuating Method (Cam-B3LYP). *Chem. Phys. Lett.* **2004**, *393*, 51−57.
(68) Perdew, J. P. Density-Functional Approximation for the Correlation Energy of the Inhomogeneous Electron Gas. *Phys. Rev. B* **1986**, *33*, 8822−8824.
(69) Zhao, Y.; Truhlar, D. G. The M06 Suite of Density Functionals for Main Group Thermochemistry, Thermochemical Kinetics, Noncovalent Interactions, Excited States, and Transition Elements: Two New Functionals and Systematic Testing of Four M06-Class Functionals and 12 Other Functionals. *Theor. Chem. Acc.* **2008**, *120*, 215−241.
(70) Möller, C.; Plesset, M. S. Note on an Approximation Treatment for Many-Electron Systems. *Phys. Rev.* **1934**, *46*, 618−622.
(71) Peschke, M.; Blades, A. T.; Kebarle, P. Binding Energies for Doubly-Charged Ions M^{2+} = Mg^{2+}, Ca^{2+} and Zn^{2+} with the Ligands L = H_2O, Acetone and N-Methylacetamide in Complexes ML_n^{2+} for *n* = 1 - 7 from Gas Phase Equilibra Determinations and Theoretical Calculations. *J. Am. Chem. Soc.* **2000**, *122*, 10440−10449.
(72) Pavlov, M.; Siegbahn, P. E. M.; Sandstrom, M. Hydration of Beryllium, Magnesium, Calcium, and Zinc Ions Using Density Functional Theory. *J. Phys. Chem. A* **1998**, *102*, 219−228.
(73) Cooper, T. E.; Carl, D. R.; Armentrout, P. B. Hydration Energies of Zinc (II): Threshold Collision-Induced Dissociation Experiments and Theoretical Studies. *J. Phys. Chem. A* **2009**, *113*, 13727−13741.
(74) Sannigrahi, A. B.; Nandi, P. K. S.; P, v. R. Ab Initio Study of Cation-Dipole Interactions. Proton, Lithium, and Sodium Affinities of Hydrogen and Alkali Halides and Natural Orbital Study of Bonding. *J. Am. Chem. Soc.* **1994**, *116*, 7225−7232.
(75) Petrie, S. Gaussian-2 Theory, Na^+, and Hf: A Cautionary Tale. *Chem. Phys. Lett.* **1998**, *283*, 131−138.
(76) Hoyau, S.; Norrman, K.; McMahon, T. B.; Ohanessian, G. A Quantitative Basis for a Scale of Na^+ Affinities of Organic and Small Biological Molecules in the Gas Phase. *J. Am. Chem. Soc.* **1999**, *121*, 8864−8875.
(77) Bauschlicher, C. W.; Partridge, H. A Modification of the Gaussian-2 Approach Using Density Functional Theory. *J. Chem. Phys.* **1995**, *103*, 1788−1791.
(78) Frisch, M. J.; Trucks, G. W.; Schlegel, H. B.; Scuseria, G. E.; Robb, M. A.; Cheeseman, J. R.; Scalmani, G.; Barone, V.; Mennucci, B.; Petersson, G. A.; et al. *Gaussian 09, Revision A.02*; Gaussian Inc.: Pittsburgh, PA, 2009.
(79) Bauschlicher, J. C. W.; Langhoff, S. R.; Partridge, H. The Binding Energies of Cu^+-$(H_2O)_n$ and Cu^+-$(NH_3)_n$ (n = 1−4). *J. Chem. Phys.* **1991**, *94*, 2068−2072.
(80) Georgiadis, R.; Fisher, E. R.; Armentrout, P. B. Neutral and Ionic Metal Hydrogen and Metal Carbon Bond Energies: Reactions of Co^+, Ni^+, and Cu^+ with Ethane, Propane, Methylpropane, and Dimethylpropane. *J. Am. Chem. Soc.* **1989**, *111*, 4251−4262.
(81) Armentrout, P. B.; Kickel, B. L. Gas-Phase Thermochemistry of Transition Metal Ligand Systems: Reassessment of Values and Periodic Trends. In *Organometallic Ion Chemistry*; Freiser, B. S., Ed.; Kluwer: Dordrecht, 1996; pp 1−45.
(82) Clemmer, D. E.; Armentrout, P. B. Ammonia Activation by Co^+, Ni^+, and Cu^+. M^+-NH_2 Bond Energies and M^+–NH_3 Adduct Lifetimes. *J. Phys. Chem.* **1991**, *95*, 3084−3090.
(83) Wickham-Jones, C. T.; Ervin, K. M.; Ellision, G. B.; Lineberger, W. C. NH_2 Electron Affinity. *J. Chem. Phys.* **1989**, *91*, 2762−2763.
(84) Smith, J. R.; Kim, J. B.; Lineberger, W. C. High-Resolution Threshold Photodetachment Spectroscopy of OH^-. *Phys. Rev. A* **1997**, *55*, 2036−2043.
(85) Ni, B.; Kramer, J. R.; Werstiuk, N. H. Density Functional Theory and Qt Atoms-in-Molecules Study on the Hydration of Cu(I) and Ag(I) Ions and Sulfides. *J. Phys. Chem. A* **2005**, *109*, 1548−1558.
(86) Rosi, M.; Bauschlicher, C. W., Jr. The Binding Energies of One and Two Water Molecules to the First Transition Row Metal Positive Ions. *J. Chem. Phys.* **1989**, *90*, 7264−7272.

CHAPTER 6

KINETIC ENERGY RELEASE DISTRIBUTIONS WITH A GUIDED ION BEAM TANDEM MASS SPECTROMETER

6.1 Introduction

The use of kinetic energy release distributions (KERDs) to probe the potential energy surface of unimolecular reactions is a practice with roots that trace back to the early '30s.[1] It was not until the early '70s that the modern KERD experiments came about in the form of metastable ion measurements using double-focusing mass spectrometers.[2, 3] Traditionally, KERD studies are conducted using photoionization[2, 4], photoion-photoelectron co-incidence spectroscopy (PIPECO)[3, 5, 6], or collision-induced dissociation (CID)[7, 8, 9] techniques with product ion measurements performed by either electrostatic analysis[10] or time of flight (TOF)[7]. Comparisons of these techniques with each other for analogous KERDs have helped outline the principles of collision dynamics[8, 11, 12, 13] and have greatly improved our understanding of unimolecular decomposition.

The development of the electrospray ionization source (ESI)[14] has allowed the study of a much wider breadth of systems by mass spectrometry than what was possible in the early days of KERD measurements. Despite this development, most KERD studies have only investigated diatomic and small polyatomic ions. Large polyatomic systems are, however, routinely studied with ESI on our guided ion beam tandem mass

spectrometer (GIBMS)[15], which has proven capable of obtaining accurate thermochemistry for a variety of systems,[16, 17, 18, 19, 20] although this technique has generally been employed to measure cross-sections rather than KERDs. The excellent accuracy of the data obtained from these cross-section measurements has prompted the use of the ESI-GIBMS to measure KERDs. An extensive search of the literature reveals that this marks the first attempt to quantitatively measure the KERDs using GIBMS techniques. Similar studies include an investigation by Stace et al. that measured the experimental peak-profiles of small-chain alcohols using a crossed-beam apparatus, although the analysis was largely qualitative.[8] A different study by Garcia et al. utilized electrostatic analysis to measure the KERD of C^+ and O^+ resulting from CID of CO^+ with He.[21] Comparison of these distributions with theory was carried out in the absence of statistical models that are necessary for larger systems and as such has little overlap with the types of examinations performed here.

The systems examined in the present work are particularly challenging because of the complexity of the models required to analyze them. The methods for modeling KERDs are as old and diverse as the experiments themselves. Most unimolecular models rely on a set of now commonplace statistical assumptions: that the reactant molecule passes through a transition state that represents a maximum in the reaction coordinate, and that the distribution of energy to the quantum states of that transition state is random, such that energy is partitioned statistically. Commonly used statistical approaches for modeling KERDs include phase-space theory (PST)[22], orbiting transition state PST (OTS/PST),[13]and a reformulated quasi-equilibrium theory (QET)[23]. There is also a variety of analytical methods worth acknowledging including finite heat bath theory

(FHBT)[24], the model free approach,[25] and the prior method.[26]

Thermodynamic information from the GIBMS is extracted using a statistical model with a basis in RRKM[27, 28, 29] developed by Armentrout et al.[30, 31] This model has evolved over the years to incorporate lifetime effects, competitive pathways, and a treatment of rotors corresponding to the phase space limit. Because KERDs are not directly given by RRKM, a reformulation of this statistical model was required.

PST and QET methods are generally used over RRKM methods to reproduce KERDS. This can be attributed to the widely held notion that KERDs are measured properties of the products[13, 32] which are explicitly considered using the former methods, whereas RRKM methods only consider the transition state species and are therefore better suited for reaction rate calculations. For reactions proceeding over loose transition states, however, the methods are analogous.[23] Simple bond cleavages proceed over loose transition states and have been successfully modeled in the Armentrout lab for the last 30 years. Therefore, it stands to reason that KERDs of those reactions can be modeled using the same statistical methods currently employed in the Armentrout lab. Doing so gives the ability to extract complementary thermodynamic data for a given chemical system (i.e., cross sections *and* KERDs) using only one instrument.

To realize the benefits of examining KERDs, it is instructive to understand the different potential energy surfaces through which a reaction can proceed. The first surface is that of a loose transition state, which is characterized by an increase in energy from the reactant that levels off asymptotically upon product formation, see Figure 6.1a. The transition state, in this case, is achieved with negligible energy to the reverse reaction. The KER to products has a statistical distribution that falls off rapidly at high

product KE and has a maximum at very low energies because of conservation of angular momentum[33]. The KERDs for loose transition states are very much a measurement of the internal energy excitation of the reactant ion.[5]

The second surface is that of a tight transition state which is characterized by a barrier to the reverse reaction, see Figure 6.1b. In the absence of any dynamic effects, generally referred to as exit channel interactions, this barrier energy is released exclusively to the KE of the products.[13] The KERD for such a scenario would resemble that of the loose transition state but shifted to higher energies by an amount corresponding to the barrier height.[13] In most cases, however, dynamic effects do exist and coupling between the reaction coordinate and various other modes causes nonstatistical broadening in the KERD.[13, 32] Nonetheless, the maximum of the KERD is representative of the height of the barrier to the reverse reaction.

In order to obtain bond dissociation energies (BDEs) with threshold collision induced dissociation (TCID) methods, reactants must be given enough energy to form products. For systems with a loose transition state, this is simply a matter of increasing the reactant kinetic energy until it exceeds that of products. For systems with a tight transition state, the reactant kinetic energy must overcome the barrier to the reverse reaction before products are formed. Because of this barrier, the experimental BDE is better described as the bond enthalpy. To obtain the true BDE we need only to subtract the barrier energy from the bond enthalpy.

Described below are our attempts to develop the statistical model of Armentrout et al. in such a way that it is capable of modeling KERDs from loose transition states. This is an ideal first step as it allows us to compare our model to statistically behaved

distributions. To test our model, we have obtained KERD data from three different systems: $Ca^{2+}(H_2O)_n$, where n = 4 – 8, $CuOH^+(H_2O)_n$, where n = 2 – 4, and H^+Gly, all of which were collided with Xe to form products. These systems represent reactants of varying charge, mass, and transition state type. The experimental setup used to obtain these data and the theory behind the statistical model is explained here in detail. A comparison between experimental data and the KERD model is made and a thorough analysis of the results is given.

6.2 Experimental

6.2.1 Instrumentation

The instrument used to obtain KERDs is a guided ion beam tandem mass spectrometer (GIBMS) that is described in detail elsewhere.[15, 34] Briefly, ions are created in an ESI[14] and then thermalized through collisional cooling with ambient gas in an ion funnel/hexapole.[35, 36] This ensures that the internal energy of the reactant ions can be described by a Maxwell-Boltzmann distribution centered at room temperature, as shown previously[37, 38, 39, 40, 41, 42]. The reactant ion beam is then selected using a magnetic momentum analyzer and is decelerated to a well-defined kinetic energy before being injected into an octopole ion guide[36] that is encompassed by a collision cell. After collisions with Xe, product and residual ions drift out of the octopole where they are mass selected using a quadrupole mass filter before being detected using a Daly detector.[43]

The main difference between operation of the GIBMS to obtain TCID cross sections and operation of the GIBMS to obtain KERD data lies in the setup of the octopole region. This region consists of two octopoles in series with the collision cell containing the end of the first octopole. The double octople arrangement was

implemented to offer higher resolution for TOF measurements than the previous single octopole and is described in detail elsewhere.[34] For cross section measurements, the first octopole voltage is swept across the reaction energies of interest and the second octopole floats on the first octopole voltage with a -0.3V bias to help carry ions to the detector. For KERD data, the first octopole is set to a fixed voltage and the second octopole voltage is swept across an ion stopping potential.

6.2.2 Experimental Methods

Sample preparation for the $Ca^{2+}(H_2O)_x$ and $CuOH^{+}(H_2O)_x$ systems consisted of dilution of $CaCl_2$ and $CuSO_4 \cdot (H_2O)_5$ salts, respectively, in neat water to a concentration of $1x10^{-4}$ M. For the H^{+}Gly system, mM amounts of acetic acid were added to a $1x10^{-4}$ M solution of Glycine in neat water to ensure protonation of Glycine. The electrospray needle voltage was operated at ~2 kV with the sample flowing at a rate of ~0.05 mL/hr to obtain maximum intensity of the ion beam. The DC drop between the inlet of the instrument to the end of the ion funnel was kept below 15 V to minimize collisional excitation.[37] Ion intensities are converted to cross sections using a Beer-Lambert law analogue described elsewhere.[15, 44] For each system, preliminary data were taken at varying Xe pressures to determine the effect of pressure on the cross section. Product channels susceptible pressure to effects were collected at 0.2, 0.1 and 0.05 mTorr and then extrapolated to zero pressure, which is rigorously a single-collision event. The voltage of ions in the lab frame (V_{lab}) is converted to energy in the center of mass frame (E_{CM}) by $E_{CM} = q\ x\ V_{lab}\ x\ (m/M)$, where m is the mass of the neutral, M is the sum of the reactant and neutral masses, and q is the charge on the ion. The differential intensity is fit with a Gaussian distribution and typically has a FWHM of ~0.12 eV.

6.2.3 Statistical Methods

In order to successfully model product kinetic energy distributions it is essential to understand the fundamental concepts underlying the collisional process. This is best achieved by considering the fate of a single reactant ion colliding with a single reactant neutral. The dissociation process begins with a voltage, V_{lab}, being imparted onto the reactant ion in the first octopole such that the energy is $E_{lab} = q\ x\ V_{lab}$. The quantity, E_{lab}, is a sum of E_{OCM} and E_{rel} . The energy of the center of mass, (E_{OCM}), is conserved throughout the process and is $E_{OCM} = E_{lab}\ (^{m_{ion}}/_{M})$. The remaining energy is the energy of the reactants relative to the center of mass, E_{rel}, and is nominally the energy available for dissociation.

Upon collision with Xe, the reactant ion and neutral form a short-lived intermediate that can survive for several rotational periods before falling apart, such that reactive scattering is assumed to be isotropic. The effect of the collision is a transfer of kinetic energy into internal modes of the reactant. The amount of energy transferred is dependent on the impact parameter and can be described by the line of centers model:

$$E_{dep} = E_{rel}(1 - {}^{b}/_{d}) \tag{6.1}$$

where E_{dep} is the amount of energy transferred (deposited), b is the impact parameter and d is the distance between centers of the reactants. This transfer has been shown to take place at high efficiency over the range of kinetic energies typically used in GIBMS studies.[34] The probability of a given E_{dep} for any one collision was determined by Muntean et al. to be[34]:

$$P(E_{dep}) = (E_{rel} - E_{dep})^{n-1}/E_{rel} \tag{6.2}$$

where n is an adjustable parameter that is system sensitive. The energy not deposited into internal modes remains in kinetic energy of the scattered reactants, E_{scat}.

If the initial internal energy of the reactant, E_{int}, plus E_{dep} of the energized molecule exceed the bond dissociation energy, E_0, then the reactant can dissociate to form products. For a given dissociation, the excess internal energy of the transition state is partitioned between internal and kinetic energy of the products. The kinetic energy released to product fragments ranges from all of the excess energy to none of it. Assuming a statistical partitioning of energy, the probability of having a given KER is described by the density of states of the TS, $\rho^{\ddagger}(E^*)$, where E^* represents the excess internal energy and is equal to $E_{dep} + E_{int} - E_0$. Because the density of states is a measure of the internal energy, the probability of a given kinetic energy is $\rho^{\ddagger}(E^* - \varepsilon)$ where $\varepsilon \leq E^*$. Therefore, if the density of states to the TS is large, there will be a high probability of having a fragment with lots of internal energy and little KER.

To summarize thus far, the amount of kinetic energy of a given product is composed of contributions from E_{OCM}, which does not change; E_{scat}, which is a function of the impact parameter; and ε, which is described by the density of states. Physically, the retarding potential measurements are a measure of the sum of velocity vectors for each of these contributions expressed as a function of energy. The probability of a product having a given kinetic energy, E_{prod}, must therefore be calculated in terms of velocities and is described by:

$$P(E_{prod}) = \int_0^{V_{scat,max}} dv_{scat} \int_0^{V_\varepsilon} dv_\varepsilon \int_{E_{prod}}^{E_{all}} \frac{(E_{rel}-E_{dep})^{n-1}}{E_{rel}} \rho^{\ddagger}(E^* - \varepsilon)\, dE_{scat} \quad (6.3)$$

where $E_{all} = \frac{1}{2}mv_{all}^2$. Integrating from E_{prod} to E_{all} accounts for all products with kinetic energies greater than or equal to E_{prod}. The maximum of this integral, E_{all}, is a function of v_{all} ,which is a sum of all the contributing factors to the total velocity of the products, namely: $v_{all} = v_{OCM} + v_{scat} + v_{\varepsilon}$. Squaring v_{all} leads to a number of "cross-terms" that broaden the distribution of product kinetic energies.[32]

$$E_{all} = \frac{1}{2}m[v_{OCM}^2 + 2(v_{OCM}v_{scat}) + 2(v_{OCM}v_{\varepsilon}) + v_{scat}^2 + (v_{scat}v_{\varepsilon}) + v_{\varepsilon}^2] \quad (6.4)$$

For this reason, experiments that measure the kinetic energy release as a function of energy rather than as function of velocity are generally more precise. It is also the reason that $P(E_{prod})$ cannot simply be thought of in terms of energy. The terms needed to calculate v_{all}, namely $v_{scat}$and v_{ε}, are supplied through the first two integrals, the limits of which prevent nonreal probabilities of E_{prod}. The third term, v_{OCM}, is a constant given by $E_{OCM} = \frac{1}{2}mv_{OCM}^2$. The limits of the first two integrals are defined as follows:

$$v_{scat,max} = \sqrt{2(E_{rel} - E_0 + E_{int})/\mu} \quad (6.5)$$

$$v_{\varepsilon} = \sqrt{2(E_{scat} + E_{int})/\mu_{prod}} \quad (6.6)$$

It is important to keep in mind that for both the scattering and KER events, the velocity carried away by separating masses, v_a and v_b, is a ratio of the total velocity, v, for that phenomenon, such that $v_a = v\frac{m_b}{m_a}$ and $v_b = v\frac{m_a}{m_b}$. Because we are only interested in the fate of the fragment ion, the velocity component for the reactant ion after the scattering event is $v_{scat,ion} = v_{scat}\frac{m}{m_{ion}}$ and the velocity component of the product ion for the subsequent KER event is $v_{\varepsilon,PI} = v_{scat}\frac{m_{PN}}{m_{PI}}$ where the quotient corresponds to the mass of the product neutral over the mass of the product ion.

The distribution of scattering angles must also be taken into account. The experimental measurement of this distribution is the projection of the scattering angle along the axis of the ion guide, cos (θ) . The probability of the cos(θ) projection is sin(θ) such that E_{prod} is:

$$P(E_{prod}) = \int_0^{\pi} d\theta \int_0^{V_{scat,max}} dv_{scat} \int_0^{V_{\varepsilon}} dv_{\varepsilon} \int_{E_{prod}}^{E_{all}} \frac{sin\theta(E_{rel}-E_{dep})^{n-1}}{E_{rel}} \rho^{\ddagger}(E^* - \varepsilon)\, dE_{scat} \tag{6.7}$$

where v_{scat}, and v_{ε} in the extended v_{all}^2 term are now accompanied by cos (θ). In practice, the distribution of scattering angles is not always isotropic and is highly dependent on the impact parameter. It has been shown that for collision energies near threshold, products assume isotropic scattering while collision energies in excess of the threshold tend to scatter forward in the center of mass frame.[34] Assuming 100% efficiency of energy deposition along the line of centers, the minimum amount of energy that must be deposited in order to form products corresponds to a minimum impact parameter that translates to a minimum scattering angle, β_{min}:

$$cos^2\beta_{min} = {}^{E_{dep} + E_i - E_0}/_{E} \tag{6.8}$$

where $\beta_{min} = 90°$ corresponds to isotropic scattering while $\beta_{min} = 0°$ corresponds to forward scattering. The justification for this relation can be found in detail elsewhere.[34] The integration over reactive scattering is therefore taken from 0 to $2\beta_{min}$ to reflect symmetry.

6.2.4 Lifetime Restrictions

For some reactions, the lifetime for dissociation may be longer than the experimental window. To account for this, we introduce a probability for dissociation in the experimental timeframe using statistical rate theory. Lifetimes for all energized molecules are obtained by taking the inverse of the unimolecular rate constant, $k(E_{react}) = k(E_{dep} + E_{int})$, which is defined by RRKM theory as:

$$k(E_{react}) = sN^{\ddagger}(E_{react} - E_0)/h\rho(E_{react}) \tag{6.9}$$

where s is the reaction degeneracy, $N^{\ddagger}(E_{react} - E_0)$ is the sum of states to the transition state, and $\rho(E_{react})$ is the density of states of the energized molecule. Including the lifetime requirement into the model gives:

$$P(E_{prod}) = \int_0^{\pi} d\theta \int_0^{V_{scat,max}} (1 - e^{-k(E_{react})\tau}) dv_{scat} \int_0^{V_{\varepsilon}} dv_{\varepsilon} \int_{E_{prod}}^{E_{all}} A \, dE_{scat} \tag{6.10}$$

where τ is the experimental time available for dissociation and $A = \frac{sin\theta(E_{rel} - E_{dep})^{n-1}}{E_{rel}} \rho^{\ddagger}(E^* - \varepsilon)$. In the limit that the lifetimes of the complex are extremely small, this equation recovers eq. (6.7).

6.2.5 Angular Momentum

Finally, the energetic consequences of angular momentum on the KERD must be addressed. To begin, it is important to remember that the total angular momentum, J, must be conserved throughout the collisional process. This means that $J = J_R + L$ where $J_R = J_{PN} + J_{PI}$ corresponding to the rotational angular momenta of the product neutral and product ion, respectively, and L is the orbital angular momentum. In the PSL treatment by Armentrout et al., the rotational angular momentum of the products, J_R, is approximated by the 2D external rotations of the EM and is coupled with L.[31] Energy in

these motions therefore is unavailable to the EM for dissociation. This changes the rate constant such that:

$$k(E_{react},J) = sN^{\ddagger}(E_{react} - E_R^{\ddagger}(J) - E_0)/h\rho(E_{react} - E_R(J)) \qquad (6.11)$$

where $E_R^{\ddagger}(J)$ and $E_R(J)$ are the energies in the 2D external rotations of the TS and the EM, respectively. The relationship between these two rotational energies and the collision energy is defined using a variational approach pioneered by Gilbert and Smith[27] and implemented by Armentrout et al.[30]

$$E_r^{\ddagger}(J) = V_{eff}(r_{react}) = (\pi\epsilon_0/2\alpha e^3\mu^2)(\hbar^2 E_r(J)/hcB) \qquad (6.12)$$

where $E_R^{\ddagger}(J)$ is pinned to the position of the centrifugal barrier, which for a loose transition state is the energy along the reaction coordinate where the derivative of $V_{eff}(r_{react}) = 0$. The value of $E_r(J)$ is described using a statistical average of $\langle E_R \rangle$ summed over possible rotational quantum numbers of the 2D rotor:

$$\langle E_R \rangle = \sum_{J=0}^{J_{max}} E_R(J) g_J \rho(E_{react} - E_R(J)) / \sum_{J=0}^{J_{max}} g_J \rho(E_{react} - E_R(J)) \qquad (6.13)$$

where $J_{max} = (\left(1 + \frac{4E_{react}}{B}\right)^{\frac{1}{2}} - 1)/2$.

There are several interesting consequences of angular momentum's role in the collision. The first consequence deals with the 2D external rotations described above. The rotational constants for both the TS ($B^{\ddagger}$) and the EM (B) are a function of the moment of inertia, I, such that $B^{\ddagger} = h/8\pi^2 cI^{\ddagger}$ and $B = h/8\pi^2 cI$. Because $I^{\ddagger}$ increases as the TS moves towards products, $E_R^{\ddagger}(J)$ becomes smaller than $E_R(J)$, thereby increasing the unimolecular dissociation rate.

The second consequence deals with the orbital angular momentum, L. The total angular momentum of the collision complexes, J, is predominantly expressed

postcollision as L. Large L-values result in large centrifugal barriers, the energy of which is preferentially released into product KE.[12] This preferential release into KE is due to the fact that after passing over the centrifugal barrier, the products fall down the repulsive wall and dissociate before they are able to adequately redistribute the energy.[45] To account for this preferential release of energy to the KERD, we add the orbital angular momentum to the KE of the products such that $v_{all} = v_{OCM} + v_{scat} + v_{\varepsilon} + v_l$ where $L = (J(J+1)\hbar^2)^{1/2}$. The effect is the introduction of more cross terms and an increase in the high energy portion of the KERD.

Unfortunately, we were unable to incorporate several of the above mentioned factors into the software version of our statistical model, including angular momentum and lifetime effects. As each factor typically requires an additional integration, a complete model would have been computationally demanding. Consideration of isotropic scattering was also omitted, and was replaced by an assumption that all products are forward scattered. This approach was far less demanding and only resulted in minor changes to the model, as discussed later. The importance of incorporating each of these factors is outlined with examples later in the text.

6.2.6 Theoretical Calculations

Quantum chemical calculations were performed using the same methods described in previous chapters. Briefly, densities of state for all transition states were obtained using a Beyer-Swinehart-Stein-Rabinovitch[46, 47, 48] algorithm. Vibrational frequencies for the transition states as well as for the reactants and products were taken from electronic state calculations and were scaled by 0.989.[49] All electronic state calculations were performed using the Gaussian 09 suite of programs.[50] Myriad

structural conformations were probed and optimized to find the low energy isomers and their rotational and vibrational frequencies at the B3LYP/6-311+G(2d,2p)[51, 52] level of theory.

6.3 Results and Discussion

6.3.1 $Ca^{2+}(H_2O)_n$

The accuracy of the statistical KERD model was tested against a range of systems. These systems presented a variety of collisional scenarios including: increasing/decreasing contributions from angular momentum, small/large kinetic shifts, and varying charge states. Each scenario and the systems used to test it are presented in detail below.

The initial test of our methods was the $Ca^{2+}(H_2O)_6$ system. Experimentally, $Ca^{2+}(H_2O)_6$ was an ideal starting point for this study because of its high signal intensity and stable electrospray signal. A comprehensive experimental and theoretical investigation of this system was performed by Carl et al. using TCID methods on the same GIBMS used in this study.[41] From that study, the adjustable parameters, E_0 and n were obtained for each complex size. These parameters are the same ones needed for the KERD model. As such, they served as a good foundation from which the model could be tested.

The KERD for $Ca^{2+}(H_2O)_6$ was investigated at a nominal 1st octopole voltage of 1.5 V, which yields 1.68 V after subtracting the zero of energy, and 1.58 eV after conversion to the center of mass energy. The result is the dissociation of the reactant to form $Ca^{2+}(H_2O)_5$ and subsequently, $Ca^{2+}(H_2O)_4$, shown in Figure 6.2a. The lower x-axis represents the retarding energy in the center of mass frame and the upper x-axis the

retarding energy in the lab frame. The y-axis is the relative intensity of products. The blue trace represents the KERD for $Ca^{2+}(H_2O)_5$. Although the shape of the KERD trace is very similar to the CID cross sections of Carl et al. shown Figure 6.2b, the only direct relationship between the two is that the maximum intensity of the KERD data correspond to the CID cross section at the given 1st octopole energy. This point is better demonstrated by the $Ca^{2+}(H_2O)_4$ trace, which abruptly flattens at a relative intensity of ~1, and is equal to the cross section for $Ca^{2+}(H_2O)_4$ at the same energy. The 1st octopole energy of 1.58 eV is given by the black vertical line. At and above this energy on the 2nd octopole, the retarding potential is 0 eV or less, and all products are able to pass through to the detector. The lower the 2nd octopole energy, the higher the retarding potential such that 0 eV on the 2nd octopole corresponds to a retarding potential of 1.58 eV.

In Figure 6.2a, the intensity of $Ca^{2+}(H_2O)_5$ has an apparent threshold of ~0.2 eV, which corresponds to a product kinetic energy of ~1.58 – 0 .2 = 1.38 eV. The 0 K BDE for $Ca^{2+}(H_2O)_6$, was found by Carl et al., to be 0.92 eV (0.86 V). Subtracting this BDE from the 1st octopole energy yields a maximum product kinetic energy of 1.58 – 0.92 = 0.66 eV, which is much lower than the 1.38 eV measured here. This difference comes from the large amount of internal energy of the $Ca^{2+}(H_2O)_6$ reactant at 298 K. Indeed, looking at the TCID cross sections of Carl et al. confirms that $Ca^{2+}(H_2O)_6$ has enough internal energy to dissociate, even at collision energies of 0 eV.

The product kinetic energy of products can be visualized differently by subtracting the 1st octopole energy by the 2nd octopole energy, given in Figure 6.2c. Now, the x-axis represents the product kinetic energy, the vertical black line represents the maximum energy, and the apparent threshold is 1.38 eV. Differentiating this intensity

gives Figure 6.2b. Note the maximum at low energies, which comes from conservation of angular momentum. The decrease in product intensity at low energies is slightly more pronounced for $Ca^{2+}(H_2O)_5$ because it begins to dissociate into the $Ca^{2+}(H_2O)_4$ product.

As an initial test of the KERD model, we collected data from the dissociation of $Ca^{2+}(H_2O)_6$ to form $Ca^{2+}(H_2O)_5$ at a 1st octopole voltage of 1.05 eV, which represents energy barely in excess of the BDE of 0.92 eV found by Carl et al.[41], see Figure 6.3a. The KERD model, given by the blue line, does an excellent job of reproducing the distribution at high energies but underestimates the distribution at lower energies. It is worth mentioning, however, that this model has no adjustable parameters. As mentioned above, E_0 and N are both taken from literature values. Increasing N from the value obtained by Carl et al. from 1.1 to 5.0 results in a remarkable fit of the data, given in Figure 6.3b. However, changing this parameter does not always guarantee a good fit, nor is it advised if meaningful thermodynamic values are to be extracted from the data.

6.3.2 Angular Momentum

Angular momentum has a larger effect on KERDs obtained from CID than it does on those obtained from photoionization techniques.[12] For this reason, it is crucial that the KERD model developed here accurately describe any effects arising from conservation of angular momentum. The centrifugal barrier, in particular, needs to be carefully accounted for due to its preferential release into product kinetic energy.

The maximum angular momentum of the transition state, as described earlier, is a sum of the total rotational and orbital angular momentum of the products, $J_r + L$. The maximum orbital angular momentum is a function of E_{rel}, such that increasing E_{rel} increases the maximum angular momentum, J. When E_{rel} is large, the total angular

momentum, J, is mainly comprised of orbital angular momentum of the products, L. As L increases, the centrifugal barrier grows and the KER to products is greater.

To demonstrate the importance of including angular momentum effects, the 1st octopole voltage was incrementally increased and the KERD measured at each step. The KERDs from Ca6w were measured at 1st octopole voltages ranging from 0.9 V, representing energy barely in excess of the threshold (0.86 V for Ca6w [41]) to 1.8V, see Figure 6.4. In each case, the maximum intensity is not achieved until the retarding potential goes to 0 eV, again given by the vertical black line. As the collision energy increases, so too does the maximum product kinetic energy. The apparent thresholds for each system are unchanged at ~ 0.2 eV, which indicates that most of the collision energy in excess of the BDE is going into the kinetic energy of the products.

The KERD from a collision energy of 0.9 V is given once more in Figure 6.4a. As the collision energy increases, shown in Figures 6.4b-d, the KERD model further underestimates the low energy region. In all cases, increasing the N value improves the fit at lower energies but does not completely reproduce the threshold region for data sets taken at high collision energies. The discrepancy at lower energies near the threshold highlights contributions to the KERD from the centrifugal barrier and underlines the need to include angular momentum, which is presently lacking from the KERD model.

6.3.4 Lifetime Effects

Careful consideration must also be given to products whose lifetimes are larger than the experimental window. Often, these products arise when the angular momentum is relatively large or the amount of energy deposited into internal modes upon collision is relatively small. Both scenarios result from large impact parameters. For a given amount

of energy deposited into internal modes, the average lifetime increases as a function of the complexity of the system. That is, larger systems have larger lifetimes because they have more quantum states available into which energy can be distributed.

The KERDs for $CuOH^+(H_2O)_3$ and $CuOH^+(H_2O)$ dissociating to lose a water were measured on the GIBMS and analyzed using the KERD model, see Figure 6.5. For each system, the model shown was created from the parameters found in our previous study. For consistency, the collision energy in each case was set to ~0.5 eV in excess of the BDE. For $CuOH^+(H_2O)$ dissociating to form $CuOH^+$, there is excellent agreement between the data and the model across the entire energy range investigated, see Figure 6.5a. As the size of the reactant increases to $CuOH^+(H_2O)_3$, however, the model is unable to reproduce the low energy region of the data, see Figure 6.5b.

6.3.6 H^+Gly

As previously indicated, the overarching goal of this study is to establish a method for measuring barrier heights. The ability to do so would allow elucidation of the bond dissociation energy by subtraction of the barrier energy from the measured bond enthalpy. A nice example of the kinetic energy broadening that can be expected from the release of the barrier energy to products can be found in the dissociation of H^+Gly. This system dissociates via two competing mechanisms with similar thresholds. The first mechanism is the loss of CO over a tight transition state. The second mechanism involves the sequential loss of H_2O over a loose transition state. The bond dissociation energies for each mechanism were found by Armentrout et al. to be 1.68 and 1.82 eV, respectively, with n-values of 0.8 and 1.1, respectively.[53] The KERD for each pathway is shown in Figure 6.6. The KERD from the tight transition state (blue) is much broader

than that of the loose transition state (red), which is indicative of the non-statistical release of energy into translational modes of the product.

The ability to discern between tight and loose transition states is promising for measuring the barrier height of the charge separation pathway. At the very least, it allows us to measure the maximum kinetic energy released. This could be achieved by modeling the KERD from a tight transition state using the statistical model. The difference between the threshold predicted by the model and the actual threshold would give the maximum kinetic energy released, which equals the barrier height. This method, however, is dependent on the statistical model being able to accurately reproduce KERDs from a range of statistical processes, which at present, it cannot do. However, the shortcomings of this model have been identified and the methods to improve it have been outlined for future consideration.

6.4 Conclusion

The KERDs resulting from the CID of $Ca^{2+}(H_2O)_6$, $CuOH^+(H_2O)_3$, $CuOH^+(H_2O)_2$, and H^+Gly were measured using a GIBMS modified to perform retarding potential measurements. These measurements were modeled using a reformulation of the statistical model created by Armentrout et al. This model used the density of states at the transition state as well as the energy deposition function and an assumption that all products were forward scattered to attempt to reproduce the experimental data. This model was tested across a range of lifetimes, centrifugal effects, and charge states. These tests all saw reasonable agreement between the model and the experimental data at low product kinetic energies (high retarding potential), however, were less accurate at higher product kinetic energies. This deviation at higher energies underlines the need to include

angular momentum and lifetime effects of the energized molecule and products. Examples of dissociation over loose and tight transition states were given for the loss of CO + H2O and CO, respectively, from the H^+Gly system. The larger KERD for the loss of CO, which occurs over a tight transition state, confirms the nonstatistical release of energy into translation that is typical for a barrier to the reverse reaction. This study lays the foundation for the analysis of KERDs using a GIBMS. We predict the ability to use this method as a way of measuring the barrier height resulting from dissociation over tight transition states. The ability to do so would allow for the measurement of true bond dissociation energies from the bond enthalpies typically measured in TCID experiments of tight transition states.

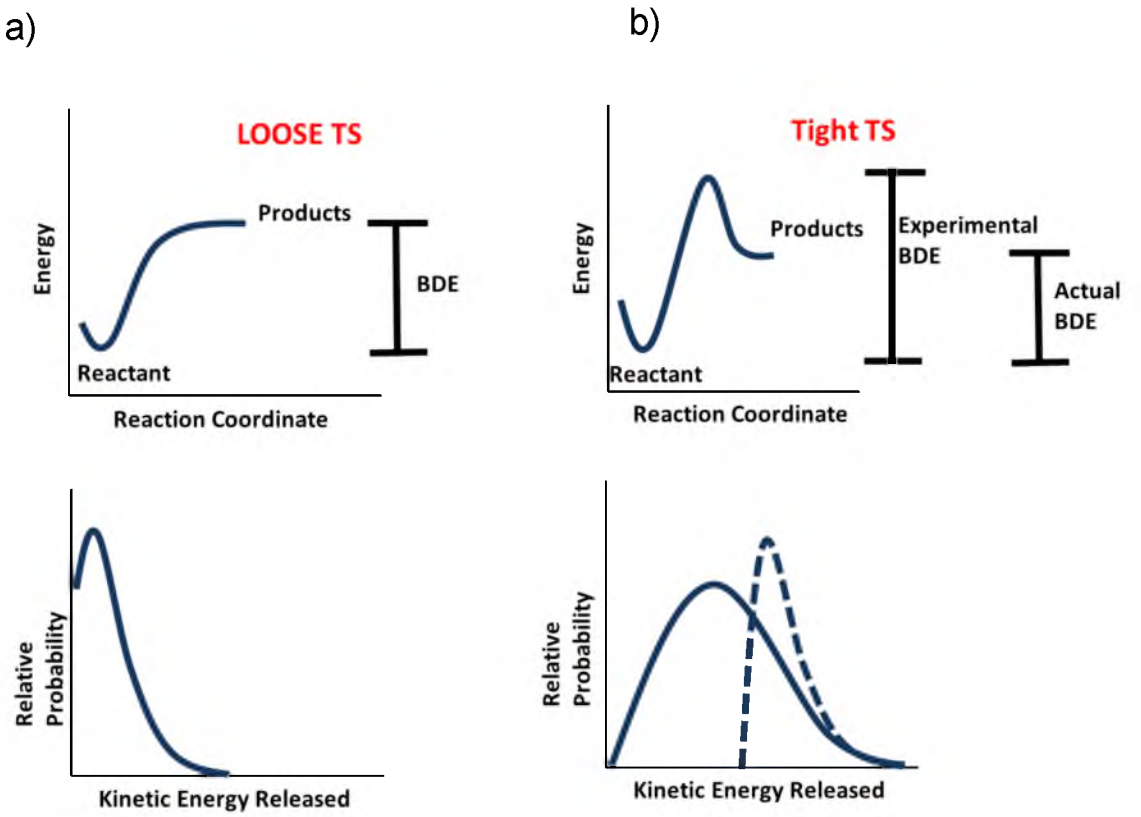

Figure 6.1. PES and resulting KERD for a) loose transition states and b) tight transition states as a function of the reaction coordinate. Black bars depict the amount of energy required to go from reactant to products. Dashed line represents the KERD in the absence of exit channel interactions.

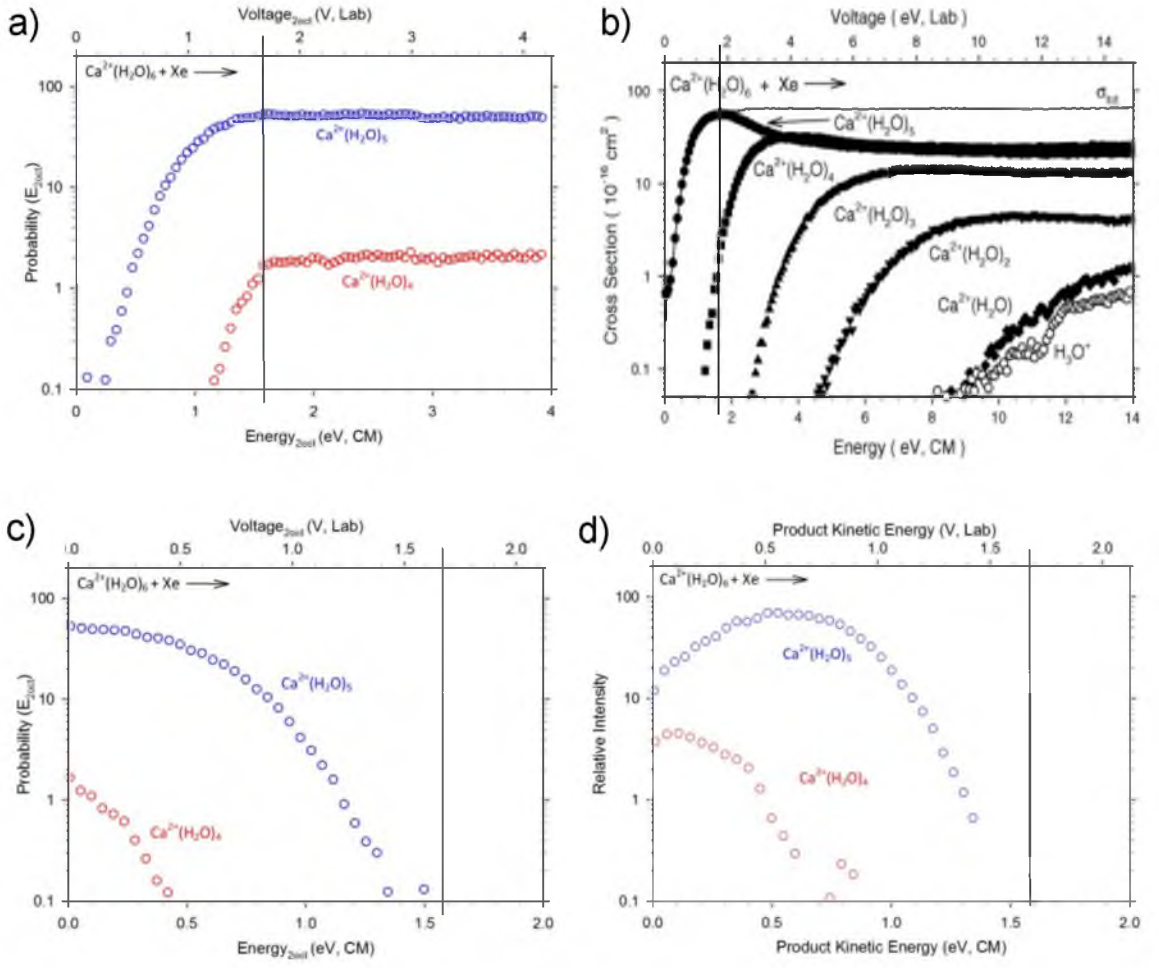

Figure 6.2. KERDs for $Ca^{2+}(H_2O)_5$ and $Ca^{2+}(H_2O)_4$ at a 1st octopole voltage of 1.68V (1.58 eV) with a) integral intensity, c) integral intensity and the energy scale of data has been inverted to reflect the product kinetic energy, and d) differentiated intensity and the energy scale of data has been inverted to reflect the product kinetic energy. B shows the CID cross sections for $Ca^{2+}(H_2O)_6$ colliding with Xe to form products from a study by Carl et al.[41] The black vertical lines represent 1.58 eV.

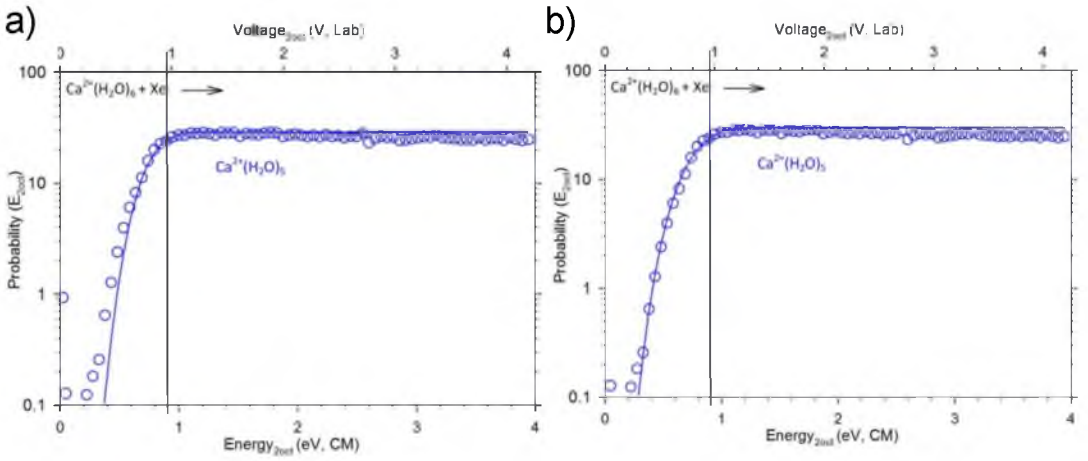

Figure 6.3. KERDs for $Ca^{2+}(H_2O)_6$ dissociating to form $Ca^{2+}(H_2O)_5$ at a 1st octopole voltage of 0.9 V (1.05 eV). Blue line represents the KERD model convoluted of kinetic and internal energy distributions of the reactant ion and neutral with a) E_0 and N parameters from Carl et al.[41] and b) N = 5. The black vertical lines represent 1.05 eV.

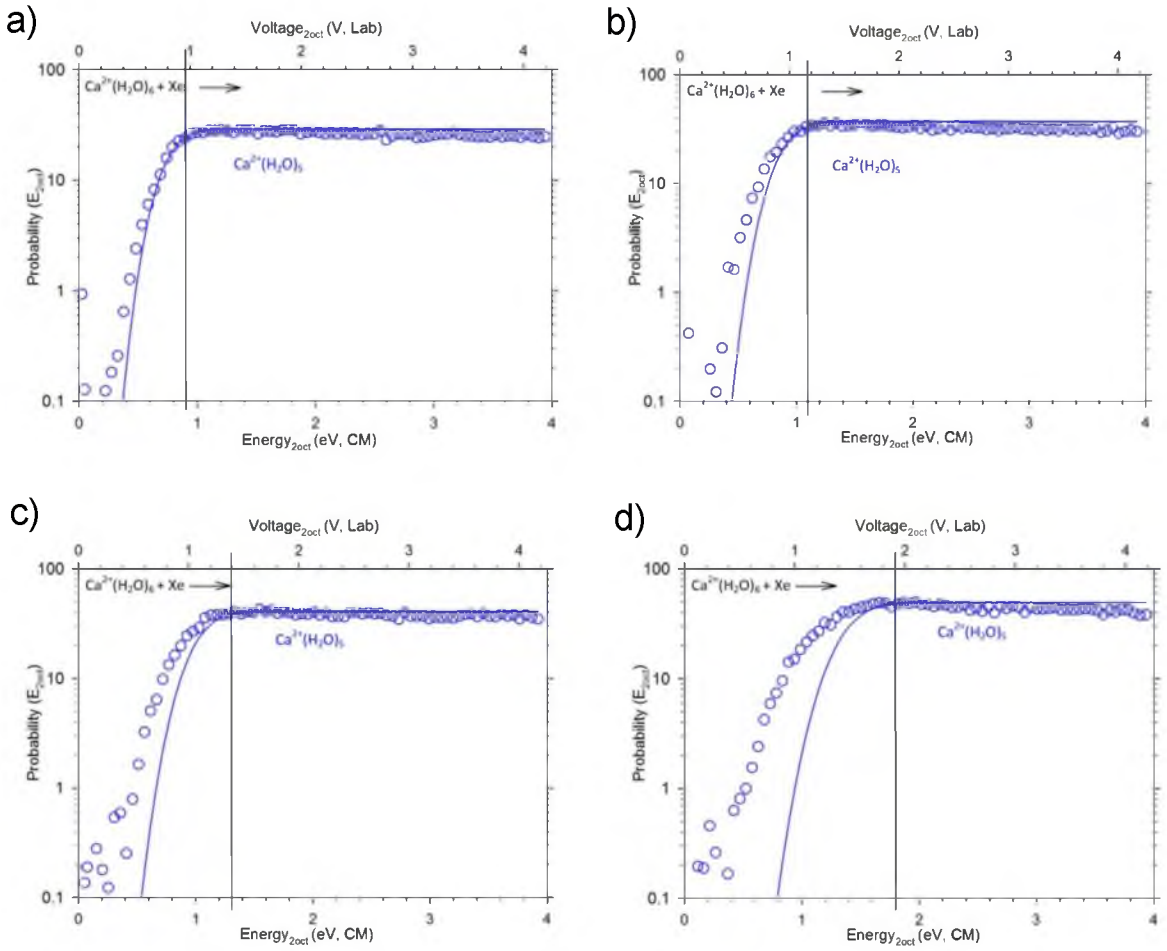

Figure 6.4. KERDs for Ca5w 1st octopole voltages of a) 0.9, b) 1.1, c) 1.3 and d) 1.8 V given by the black line. The blue line represents the KERD model convoluted over the kinetic and internal energies of the reactant ion and neutral. The black vertical lines represent the 1st octopole energy.

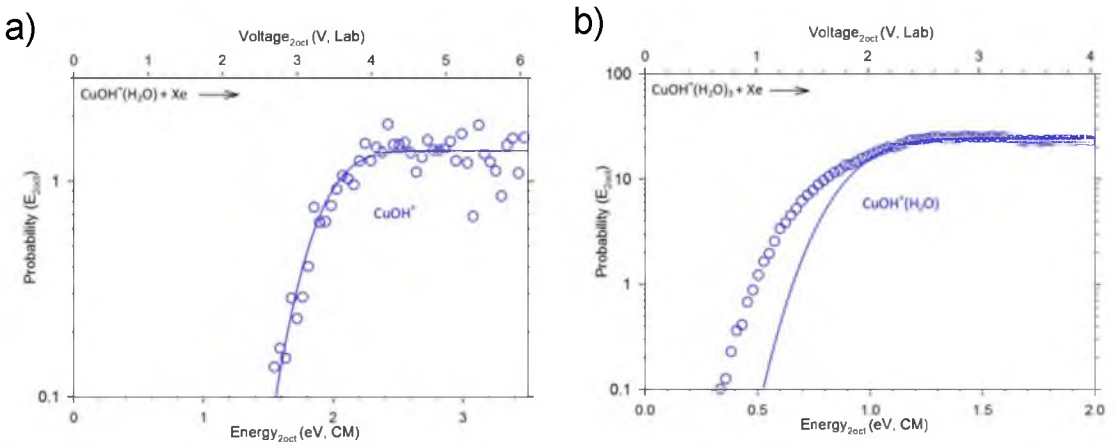

Figure 6.5. KERDs for a) $CuOH^+(H_2O)$ dissociation to form $CuOH^+$ at a 1st octopole voltage of 4.0 V (2.3 eV) and b) $CuOH^+(H_2O)_3$ dissociating to form $CuOH^+(H_2O)_2$ at a 1st octopole voltage of 2.5 V (1.3 eV). The blue line represents the KERD model convoluted over the kinetic and internal energies of the reactant ion and neutral.

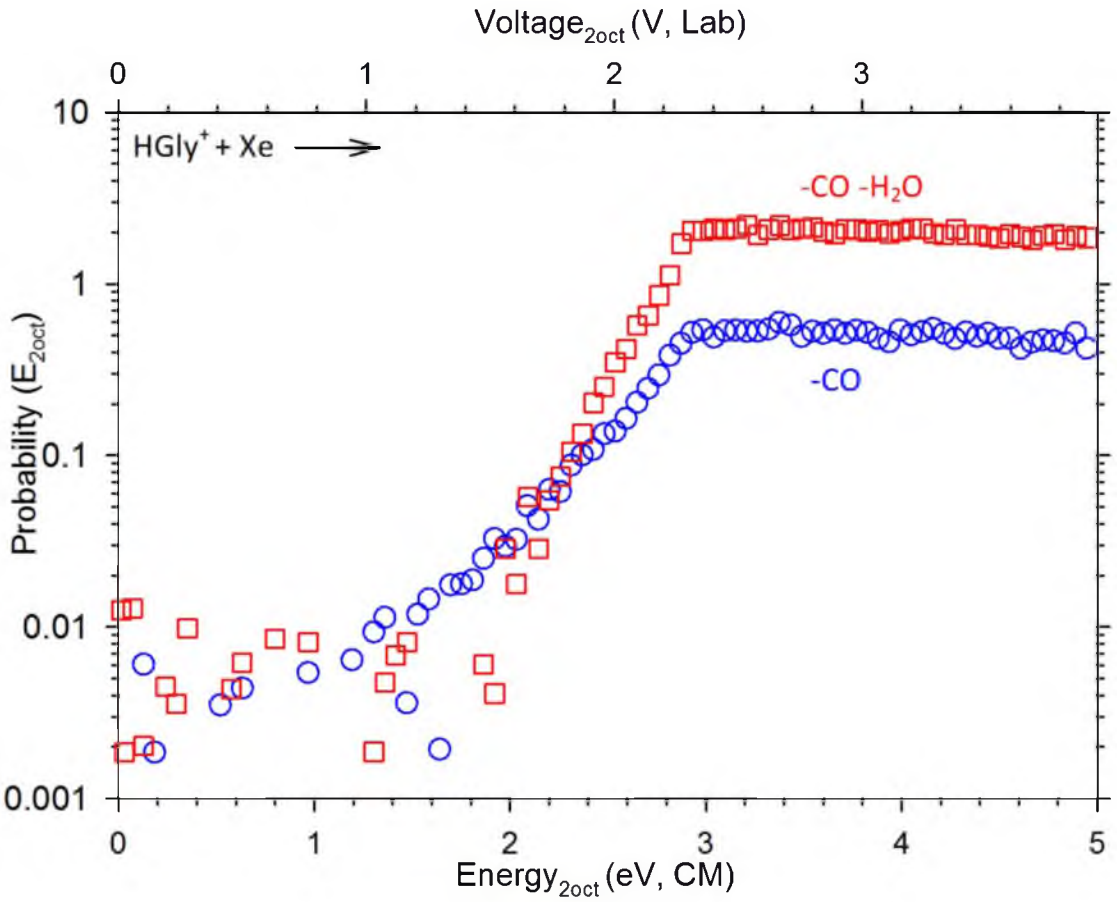

Figure 6.6. KERDs of H^+Gly dissociating to lose CO over a tight transition state (blue, bottom) and to lose an additional H_2O over a loose transition state (red, top).

6.4 References

[1]Bleakney, W., Phys. Rev. **35,** 1180 (1930)

[2]Beynon, J. H.; Cooks, R. G.; Amy, J. W.; Baitinger, W. E.; Ridley, T. Y., Anal. Chem. **45,** 1023A (1973)

[3]Mintz, D. M.; Baer, T., J. Chem. Phys **65,** 2407 (1976)

[4]Bahati, E. M.; Jureta, J. J.; Belic, D. S.; Cherkani-Hassani, H.; Abdellahi, M. O.; Defrance, P., J. Phys. B: At., Mol. Opt. Phys. **34,** 2963 (2001)

[5]Lifshitz, C., J. Phys. Chem. **87,** 2304 (1983)

[6]Klots, C. E., J. Chem. Phys. **58,** 5364 (1973)

[7]Farrar, J. M.; Lee, Y. T., J. Chem. Phys. **65,** 1414 (1976)

[8]Stace, A. J.; Shulka, A. K., Int. J. Mass Spectrom. Ion Physics **37,** 35 (1981)

[9]Herman, Z.; Birkinshaw, K.; Pacak, V., Int. J. Mass Spectrom. Ion Processes **135,** 47 (1994)

[10]Hanratty, M. A.; Beauchamp, J. L.; Illies, A. J.; Van Koppen, P.; Bowers, M. T., J. Am. Chem. Soc. **110,** 1 (1988)

[11]Cho, S. I.; Choe, J. C.; Kim, M. S., Rapid Commun. Mass Spectrom. **7,** 594 (1993)

[12]Klots, C. E.; Mintz, D.; Baer, T., J. Chem. Phys. **66,** 5100 (1977)

[13]Chesnavich, W. J.; Bowers, M. T., J. Am. Chem. Soc. **98,** 8301 (1976)

[14]Yamashita, M.; Fenn, J. B., J. Phys. Chem. **88,** 4451 (1984)

[15]Ervin, K. M.; Armentrout, P. B., J. Chem. Phys. **83,** 166 (1985)

[16]Aristov, N.; Armentrout, P. B., J. Phys. Chem. **90,** 5135 (1986)

[17]Ervin, K. M.; Armentrout, P. B., J. Chem. Phys. **86,** 2659 (1987)

[18]Fisher, E. R.; Schultz, R. H.; Armentrout, P. B., J. Phys. Chem. **93,** 7382 (1989)

[19]Carl, D. R.; Chatterjee, B. K.; Armentrout, P. B., J. Chem. Phys. **132,** 1 (2010)

[20]Mookherjee, A.; Armentrout, P. B., Int. J. Mass Spectrom. **370,** 16 (2014)

[21]Garcia, G.; Mejía-Ospino, E.; Gurerrero, A.; Álvarez, I.; Cisneros, C., Eur. Phys. J. D **42,** 393 (2006)

[22]Light, J. C., J. Chem. Phys. **40,** 3221 (1964)

[23]Klots, C. E., J. Phys. Chem. **75,** 1526 (1971)

[24]Klots, C. E., J. Chem. Phys. **98,** 1110 (1993)

[25]Klots, C. E., J. Chem. Phys. **90,** 4470 (1989)

[26]Urbain, P.; Leyh, B.; Remacle, F.; Lorquet, A. J., J. Chem. Phys. **110,** 2911 (1998)

[27]Gilbert, R. G.; Smith, S. C., *Theory of Unimolecular and Recombination Reactions*. Blackwell Scientific: London, 1990.

[28]Holbrook, K. A.; Pilling, M. J.; Robertson, S. H., *Unimolecular Reactions*. 2nd ed.; Wiley: New York, 1996.

[29]Truhlar, D. G.; Garrett, B. C.; Klippenstein, S. J., J. Phys. Chem. **100,** 12771 (1996)

[30]Rodgers, M. T.; Ervin, K. M.; Armentrout, P. B., J. Chem. Phys. **106,** 4499 (1997)

[31]Rodgers, M. T.; Armentrout, P. B., J. Chem. Phys. **109,** 1787 (1998)

[32]Laskin, J.; Lifshitz, C., J. Mass Spectrom. **36,** 459 (2001)

[33]Lifshitz, C.; Berger, P.; Tzidony, E., Chem. Phys. Lett. **95,** 109 (1983)

[34]Muntean, F.; Armentrout, P. B., J. Chem. Phys. **115,** 1213 (2001)

[35]Teloy, E.; Gerlich, D., Chem. Phys. **4,** 417 (1974)

[36]Gerlich, D., Adv. Chem. Phys. **82,** 1 (1992)

[37]Moision, R. M.; Armentrout, P. B., J. Am. Soc. Mass Spectrom. **18,** 1124 (2007)

[38]Heaton, A. L.; Moision, R. M.; Armentrout, P. B., J. Phys. Chem. A **112,** 3319 (2008)

[39]Heaton, A. L.; Armentrout, P. B., J. Phys. Chem. A **112,** 10156 (2008)

[40]Carl, D. R.; Moision, R. M.; Armentrout, P. B., J. Am. Soc. Mass Spectrom. **20,** 2312 (2009)

[41]Carl, D. R.; Moision, R. M.; Armentrout, P. B., Int. J. Mass Spectrom. **265,** 308 (2007)

[42]Cooper, T. E.; Armentrout, P. B., Chem. Phys. Lett. **486,** 1 (2010)

[43]Daly, N. R., Rev. Sci. Instrum. **31,** 264 (1960)

[44]Armentrout, P. B., J. Am. Soc. Mass Spectrom. **13,** 419 (2002)

[45]Baer, T.; Hase, W. L., *Unimolecular Reaction Dynamics: Theory and Experiments*. Oxford University Press: New York, 1996.

[46]Beyer, T. S.; Swinehart, D. F., Commun. ACM **16,** 379 (1973)

[47]Stein, S. E.; Rabinovitch, B. S., J. Chem. Phys. **58,** 2438 (1973)

[48]Stein, S. E.; Rabinovitch, B. S., Chem. Phys. Lett. **49,** 183 (1977)

[49]Bauschlicher, C. W.; Partridge, H., J. Chem. Phys. **103,** 1788 (1995)

[50]Frisch, M. J.; Trucks, G. W.; Schlegel, H. B.; Scuseria, G. E.; Robb, M. A.; Cheeseman, J. R.; Scalmani, G.; Barone, V.; Mennucci, B.; Petersson, G. A.; Nakatsuji, H.; Caricato, M.; Li, X.; Hratchian, H. P.; Izmaylov, A. F.; Bloino, J.; Zheng, G.; Sonnenberg, J. L.; Hada, M.; Ehara, M.; Toyota, K.; Fukuda, R.; Hasegawa, J.; Ishida, M.; Nakajima, T.; Honda, Y.; Kitao, O.; Nakai, H.; Vreven, T.; Montgomery, J. A.; Peralta, J. E.; Ogliaro, F.; Bearpark, M.; Heyd, J. J.; Brothers, E.; Kudin, K. N.; Staroverov, V. N.; Kobayashi, R.; Normand, J.; Raghavachari, K.; Rendell, A.; Burant, J. C.; Millam, J. M.; Iyengar, S. S.; Tomasi, J.; Cossi, M.; Rega, N.; Millam, J. M.; Klene, M.; Knox, J. E.; Cross, J. B.; Bakken, V.; Adamo, C.; Jaramillo, J.; Gomperts, R.; Stratmann, R. E.; Yazyev, O.; Austin, A. J.; Cammi, R.; Pomelli, C.; Ochterski, J. W.; Martin, R. L.; Morokuma, K.; Zakrzewski, V. G.; Voth, G. A.; Salvador, P.; Dannenberg, J. J.; Dapprich, S.; Daniels, A. D.; Farkas, O.; Foresman, J. B.; Ortiz, J. V.; Cioslowski, J.; Fox, D. J. *Gaussian 09, Revision A.02*, Gaussian Inc.: Pittsburgh, PA, 2009

[51]Becke, A. D., Phys. Rev. A **38,** 3098 (1988)

[52]Lee, C.; Yang, W.; Parr, R. G., Phys. Rev. B **37,** 785 (1988)

[53]Armentrout, P. B.; Heaton, A. L.; Ye, S. J., J. Phys. Chem. A **115,** 11144 (2011)